University of Naples "Federico II"

Polytechnic and Basic Sciences School
PhD School in Chemical Sciences

Development and Applications of First Principles Approaches for Heterogeneous Functional Materials

Eduardo Schiavo

Advisor:
Prof. Michele Pavone

Examiner:
Prof. Antonio Carella

XXXII cycle
Coordinator: Prof. Angela Lombardi

Contents

Introduction

The last few decades of human history have been signed by an incredibly fast technological development. The advancement of the scientific knowledge that has allowed such progress revolves around the ever-growing field of materials science. Often, a big step ahead in the former stems from an important finding in the latter. As an important example, one may cite the work on cathode materials that allowed the development of efficient Li-ion batteries, for which the Nobel Prize in Chemistry was awarded last year [1, 2]. This was the turning point that opened the way to the world of portable electronic devices that have dramatically transformed our every-day life. In the same technological area, materials science has been the theoretical ground for the evolution of hi-tech electronic and opto-electronic devices (e.g. touch screens, OLEDs, transitors etc.) [3–5]. Applications extend all the way to the medical sphere, where the emerging of nanotechnology in biosensing and drug-delivery devices based on smart materials has led to huge advances both in therapy and diagnostics [6]. Heterogeneous functional materials have boosted the development of solar energy conversion devices, leading to the design of third generation solar cells such as dye-sensitized solar cells (DSSCs) and perovskite solar cells, and to the development of heterogeneous photo-catalysts that are able to reconvert solar energy in chemical energy [7, 8].

These materials have some peculiar properties that make them suitable for the aforementioned applications. In this thesis, we will mostly deal with two-dimensional (2D) materials, transition metal oxides and hybrid organic-inorganic materials. Unfortunately, the extraordinary properties of these classes of materials come with a price. For some of them, fabrication and characterization techniques are very complex; this certainly slows down the investigation of their properties

and the design of new systems and devices based on such materials. To unravel the complexity of the electronic structure properties that are involved in the operation of the devices for which they are employed, we really need to look at them at an atomistic scale. Experimental techniques often fail to reach this level of detail, due to the many complexities that are present in any real system (e.g. impurities, defects). To overcome these problems, experimental techniques may be assisted by theoretical investigation. By looking at the systems trough the magnifying glass of computational chemistry, we are able to have an insight on their microscopic properties and structure-function relations. This grants us a deeper level of understanding that is a key step for a future rational design of new, better performing, materials finely tuned for the target applications. The results of theoretical investigations can in fact be used to guide the experimental investigations in the right direction.

However, the computational study of such complex systems is far from trivial. When it comes to cutting-edge systems we are pushed towards the limits of the capabilities of the current theoretical methods and computing power. Of course different classes of materials present different challenges. To realistically represent a system to be used in an actual device, we usually need a model of a size that cannot be afforded by highly accurate computational methods. This is the reason why most computational material science studies use density functional theory (DFT).

This theory, altough very powerful for computing many interesting properties, suffers from some severe limitations. It is, in fact, a ground state theory that is not able to describe electronic transitions from this state to the excited ones, or perturbation of this state that generate interactions like van der Waals forces. The approximate nature of the functionals used is also a source of error; one may cite the very well-known self interaction error (SIE) due to the lack of exact exchange. A more detailed discussion on DFT and its typical flaws can be found in the next chapter. We will have to deal with some of the above mentioned problems to achieve our goals. In some cases, we will be able to rely on standard approaches to overcome some well-established DFT limitations, while in some other cases, we will need to develop new ones. In the next chapter, we go into more detail regarding the theoretical background of this thesis. We analyse the advantages

and flaws of the methods used throughout the text and give some technical details on how the computations were run. In Chapter 3 we discuss some methodological development carried out in our group in order to overcome the most limiting deficiencies of current state of the art theoretical methods.

One of the fields of materials science that has attracted a lot of attention in the last few years is that of solar energy conversion [9]. More in general, research endeavours towards obtaining efficient devices for clean energy conversion have been really increasing ever since the environmental concerns have become a pressing issue. Among the many renewable sources available on planet Earth, sunlight is by far the most abundant one, so it has been the main focus of research in this field. Standard photovoltaic (PV) devices based on crystal silicon are by now a well established technology with efficiencies reaching 25% [10,11]. However, classical PV is not completely free of environmental impacts [12] and suffers from severe limitations regarding the integrability of the conversion devices into other objects. Such integration can easily be achieved with technologies like Dye Sensitized Solar Cells (DSSCs) that can easily be integrated on flexible supports and have high efficiencies also in indoor light conditions. These devices, along with perovskite solar cells (based on similar principles) constitute the future generation of solar energy conversion devices.

Due to the intermittent nature of the source, research on solar has activated an intense research on energy storage. All kinds of batteries have been designed over these years (*e.g.* Li-ion, Li-air, Li-S, Na-ion) in order to store the excess energy and use it when the source is not available [13]. Another important way of storing this sunpower, is to convert it into a *chemical fuel* that can later be converted in energy. Photoelectrochemical cells (PECs) are based on this concept, *i.e.* sunlight is used to activate a catalytic process that converts an inert molecule into its reactive components so that the process can be reversed in a controlled way, producing electricity. One important example is the water splitting reaction, that can be easily reversed in a fuel cell (FC) configuration, obtaining clean energy production. Another important application of this PEC configurations is CO_2 recycling. By activating the reduction of carbon dioxide to small hydrocarbons, through sunlight and an adequate photocatalysit, it is possible to use the products

in a carbon-neutral way. In Chapter 2 we discuss some important results on materials for solar energy conversion concerning both electricity generation through DSSC devices and CO_2 photoreduction. For these applications, we mainly focus on transition metal oxides and their interfaces with molecules. The rich chemistry of the half filled d-orbitals makes them practical for a wide variety of uses. Different geometries for example influence the splitting of these orbitals, dramatically changing the electronic properties of these materials. The presence of vacancies or point defects is also important and very common. Morphology and line defects also play a role, given that in most cases interesting chemical events occur near the defects and rarely on perfect isotropic environments. In particular, we are interested in applications for energy conversion, for example in third generation solar cells and photocatalysis. Also in this case, doping can play an important role and the interfaces between such oxides with molecular systems can create new interesting hybrid organic-inorganic materials with amazing features.

In the last ten years, since the first scotch-tape synthesis of single layer graphene, the interest on 2D materials has grown incredibly fast. Unique structural and electronic properties were now available. Not only graphene, but several other materials of this family were put under the spotlight: hexagonal boron nitride (hBN), transition metal dichalcogenides (TMDs), phosphorene etc. What makes these systems even more interesting, is the fact that their properties can be tuned as desired in a number of ways. To name one, the doping of such materials has been extensively studied both theoretically and experimentally. Substituting an atomic site with an aliovalent atom or creating vacancies in certain atomic sites is a common way to include an excess or depletion of electrons to the system. Mechanical strain can also be used as a tool to influence the electronic properties by inducing geometrical deformations. But what really makes 2D materials so appealing is the fact that they can be interfaced between one another or adsorbed on surfaces of other materials (e.g. metals, metal oxides), resulting in new properties at the interfaces that are different from the sum of those of the starting separate materials. In chapter 4 we will extensively explore 2D materials and how their properties can be engineered at an atomistic level to optimize them for the desired application.

The work presented in this thesis is organized in four chapters covering three

major areas of the work done during my PhD. In Chapter 1, we intoroduce the general thoretical framework and report the computational methods used throughout this thesis. Chapter 2 describes the work on materials for solar energy conversion, this includes an extensive work on transition metal oxides surfaces and interfaces between these surfaces and molecular dyes adsorbed on them for DSSC applications and some work on CO_2 photoreduction on the surface of similar oxides. In Chapter 3 we discuss the development and applications of embedding techniques for the study of systems related to those investigated in the previous chapters, along with a DFT-D reparametrization for metal-molecule interfaces. Chapter 4 reports the work on 2D materials, describing both the investigation of graphene and metal-supported graphene, and transition metal dichalchogenides (TMDs) for catalytic applications.

Chapter 1

Methods

1.1 Theoretical Background

Computational methods have become by now a standard tool in materials science. Very often they accompany experiments in the characterization of the properties of materials, assisting them in the interpretation of results. As a matter of fact, they are very often the only way to acquire information at a scale that is beyond the grasp of the measurement. On the other hand, sometimes current computational tools are not powerful enough to catch the complexities of the real world systems that are investigated by the experimentalists. For these reason, a strong interplay between the two worlds is needed to tackle the intricacies of heterogeneous functional materials. Theoretical models at varying degrees of accuracy have been developed over the years, covering different size- and time-scales. Some of these are completely *ab initio*, others require some experimental input. A complete review is beyond our scope here and can be found elsewhere [14]. Density Functional Theory is certainly the most popular approach in the field of materials science. Its linear scaling in the orbital free formulation, that comes from the direct application of the Hohenberg and Khon theorems [15], makes it an incredibly cost-effective and powerful tool, though only applicable to a few main group metals. By reintroducing the orbital formalism for the kinetic energy evaluation, Kohn and Sham gave birth to the DFT approach in the widespread form that we know today [16]. In spite of the increased computational cost (in the

best case it scales as N^3 [17]), KS-DFT is considered the best affordable way to get reliable and accurate results at a QM level. Most commonly, a density functional of the generalized gradient approximation (GGA) family is used within this scheme. Especially when treating extended, solid state systems, DFT is very often the only possible choice, since the cost of more accurate correlated wavefunction methods is simply too high for the typical high performance computing (HPC) set up. Obviously, the low-cost of DFT comes at the expense of its applicability: the approximations that make it inherently cost-effective lead to some severe limitations. First of all, DFT is by construction a single-reference, ground state theory. Every time we are interested in excited states we are forced to abandon it for a more expensive method (*e.g* coupled cluster (CC), GW, configuration interaction (CI), complete active space self-consistent field (CASSCF)). One possible way to obtain information on the excited states without switching to the wave-function formalism, is time-dependent DFT. This method relies on the Runge-Gross theorem [18] which is a time-dependent extension of those of Hohenberg and Kohn for a time dependent potential mapped to a time dependent density. As an example, one may calculate excitation energies as the poles of the linear response function. Once again a detailed description of the theory behind this is beyond the purpose of this thesis and the interested reader can find more information in reference [19]. In Section 2.1.1 we report some TDDFT calculations to determine excited state properties of some dyes.

Another important consequence of using a ground state theory is missing the information about transient perturbation of the ground state that give rise to noncovalent interactions (*i.e.* dipersive forces). When studying interfaces between organic and inorganic systems, for example, we encounter the problem of correctly describing the van der Waals forces. These forces are in fact very important in glueing the system together. There is an extensive research on how to amend to this lack of dispersive forces in DFT. Many different approaches have been proposed and used over the years, some being very accurate but expensive. The main workhorse for dispersion correction in DFT is the family of semiempirical methods developed by Grimme [20, 21]. These in fact work incredibly well for molecular systems but are still inadequate for the description of molecules adsorbed on transition metals. The basic idea behind these methods is to compute the

dispersion contribution with a pairwise potential that is completely parametrized with respect to the atoms. As an example, in the simplest DFT-D2 approach, dispersion is computed via the London-like formula:

$$E_{disp} = -s_6 \sum_{i=1}^{N_{at}} \sum_{j=i+1}^{N_{at}} \frac{C_6^{ij}}{R_{ij}^6} f_{dmp}(R_{ij}) \tag{1.1}$$

where s_6 is a scaling factor depending on the DFT functional used, R_{ij} are the atomic distances, C_6^{ij} are the pairwise coefficients that are obtained from the atomic ones and f_{dmp} is a damping function that shuts down the dispersion contribution at short range. The so-computed E_{disp} is simply added to the DFT energy, without adding any computational cost to the calculation. In the more refined DFT-D3 method, the atomic coefficients are obtained from TDDFT calculations and the atomic connectivity is taken into account in calculating the C_6^{ij}.

A different scheme, developed by Dion et al. [22, 23] is based on a non-local correlation functional (vdw-DF) that models the long-range correlation that generates the dispersion forces. While DFT-D2 and D3 are known to ovestimate the dispersion interaction at the metal-molecule interface [21], vdw-DF improves the description of the adsorption energies but overestimates the metal-molecule distance [24]. After that, several other refinements of this functional have been developed over the years [25–28]. Another method worth mentioning is that by Tkatchenko and Scheffler, based on the summation of interatomic coefficients, obtained from the electron density of the molecule and accurate reference data for the free atoms [29]. In a very recent work, Tao *et al.* developed an interesting method, based on Lifshitz-Zaremba-Kohn second order perturbation theory for including dispersive forces in DFT [30]. This method (named PBE + vdW) gives results that are close to RPA benchmarks. The downside of this method is the restriction that the metal surface must be clean and the fact that its computational cost is still far greater than DFT-D. This is not a complete list of the approaches proposed to amend for the lack of dispersion in DFT, the interested reader may find more informations on some reviews on the topic [31, 32]. A general trend is that the more accurate the models, the higher their computational cost. As an example, a very efficient implementation of the non-local vdw-DF proposed by

Román-Peréz et al. has twice the computational cost of a standard semilocal DFT calculation [33].

Thanks to its simple functional form, the DFT-D2 scheme can be tuned to fit experimental data (or more accurate computational results). Robledo *et al.* proposed to apply the correction only on the metal atoms at the topmost layer of the surface. This way they try to account for the screening effect of metals. Unfortunately, this approach lacks transferability to different systems or reconstructed surfaces. One of the reasons for the inability of the DFT-D approaches to accurately model hybrid systems involving transition metals can be found in the definition of the atomic coefficients. The scheme by which they are obtained is not exactly the same in D2 and D3, but they both rely on the atomic polarizabilities and ionic potentials of the isolated atoms and of the atoms in typical bonding situations. Since this is not really applicable to TMs, an average parameter is used for a whole transition series; taken as the mean value between that of the preceding noble gas and that of the following group III element. Another important factor that can affect the DFT-D corrections is the damping function. Different damping schemes (*e.g.* zero, Becke-Johnson) give very different results, since it is of critical importance to turn off the dispersion at the right distance.

In Chapter 3 we propose a reparametrization of DFT-D2, with the aim of making it suitable for large scale calculations on hybrid systems (like metal-molecule interfaces). The reparametrization is carried out on the case study of adsorption of small organic molecules on Ag(111). In Section 4.1 of Chapter 4 we use our reparametrized method (DFT-Ds) to study the interaction between a (doped)graphene system and Ag(111).

A third problem we encounter very often in DFT applications, is the accurate treatment of localized open shell electrons that are very common, for example, in the d orbitals of transition metals. This problem arises due to the presence of the so called self interaction error (SIE). In the Coulomb part of the potential, the interaction of an electron with itself is allowed (*i.e.* the term i=j). In a wavefunction-based method (as Hartree Fock) this term would be entirely cancelled out by its exchange counterpart. Unfortunately, this part is only approximate in DFT and fails to remove all the self interaction. This causes the electrons to repel themselves and give unphysically delocalized solutions. There are two main

strategies to overcome this problem. One is going one step up on the Jacob's ladder of density functionals [34] and use a hybrid functional, that contains a percentage of exact exchange. The quantity of HF is somewhat arbitrary and depends on the functional used, some more refined functional scales this quantity with respect to the electron distance (range separated hybrids). Hybrid functionals give good results on the electronic properties (*e.g.* band gaps) of transition metal oxides but the added computational cost is far from negligible. A less pricey approach is DFT+U, where the difference between the intra-atomic Coulomb energy and exchange (U-J) is added as a parameter, enforcing electron localization [35]. The U and J parameters can either be extracted from *ab initio* calculations [36] or fitted against experimental data. Throughout this thesis we will make use of both methods in different situations. A common approach we used is that of running geometry optimizations with a GGA (or GGA+U) functional and then run single point calculations for the determination of the electronic structure with a hybrid functional. In Section 4.2 of Chapter 4, we also report a benchmark of a few density functionals (a GGA and two hybrids) for the determination of the structural and electronic properties of transition metal dichalcogenides.

A major issue we encounter in the description of heterogeneous functional materials arises from having different target properties on the different parts of the system. A good example of this are the hybrid electrodes for DSSCs described in Chapter 2. To correctly represent the physical phenomena occurring in such an electrode, one would need to model the photochemical process of excitation of the dye and electron or hole transfer from the dye to the semiconductor surface. We have already pointed out that DFT is a ground state theory. Hence, it is not capable to properly describe the LUMO of the molecule that is involved in the excitation process. A higher level of theory is needed to correctly model this phenomenon. On the other hand, to reproduce the solid substrate in the right way we need a size of the model system that is too big to be able to afford anything more expensive than DFT. One possible solution could be to partition the system and use two different levels of theory for two different parts, using one of the so-called "embedding methods". In such methods, a *cluster* is carved out of the system containing the region on which a higher detail/accuracy is needed. This cluster is treated with a correlated wavefunction (CW) method, while its interac-

tion with the environment (*i.e.* the remaining part of the system) can be treated in a number of ways, depending on the methods used. In an ionic solid, for example, the simplest approach would be to replace the atoms in the environment with point charges. A shell model can be used if the polarization of the environment needs to be accounted for [37]. Another common approach is quantum mechanics/molecular mechanics (QM/MM) that is widely applied to molecular systems and semiconductor surfaces [38]. In this method, the cluster is treated with a quantum mechanical method, while a classical force field is used to describe the environment [39]. A QM/MM approach that is worth mentioning is the ONIOM embedding, that allows for several layers that can be treated with different levels of theory [40]. Embedding methods that employ an interaction potential between the cluster and the environment may be collected into two categories: orbital-based and density-based. The first often employ the Green's function of the system or an explicit contribution from the molecular orbitals of the system [41–43], while the latter are based on approximate kinetic energy densisty functionals (KEDFs) in an OFDFT embedding potential [44]. One interesting density-based approach that goes beyond the use of KEDFs is density functional embedding theory (DFET) that was first proposed by Cortona [45] and then further developed by Carter and co-workers [46–48]. In this method, the electron density is partitioned into that of the cluster and that of the environment, that are both treated at a QM level (DFT). The interaction between the cluster and the environment is treated via a unique embedding (interaction) potential that is obtained through an optimized effective potential (OEP) procedure. Once the potential has been obtained, it can be used to run a calculation on the cluster with a CW method, combining the periodic DFT description of the environment, with an accurate treatment of the cluster [49]. In Chapter 3 we discuss the theory and implementation in a plane waves code (VASP) of DFET that can be able to enhance our capability to treat such complex structures.

1.2 Computational Details

Most of the results reported in this thesis were obtained by DFT calculations run with the Vienna ab initio simulation package (VASP) [50–53], using plane waves basis sets. To correct for the self interaction error we used the DFT+U scheme in the rotationally invariant approach by Dudarev et al. [54] as implemented in VASP [55] and in some cases the hybrid functionals by Heyd, Scuseria and Ernzerhof (HSE) [56, 57] and by Adamo and Barone (PBE0) [58]. The GGA part in the DFT+U and standard DFT calculations were run with the Perdew, Burke and Ernzerhof (PBE) functional [59, 60]. Projector augmented wave (PAW) potentials were used to treat the core region of the atoms [61]. We used the correction developed by Grimme to account for the dispersive interactions (DFT-D2 [20] and DFTD3 [21]) and in some cases our reparametrization (DFT-D2s [62]). We used the Gaussian09 Program [63] for the theoretical characterization of the isolated carbazole dyes (Section 2.1.1) and for the cluster calculations for the reparametrization of DFT-D2s When computing adsorption energies with this program and gaussian basis sets, the counterpoise correction (CP) was applied to remove the basis set superposition error (BSSE).

The computational details regarding the different calculations are reported at the end of each section of the following chapters.

Chapter 2

Materials for Solar Energy Conversion

For the past twenty or thirty years, environmental issues have been a hot topic. In their various declinations, they have very much affected not only the scientific discussion, but also politics and our everyday life over these years. It is in fact out of doubt that as our world experiences a boom in demographic growth, the exploitation of polluting sources to provide energy to the increasing population becomes a critical issue. Figure 2.1 shows very clearly how the annual growth rate of world population has experienced a spike in the late seventies and how the total population has been steeply increasing ever since. Projections are even more alarming, by 2050 we will have almost doubled the number of people we had in the late eighties. It is very clear that it is vital to switch to a sustainable way of producing and supplying energy to the populations, as the greenhouse gases emissions are also increasing at an alarming rate. As stated above, these concerns are nothing new. The first major political step towards a reduction of polluting emissions was made in 1992 with the *United Nations Framework Convention on Climate Change*, that will be the basis for the *Kyoto Protocol* five years later [64]. The objectives of these treaties were the "[...] stabilization of greenhouse gas concentrations in the atmosphere at a level that would prevent dangerous anthropogenic interference with the climate system". As January of this year, 136 countries of the 144 needed for it to enter into force have ratified the second

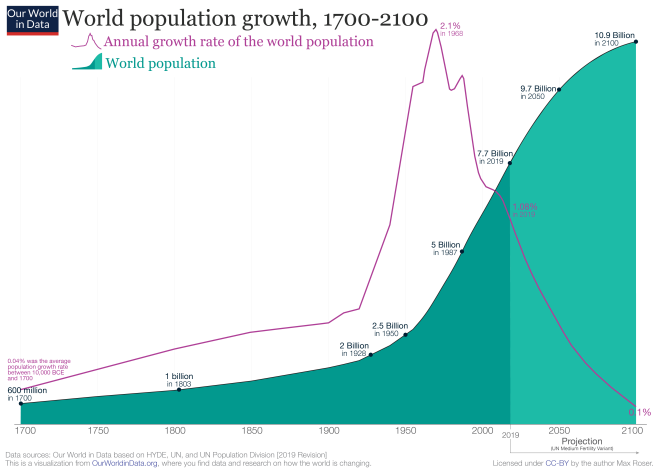

Figure 2.1: World population growth and population over the last 300 years according to Our World in Data

commitment period of the Kyoto Protocol (Doha Amendment) [65]. A greater international consensus on taking action against global warming was reached in December 2015, with the representative of 196 states signing the Paris Agreement [66]. The efforts of the parties, with varying targets on the emissions set by each country, will be devoted to reduce the emissions of greenhouse gases in order to keep the increase in global average temperature below 1.5 °C above pre-industrial levels. At the very core of a change towards a less polluting growth model lies the technological advancement.

Even in this field, the role of research on materials is crucial for the development of new, efficient energy conversion devices. Switching from fossils to renewable sources is in fact the only way to achieve the goal of reducing the anthropogenic impact on global warming. There are many renewable sources available on the planet, and probably we will need to exploit all of them to extract enough energy for the constantly growing population. Among these sources, sunlight is by far the most abundant one. An efficient use of the sunpower that strikes the surface of the earth every day would satisfy the need of the global population [67]. Solar energy can be either directly converted to electricity via solar cells, or converted in "chemical energy" by using it to photocatalize slow reactions. As an example of the latter, the trapping and recycling of polluting greenhouse gases (CO_2 above them

all) can be done exploiting this energy. The aim is to convert CO_2 to chemicals that can be used for other purposes in a CO_2-neutral way.

In this chapter, we will present our results on materials for two major target applications: i) electrodes for DSSCs, ii) photocatalysts for CO_2 reduction

Dye Sensitized Solar Cells In the field of solar energy conversion, most mass-produced and widespread devices still rely on the old Silicon-based photovoltaic panels. These solar cells have decent efficiencies, but suffer from some limitations. Their efficiency becomes in fact limited in diffuse light conditions and they rely on highly pure crystalline Si to work. This means that it is not possible to design the device in a different way with respect to the large black solid panels that are not free of environmental impacts [68]. DSSCs on the other hand, are very flexible devices that also work in indoor light conditions [69] and can be easily integrated in other objects, architectural elements [70], accessories and so on... [71] Moreover, even though the cost of Si-based devices has gone down in recent years thanks to the scaling of mass production techniques, the developement of devices based on cheaper materials may lower further the cost of production of solar panels [72, 73].

DSSCs were first proposed by Grätzel and O'Regan in 1991 [74]. Their paper marked a paradigm shift in the world of solar cells. For many years, in fact the efficiency of solar cells was connected to the degree of purity and crystallinity of the solid electrode. In DSSCs, the electrodes are instead made of semiconductors nanoparticles with organic dyes adsorbed on them. In these devices the conductivity of the mesoporous semiconductor is increased for smaller nanoparticle sizes [67] Figure 2.2 gives a pictorial representation of how a DSSC works.

The diagram depicted in Figure 2.2 is relative to an n-type DSSC. There are in fact two kinds of DSSCs, n- and p- type, depending on the semiconducting character of the semiconductor. In both of them, the process starts from the photoexcitation of the dye. In an n-type system, the event that follows is an electron transfer from the LUMO of the photoexcited dye to the conduction band of the semiconductor. The oxidized dye is regenerated by a redox couple present in the electrolyte solution, which in turn re-accepts an electron from the counter electrode. In a p-type device, on the other hand, the photo excitation is followed

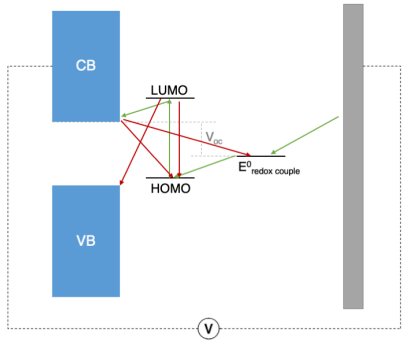

Figure 2.2: Scheme of a n-type dye sensitized solar cell. The Blue boxes represent the energies of the valence band (VB) and conduction band(CB) of the semiconductors. The HOMO and LUMO level refer to the dye adsorbed on it and the redox potential to the redox couple present in the electrolyte. The tall grey box on the right represents the counter-electrode. Green arrows depicts the (desired) electron transfers

by an electron transfer from the valence band of the semiconductor to the HOMO of the dye, the current flows the other way round (this process is usually described as an *hole injection* from the dye to the semiconductor). Each of these processes competes with an undesired recombination process (red arrows in figure) that can reduce the cell efficiency and must be hindered (or, when possible, completely suppressed). In these devices the efficiency is defined as:

$$\eta = \frac{V_{OC} J_{SC} FF}{P_{in}} \tag{2.1}$$

where V_{OC} is the open circuit voltage of the cell, J_{SC} the short circuit current of the cell, FF the fill factor and P_{in} the intensity of the incident light. The latter can vary between 0 and 1 and is defined as the maximum power of the cell divided by the product of V_{OC} and J_{SC}. We will go through some detail of how the properties of the materials affect these values (and consequently the efficiency) as we discuss the results in the following sections. For a more detailed review of the operational principles of a DSSC the reader is referred to reference [67]. At

this point, it is worth noticing only that the V_{OC} (in an n-type device) depends on the difference between the edge of the conduction band of the semiconductor and the redox potential of the redox couple, see Figure 2.2. Further developments of DSSCs involve the possible constuction of so called *tandem cells*, where both electrodes are photoactive: one being a n-type electrode and the other a p-type one [75, 76]. In such devices the V_{OC} is equal to the sum of those of the two separate devices, and the efficiency is much increased. Usually dyes with shifted absorption maxima are used on the two electrodes in order to cover a larger range of the solar spectrum and improve light harvesting. Another important thing to mention is that tandem cells can also be used as photoelectrochemical devices to perform the photocatalysis of reactions of interest in the field of clean energy conversion (*e.g.* water splitting) [77]. Current record efficiencies are around 14% [78] for n-DSSCs, while p-DSSCs are stuck below 2% [78, 79]. In order to achieve greater efficiency with tandem cells, the p-type part must be improved. One of the main reasons for such poor performances can be ascribed to NiO, which is the current standard semiconductor employed in these devices due to its low cost and easy manipulation [80–82]. NiO presents in fact several drawbacks: low electrical conductivity, low hole mobility and high valence band edge potential with respect to the most common I^-/I^{3-} redox couple, which yields a low open circuit voltage of the cell [83]. An alternative to NiO could really boost the efficiencies of p-DSSCs. A class of materials that has emerged as a possible alternative to NiO is the Cu-delafossites family. These oxides, of $CuMO_2$ formula, are wide band gap semiconductors with a p-type conductivity [84]. This makes them almost unique, since most of the transparent conducting oxides (TCOs) exhibit a n-type conductivity. These materials could in principle have all that it takes to outperform NiO in p-DSSC applications: they have a wide optical gap that can reduce undesired absorption phenomena and their low lying valence band edge could grant the cell a higher V_{OC} with respect to NiO [85, 86]. For this reason, it is important to understand in detail the electronic and structural properties of these copper oxides and how it is possible to tune them to design new efficient devices. In the first paragraph of Section 2.1 we investigate the properties of three members of this family: $CuAlO_2$, $CuGaO_2$ and $CuCrO_2$. We analyze their electronic structure and the effect of a p-type (Mg) doping on them, and compare the calculated

parameters relevant for p-DSSC operations with those of NiO.

Despite all the positive effects of $CuMO_2$/NiO substitution on efficiency-related parameters, this does not always result in an overall increase of the PCE. This is due to the fact that the overall cell efficiency is also strongly dependent on the properties at the semiconductor/sensitizer interface. As an example: the lower the position of the valence band, the smaller the driving force for hole injection. For this reason, sometimes typical dyes used for NiO (*e.g.* C343, P1 etc) do not work (or work with lower efficiencies) with delafossites [83,86,87]. Hence, in order to make the best of the electronic properties of $CuMO_2$ oxides we might need to select new dyes with a suitable alignment of the frontier orbitals with respect to the band edges of the SC. Another important issue realted to the dye-SC interface is the coverage of the dye, which is strongly dependent on the shape and size of the nanoparticles and to the binding strength of the dye to the surface. One of the open questions is weather the anchoring groups used to attach the molecules on NiO are suitable to the surface of the delafossites. In the second paragraph of Section 2.1, after having addressed the properties of different oxides and selected the one that seems the best choice, we analyse the interaction between two anchoring groups on it. We chose carboxylic acid (-COOH), which is the most common group for these applications, and phosphonic acid (-PO_3H_2) that has been used on NiO giving higher efficiencies and stability in aqueous systems [88–91].

Even though NiO is the main limiting factor, some improvement can be achieved also on the dye side. A good absorption of sunlight and an intra molecular charge transfer are important properties for an efficient electrode. Most importantly, we will see how it is really the interface between the two materials which grants the cell the properties needed. Hence, a theoretical investigation that takes into account the properties of such interface is needed to explain the experimental data. In the first paragraph of Section 2.1, we present a combined experimental and theoretical study on three newly synthesized push-pull dyes. We discuss their structure and the effect of different modifications on the light harvesting and charge transfer properties of the isolated dyes and on the interfaces between the dyes and NiO. From the latter we are able to extract some parameters directly related to the hole injection driving force and a qualitative picture of the likelihood of the recombination process that allow us to explain the relative efficiency of the dyes in operating

conditions.

Recycling Carbon Dioxide Another possible way to stop the increase of CO_2 concentration in the atmosphere is reconverting it into value-added chemicals through photo-electrochemical cells (PECs). The chemicals produced in this way can after be used for various applications, in a CO_2 neutral way. Many researchers have focused on optimizing homogeneous [92] and heterogeneous [93–97] photocatalysts for the CO_2 reduction reaction (CO2RR). These technologies are still quite far from real world applications because of their low CO_2 conversion efficiencies, high overpotential and low selectivity towards specific hydrocarbons. CO2RR is usually performed in acidic aqueous solutions because proton-coupled electron transfer (PCET) steps are less endoergic than forming the $CO_2^{\cdot-}$ by electron transfer [92]. The competing hydrogen evolution reaction (HER) in aqueous media, that can occur through proton or water reduction, may cause a decrease in Faradaic efficiency [98]. Copper is the only metal that is able to catalyse the production of hydrocarbons beyond formic acid and carbon monoxide [99]. For this reason, it has been widely used to study the mechanism of the reaction and to try to design new catalysts. Both measurements and calculations have demonstrated the activity of Cu supported on transition metal carbides [100, 101] and oxides [102, 103], and that of copper oxides [104–107] for CO_2 photo-activation. Unfortunately, for the latter the high overpotentials promote their partial reduction to metallic Cu, making the electrode unstable. CuO/Cu_2O nanorods arrays with decent stabilities have been designed by Gahdikhani *et al.* and Rajeshwar *et al.*, calling attention to the importance of morphology in tuning the features of the catalysts [108, 109]. As mentioned before about solar energy conversion in solar cells, Copper-based delafossites have attracted interest in the last few years. Their singular thermoelectric, magnetic and optical properties make them suitable for a number of applications in optoelectronics, electron emitters, LEDs, laser diodes and solar cells [110–112]. One interesting feature of these materials is their mixed Cu(I)/Cu(II) valence, that gives them a p-type character. Among the big family of this oxides, $CuFeO_2$, even though is not suitable for DSSC applications, is particularly interesting for the catalysis of CO2R. It is a semiconductor with an optical gap that falls in the visible region (1.52 eV) [113] and with the bottom of

the conduction band at an energy that makes the redox potentials of CO_2 to desirable hydrocarbon accessible [114, 115]. All the properties described above, plus its low efficiency towards the HER, make $CuFeO_2$ a good electrode material in PECs for CO2R. As pointed out for copper oxides, even in this case the efficiency of these electrodes has been found to be strongly dependent on the morphology and on the synthetic methods [115, 116].

As discussed for other members of the delafossites family for applications in solar cells, a doping of such materials with Mg in the site of the trivalent cation can have important effects. Bocarsly and co-workers have shown that doping $CuFeO_2$ with 0.05% Mg^{2+} results in a better stability, with no metallic copper found after 8 h electrolysis), and an improved efficiency (*i.e.* 14%) with a selectivity towards formate [117]. HER activity is lowered, but not completely suppressed. A recent work by the same group has investigated the effect on carrier concentration and mobility of varying concentrations of Mg doping and Cu vacancies [118]. They measured the best photo-responses with the lower p-type carrier concentrations and higher carrier mobility: increasing too much the Mg doping can yield the formation of n-type defects, likely oxygen vacancies. Also mixed phase materials ($CuFeO_2$/CuO) have been investigated, they have been found to produce formate with high selectivity and to catalyse the oxygen reduction reaction [119,120]. They also found that by tuning the Fe:Cu ratio in such mixed electrodes it is possible to tune the selectivity towards the formation of acetate [120]. This emphasizes the different role of the different metals. Once again morphology plays a key role: Yoon *et al.* have found that structures composed by layers of CuO and $CuFeO_2$ show a high selectivity towards the production of formate [121]. In the aforementioned works, the role that $CuFeO_2$ plays on catalysis is not properly addressed, the main focus is in fact on its photoelectrochemical properties and the active role in catalysis is left to CuO and Cu in particular.

In a fourth part of Section 2.1 we investigate the catalytic role of $CuFeO_2$ on CO2RR and demonstrate the active role of the Fe sites. The microscopic processes of the adsorption and activation of carbon dioxide on this material have been so far unexplored. We investigate the specific role of surface atoms and defects and comment their effect on the morphology of the system in comparison with literature. As an example, it has been recently proven that oxygen vacancies have

an important role in activating CO_2 adsorption of the surface of copper (I) oxide thanks to the electronic rearrangement [122]. In this chapter, we provide an in-depth analysis of the adsorption and activation of CO_2 on $CuFeO_2$ addressing the specific roles of the different metallic sites on the process, as well as that of vacancies in surface. In this way we advance the understanding of the specific role in catalysis of different modifications that can help us design new and better performing electrode materials.

The next sections are organized in four areas regarding: i)the properties of the family of copper delafossites as an alternative to NiO, ii) the possible binding modes of two commonly used anchoring groups for dyes (carboxylic and phosphonic acid) on a delafossite, iii) the interface between three newly synthesized carbazole-based dyes and the current standard NiO iv) CO_2 adsorption and activation on $CuFeO_2$ for CO2RR catalysis.

In section 1.2 we have collected the general computational approach, while section 2.1 contains the core results of these works. The relative conclusions and future perspectives are reported in Section 2.2. The last paragraph of each subsection of Section 2.1 contains the computational details for that specific subsection.

2.1 Results and Discussion

2.1.1 Dye-NiO interfaces

Before exploring the possible alternatives to NiO for p-DSSC applications, in this section we provide an analysis of the interface between newly synthesized dyes and NiO. Even though we have repeatedly pointed out that most of the issues related to the underdevelopment of p-DSSCs are solvable replacing NiO, we believe that there is room for improvement also on the design of the dyes. Key parameters for efficient dyes are a good sunlight absorption and an intramolecular charge transfer upon excitation; in this way, the electron is localized far from the surface of the semiconductor, preventing undesired recombination processes and the hole is localized close to the anchoring group, favouring the hole injection process. A dye with such features can really boost the performance of the cell. However, it

might not be enough; since the electronic features at the interface can still hinder the crucial charge transfer processes needed for the cell to work.

Synthesis and electrochemical characterization The new dyes have a common carbazole electron-donating unit, functionalized with an acrylic acid anchoring group and a different electron withdrawing group. The group of Prof. Carella at the University of Naples "Federico II" performed the synthesis and characterization of the dyes. Here we omit the details about the synthesis, thermal and thermogravimetric characterization of the dyes, the interested reader is referred to the work published on the subject for further details [123]. We only mention that the dyes have shown a good thermal stability and decomposition temperatures much higher than operating DSSC temperatures. The UV-vis spectra of the dyes have been measured in tetrahydrofuran (THF) solution and are depicted in Figure 2.3

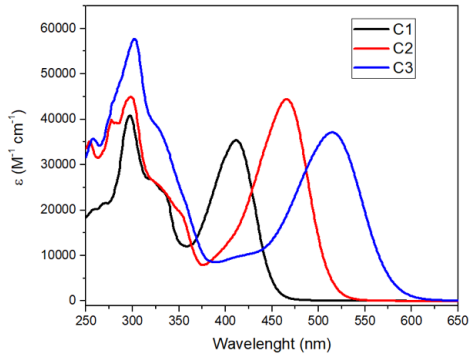

Figure 2.3: UV - vis spectra of the dyes in THF solution

The absorption properties are influenced by the different electron withdrawing group, that shifts the absorption maxima. **C1**, **C2** and **C3** have maxima at 411, 464 and 514 nm, respectively. Also the molar extinction coefficients are fairly high, in a range from 35000 cm^{-1} M^{-1} to 44000 cm^{-1} M^{-1}. The optical properties are listed in Table 2.1

The redox potentials of the dyes have been obtained by means of cyclic voltammetry versus the (Fc/Fc^{+}) couple. The CV plots are reported in Figure 2.4

Table 2.1: Optical properties of the synthesized dyes.

	$\lambda_{max}(nm)$	$\epsilon(cm^{-1}M^{-1})$	$\lambda_{max}(nm)$	$\epsilon(cm^{-1}M^{-1})$
C1	297	4.04×10^4	411	3.54×10^4
C2	300	4.44×10^4	465	4.44×10^4
C3	302	5.03×10^4	515	3.71×10^4

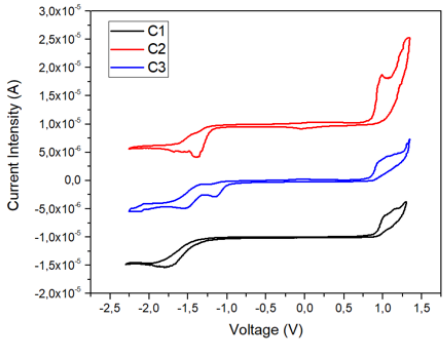

Figure 2.4: CV plot of the three dyes under study; the experiment was performed at a scan rate of 100 mV s^{-1} in dichloromethane solution (∼0.3 mM), and using tetrabutylammonium hexafluorophosphate (100 mM) as non-redox electrolyte. The CV scan explores first positive applied voltages and then move towards negative values.

The redox potential can be correlated to the energies of the frontier orbitals, according to:

$$E_{HOMO} = -(E_{onset,ox} - E_{Fc/Fc^+} + 5.1)$$

$$E_{LUMO} = -(E_{onset,red} - E_{Fc/Fc^+} + 5.1)$$

We can use these values to compare the effect of the different acceptor groups, but not to relate them directly to the position of the dyes in operating conditions, since the interface with NiO is missing. We found that the strength of the acceptor group has a major effect on the LUMO position. The HOMO is not much effected, only slightly destabilized. Further details on the nature of frontier orbitals are reported in the next section. Table 2.2 lists the electrochemical properties of the dyes

Table 2.2: Electrochemical properties of the synthesized dyes.

	$E_{ox}(V)$	$E_{red}(V)$	$E_{ec}(V)$	$E_{opt}(eV)$	$E_{HOMO}(eV)$	$E_{LUMO}(eV)$
C1	0.92	-1.37	2.29	2.69	-6.02	-3.73
C2	0.89	-1.22	2.11	2.35	-5.99	-3.88
C3	0.84	-0.99	1.83	2.07	-5.94	-4.11

Computational analysis In this section, we report a theoretical characterization that we performed on the three dyes, that were later tested in operating conditions in the group of Prof. Gerbaldi at the Polytechnic of Turin. As discussed above, the three dyes are push-pull dyes, with a carbazole unit as a donor, a carboxylate group as anchoring and differ only in the acceptor group. Figure 2.5 depicts the chemical structure of the three dyes under study.

The optical and electrochemical properties of each of these dyes in solution have been characterized. We rationalized these results by means of state-of-the-art first principles calculations based on DFT and TD-DFT. The effect of the solvent are included by means of the polarizable continuum model (PCM) of implicit solvation. The dye-electrode interfacial properties are studied in a periodic slab

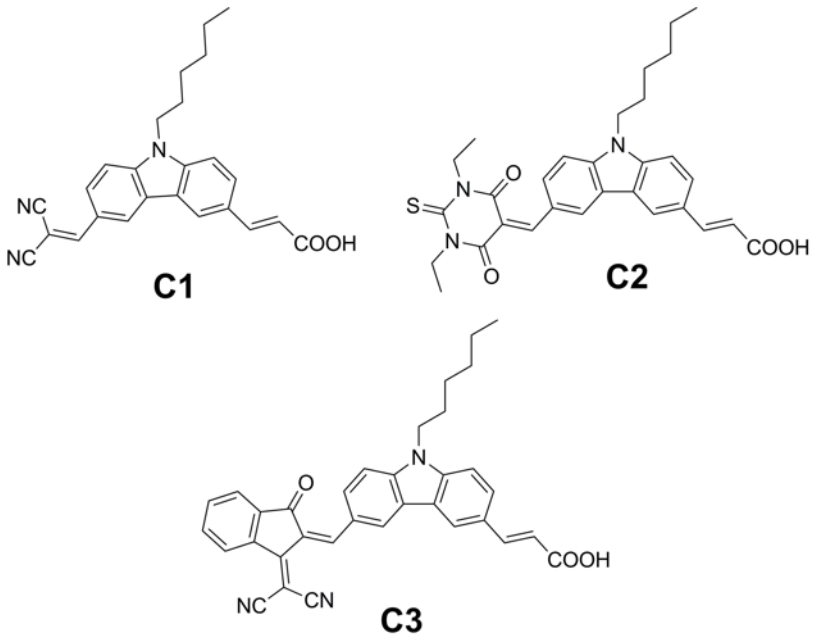

Figure 2.5: Chemical structures of the C1, C2 and C3 dyes

approach. In carrying out this characterization, we highlight the need to correctly account for the interface between the systems to catch the relevant features for DSSC operation.

The first step of this study has been the synthesis of these dyes and their electrochemical characterization. The data relative to such synthesis and characterizations can be found in reference [123]. As a second step, we performed a theoretical analysis of the dyes in an attempt to rationalise their optical and electronic properties. We investigate the structural and electronic features at a DFT/TD-DFT level. To simplify the model systems, we remove the long alkyl chain on the N of the carbazole moiety and replace it with a methyl group. We assume this is a safe choice, since the alkyl chain does not affect the electronic structure, which is governed by the acceptor and donor groups on the push-pull dye. We considered different conformations around the bond between the carbazole unit and the acceptor group, but found no significant energy difference. The DFT minima of the three dyes are shown in Figure 2.6 along with the isodensity surface

plots of the computed HOMO and LUMO.

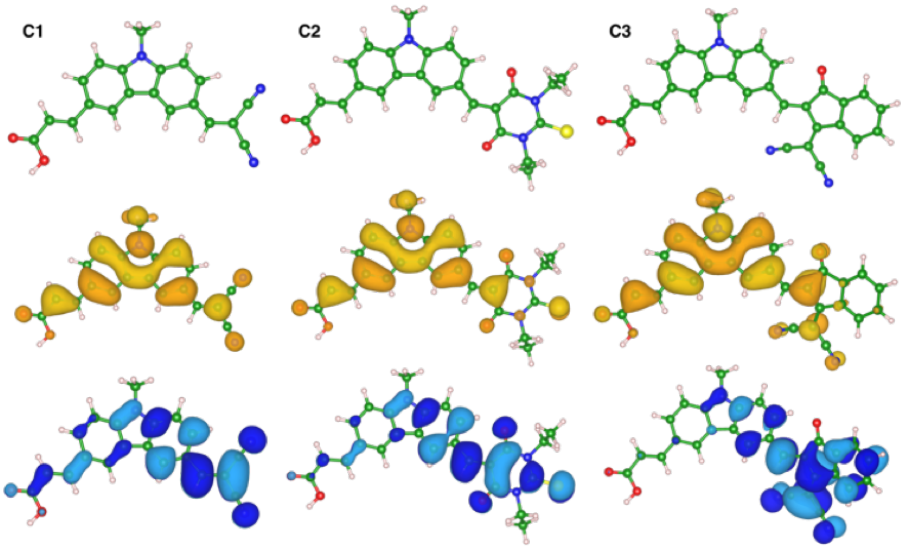

Figure 2.6: Minimum-energy structures of C1, C2 and C3 model dyes in ACN (top panel), HOMO (middle) and LUMO (bottom) (isodensity surface level: 0.02 a.u.; positive/negative surfaces are in yellow/orange and blue/cyan for HOMO and LUMO, respectively). Color legend: C green, O red, Ni blue, S yellow, and H white

From a qualitative perspective, we can see that in the three systems the HOMO is localized on the carbazole, while the LUMO is mostly located on the acceptor group. The degree of localization of the LUMO increases from C1 to C3, as the electron-withdrawing strength of these groups. In order to evaluate the optical properties of these molecules, we performed TD-DFT calculations. Table 2.3 lists the results of such computations.

A good vertical excitation is permitted by the overall good overlap between the HOMO and LUMO of the dyes, which is reflected on the high oscillator strengths value, listed in the third column of the table. The computational results in ACN qualitatively agree with the measurements in THF, with some minor discrepancy in the LUMO energies due to the different solvents employed. The electrochemically derived LUMO also includes the reorganization energies for the reduction of the dyes that are neglected by the calculation. Also the trend in visible band maxima

Table 2.3: Computed electronic properties of the **C1**, **C2** and **C3** dyes. Vertical absorption wavelengths (λ_{max}) and oscillator strengths (f), E_{0-0} transition energy (see text), and absolute energy position of the HOMO and LUMO. All data have been computed in ACN solvent.

	$\lambda_{max}(nm)$	f	$E_{0-0}(eV)$	$E_{HOMO}(eV)$	$E_{LUMO}(eV)$
C1	361	1.347	3.10	-6.06	-2.96
C2	389	1.626	2.75	-6.00	-3.25
C3	425	1.165	2.57	-5.85	-3.28

(411, 465, 514 nm from **C1** to **C3**) is reproduced by the theoretical values, catching the red shift from **C1** to **C3** and the higher value of f for **C2** in agreement with the measured maximum value of the molar extinction coefficient among the three dyes. By analyzing the TD-DFT transitions, we can assign this first bright band to the HOMO - LUMO transition. Table 2.3 lists also the E_{0-0} transitions, that are the energy differences between the S^1 excited state minimum and the S^0 optimized ground state. Thanks to this transition energy we are able to extrapolate the position of the LUMO that can be compared with electrochemical data reported in the previous section. Again, the measured and calculated trends are the same. A crucial properties of push-pull dyes as the ones we are studying here, is the internal charge transfer (ICT) that occurs upon excitation. As we mentioned before, an efficient ICT can enhance hole injection and suppress recombination. Here we have quantified the extent of this ICT with the approach proposed by Ciofini *et al.* [124] . We also compute the charge transfer excitation length (D_{CT}) in the same model, defined as the distance between the centroids of the charge densities before and after the transfer. Table 2.4 lists these data.

Table 2.4: intramolecular charge-transfer parameters upon photoexcitations: charge transfer length (D_{CT}) and amount of electronic density that is transferred (q_{CT}).

	D_{CT} (Å)	$q_{CT}(e^-)$
C1	2.65	0.601
C2	2.83	0.642
C3	3.45	0.694

These data follow the recurring, and by now expected, trend from **C1** to **C3**. We have seen how the computational analysis agrees with the properties of the dyes measured in solution. By looking at the ICT and optical properties one would now expect the trend in relative charge injection efficiency to be **C3>C2>C1**. However, DSSC are complex multicomponent devices where the interfaces between different materials play a fundamental role. We have stated time and again throughout this thesis that very often at the interfaces new features emerge that are different from the sum of those of the separate materials. To explore this possibility, we have carried out an analysis of the three molecules and the NiO electrode surface. NiO, besides its known flaws, is still the currently the most employed p-type semiconductor material for these applications. We use here a 5-layer slab exposing the NiO (100) surface, known to be the most stable one. We remove one Ni atom from the central layer to reproduce the p-type character of this material. Even though the hole concentration introduced in our model is higher than the natural concentration occurring in the real oxide, this same model has provided good qualitative results in a previous study for the C343/NiO interface. Moreover, we must also note that our model is far from the real system since several other species that take part in the complex equilibria are missing. However, this has the advantage, typical of computational chemistry, of decoupling the effects of the various species and dissect which one gives which contribution to the overall system. These calculations were carried out with PBC at the PBE+U level, with the VASP code (see computational details).

Figure 2.7 shows the optimized structures on the pNiO model, only the dye and the first two NiO layers under it were allowed to relax, while the rest of the solid was kept at a fixed geometry. For all the dyes we chose a bidentate anchoring mode, that is the most stable one for this anchoring group on NiO (vide supra). Optimizations were carried out in vacuum, then a single point calculation in solvent was done on top of these geometries (using the PCM model as implemented in VASP). From these data, we can have a theoretical prediction of the driving force for the hole injection process. The difference between the Fermi level (that is, the top of the valence band) and the HOMO of the adsorbed dye gives us such value. The pDOS depicted in Figure 2.8 show very clearly this information.

In all cases the Fermi level crosses the valence band of NiO, as expected for a p-

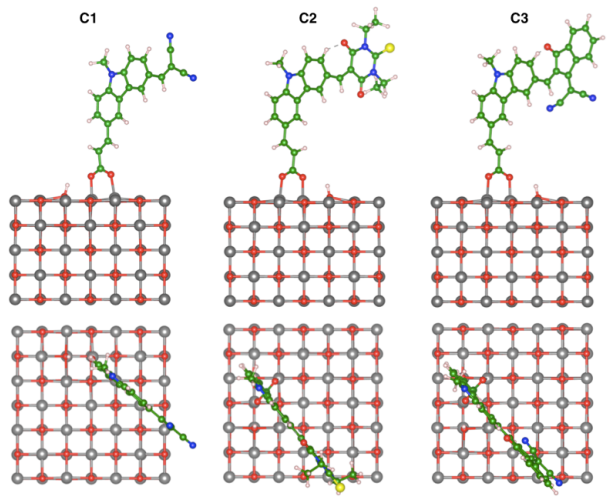

Figure 2.7: Dyes anchored on the 5-layer p-type NiO surface slab, side view (top) and top view (bottom). All the dyes are anchored through the carboxylate group in a bidentate configuration. Colour legend: C green, O red, Ni grey, N blue, H white, S yellow.

type semiconductor. The hole injection driving force is defined as $\Delta E = E_{HOMO} - E_F$, as follows from an electron transfer from the VB of the semiconductor to the HOMO of the dye. This driving force does not account for the kinetic parameters of the actual charge transfer process, but is just a thermodynamic parameter. However, this parameter has been widely accepted as a good approximation and provides valuable information when comparing different dyes [67,125]. **C2** and **C3** present very similar ΔE values, while the hole injection driving force for the **C1** is significantly more convenient than for the other two: -0.73 eV versus $\sim$ -0.54: an improvement of $\sim$35%. A large ΔE means a more efficient driving fore, that is important to reach high PCEs, since the J_{SC} is directly dependent on it. The best choice seems to be now **C1**, with the trend being **C1**>**C2**$\sim$**C3**. The correlation between PCEs and hole injection efficiency is not linear. However, there is a general tendency to higher PCEs with better hole injection processes. We believe this to be particularly true for the three dyes under examination, that are only different in the acceptor group. The process that competes with hole injection is electron recombination: an electron transfer from the LUMO of the dye to

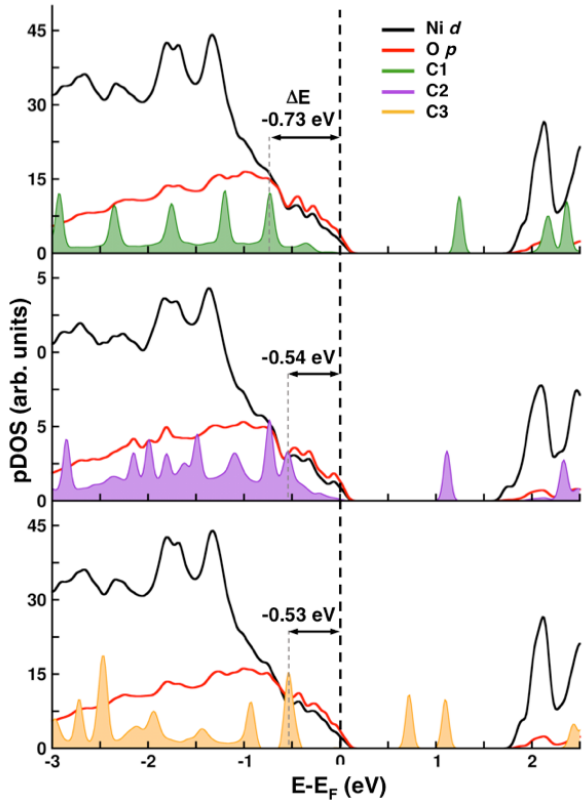

Figure 2.8: Atom- and angular-momentum projected density of states of C1 (top) C2 (middle) and C3 (bottom) adsorbed on NiO. Colour code is displayed in the legend in the upper right corner. The Fermi energy (E_F) set to zero. Solid black arrows indicate the distance from the last populated peak of the molecules and the Fermi level (i.e. the ΔE for hole injection).

the semiconductor. A thorough investigation of this process is computationally cumbersome and beyond our purpose. Push-pull dyes try to suppress this process localizing the LUMO far away from the surface. We can have a qualitative look at this distance that has been shown both experimentally and computationally [126–128] to be correlated to the rate of recombination. Figure 2.9 depicts the projected density of the LUMO of the dye on NiO.

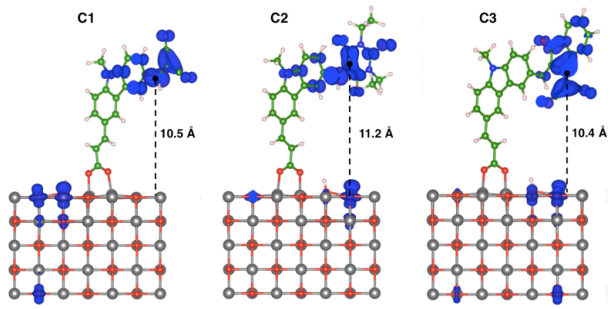

Figure 2.9: Distance between the surface of NiO and the centroid of the dye LUMO, defined as in ref. 50 (in the image the isodensity surface level is set to 0.0025 a.u.). Colour legend as in Figure 2.7

In each case the LUMO band is strongly localized on the acceptor groups, far away from the surface. We have measured the distances from the centroid of the densities and surface. The computed distances are similar from all the three dyes and suggest that recombination is not likely to occur.

p-DSSC devices based on C1, C2 and C3 The group of Prof. Gerbaldi at the Polytechnic of Turin has carried out a proof-of-principle study on the suitability of these dyes in p-DSSC applications. They have sensitized NiO with **C1**, **C2** and **C3** and measured J-V curves and the corresponding photoelectrochemical parameters (J_{SC}, V_{OC} FF, PCE) reported in Figure 2.10 and listed in Table 2.5, respectively. We refer again the interested reader to the work published on the subject for further experimental details [123].

The PCEs are not high, but consistent with state-of-art p-type DSSC devices with similar electrode preparation and the reference **P1** dye (PCE $\sim$ 0.05 %) [129, 130] and other carbazole based dyes. [131] Interestingly, **C1** outperforms

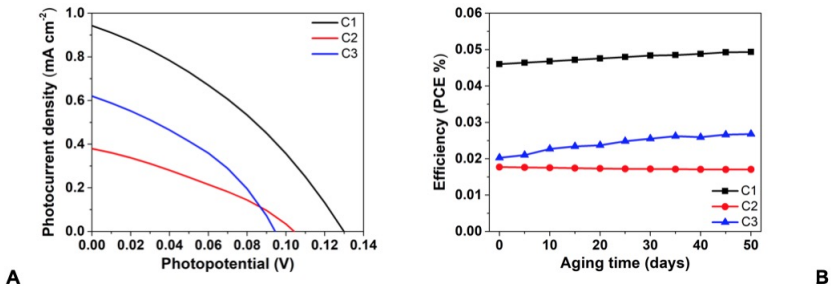

Figure 2.10: (A) Characteristic J-V curves of the NiO-based p-DSSCs with C1, C2 and C3 sensitizers. (B) PCE vs. aging time under ambient temperature/light for NiO-based p-DSSCs with C1, C2 and C3 sensitizers.

Table 2.5: Comparison of the main photovoltaic parameters obtained from the J-V curves of the p-DSSCs with differently sensitized NiO electrodes.

	$V_{OC}(mV)$		$J_{SC}(mAcm^{-1})$		$FF(\%)$		$PCE(\%)$	
	1d	50d	1d	50d	1d	50d	1d	50d
C1	132	141	0.942	0.946	37.0	37.0	0.046	0.049
C2	104	118	0.380	0.280	44.8	51.7	0.018	0.017
C3	93	132	0.620	0.590	35.2	34.4	0.020	0.027

the other two dyes in terms of photocurrent and potential, as predicted by the theoretical analysis of the interface. It is also interesting that all the three systems have shown great stability under ambient light and temperature for 50 days. **C1** and **C3** showed a surprising improvement of their efficiency during the first month, probably due to optimization of electrode wetting by the electrolyte.

Computational Details The ground state optimization, vibrational frequencies and molecular orbital energy levels were computed with the PBE0 hybrid functional [58]. To characterize the excited state properties we employed the CAM-B3LYP functional [132]. A TZVP vasis set was used for all the atoms [133]. These calculations were run in acetonitrile solvent described by the polarizable continuum model (PCM) [52] with $\epsilon = 35.688$. We analyzed the extent of the intramolecular charge transfer upon excitation with the method developed by Le Bahers *et al.* [124] In the periodic calculation on the NiO vacuum slab, an *ab initio* derived value of 3.8 eV for the U-J on Ni d orbitals was chosen [134–136]. We modelled the p-type character of NiO by removing a neutral Ni atom from the 3x3 - 5 layer slab. We included the solvent effect at the interface with the PCM implicit solvation scheme as implemented in the VASP-sol code [52]. We used a 3x3x1 Γ centered k-point mesh and used a 600 eV kinetic energy cutoff for plane waves.

2.1.2 Cu-based Delafossites

In this section we analyze the properties of this family of Cu(I) oxides as a possible alternative to NiO in p-DSSCs. They are of general formula $CuMO_2$, with M beying a trivalent cation, and are wide band gap semiconductors. The interesting properties of these oxides is that they exhibit a p-type conductivity, while most of the transparent conducting oxides (TCOs) are of n-type character. These two simple properties have attracted attention on these oxides as possible candidates for p-DSSC electrode materials. Since the discovery of their p-type conductivity [137], many have started to look into their properties to investigate whether they could substitute and outperform NiO.

$CuMO_2$ has a crystalline structure composed of MO_6 octahedra with sharing

edges, forming layers that are interconnected by Cu atoms coordinated linearly to two oxygens in two different layers.

Group III (Al, Ga, In) delafossites have been most widely studied, their band gaps were reported to be around 3.6 eV [138]. Different methods of synthesis and the effect of dopants and templating agents on the morphology of the nanoparticles are reported in literature [139,140]. Experimental measurements of their properties seem to suggest that they could indeed be a better choice than NiO in p-DSSCs. An experimental comparison between $CuAlO_2$ and NiO carried out by Nattestad et al. reported a V_{OC} for $CuAlO_2$ of 333 mV and an incident photon conversion efficiency (IPCE) of 4%, higher than the NiO-based device. The performances of delafossites can also be improved by doping them with a divalent cation in the M site (typically Mg^{2+}). This in fact is suggested to enhance the p-type conductivity by increasing the number of charge carriers (holes). However, this strongly depends on the concentration of such defects. Mg-doped $CuGaO_2$ has been reported to increase the photovoltaic yields with low Mg concentrations, but with increasing Mg content structural defects come in to play that hinder the carrier mobility and lower the efficiency [140]. As of today, there are only a few theoretical studies concerning Cu-based delafossites, most of which focus on the characterization of band structure and conductivity mechanism. [84, 141] The role of divalent cation substitutions on the charge reorganization has also been thoroughly investigated [142, 143], suggesting an enhancement of te mixed Cu(I) Cu(II) valence present in these oxides. There are still a number of open issues in these materials. How convenient it is to substitute an atom in an M site with Mg, for different elements; which is the effect of the delafossite surface termination on the valence band edge position, are questions that remain unanswered up to date. In this section, we look into these problems and try to give an answer to these questions. In particular, we investigate the properties of $CuAlO_2$, $CuGaO_2$ and $CuCrO_2$, which are some of the most studied systems in literature. We analyze the structure and charge distributions and have a look at the effects of Mg doping. We provide a prediciton of valence band edge positions and V_{OC} with respect to some of the most common electrolyte redox couples in DSSC applications. To do that, we model two different orthorhombic surfaces: the (100) and (011) and compute the work function from which we can extract the absolute positions of

the bands [144].

Structural Models Let us briefly illustrate the structural model we used to describe the $CuMO_2$ strucures. The general delafossite structure has two politypes, the 2H and the 3R. [111] Besides the long debate in literature, no significant energy difference has been reported between the two [111, 145]. Most of the studies focus on the 3R politype [84, 137, 140, 146]. X-ray diffraction patterns measured on $CuGaO_2$ show only peaks relative to the 3R phase. In order to be able to compare our work with the existent literature, we chose to investigate the 3R phase too. The 3R type belongs to the $R\bar{3}m$ space group, with a rombohedral symmetry. Figure 2.11 (a) depicts the hexagonal unit cell of a 3R $CuMO_2$. We used such model to describe the three delafossites under examination: $CuAlO_2$, $CuGaO_2$ and $CuCrO_2$.

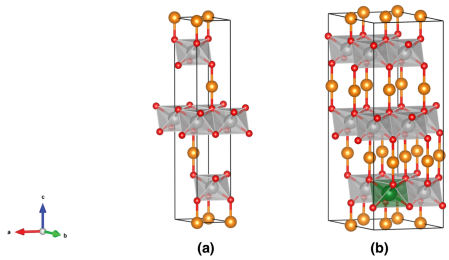

Figure 2.11: Crystal strycture of the 3R $CuMO_2$ hexagonal unit cell (a); 2x2x1 supercell model for $CuM_{1-x}Mg_xO_2$ (with x=0.083). Colour code: Cu (dark orange), M (grey), O (red) and Mg (green)

To reproduce the p-doping, we substituted an atom in the M site with a Mg atom in a 2x2x1 spercell (Figure 2.11 (b)). This way we have a dopant concentration of $8.3\%_{atom}$. As we mentioned before, to be able to evaluate the valence band edge position we need to model the surface of the nanoparticles. We did this with a vacuum slab model, cutting from the bulk shown before the (100) and (011) orthorhombic surfaces. These correspond to the hexagonal $(11\bar{2}0)$ and $(01\bar{1}2)$ surfaces, respectively. We built a surface slab with 5 atomic layers and 10Å and 14Å of vacum for the (100) and (011) surfaces, respectively. Such slab models

are depicted in Figure 2.12. Please note that in the case of $CuCrO_2$ the surfaces were doubled along the b axis to be able to correctly model the antiferromagnetic ordering on the Cr atoms.

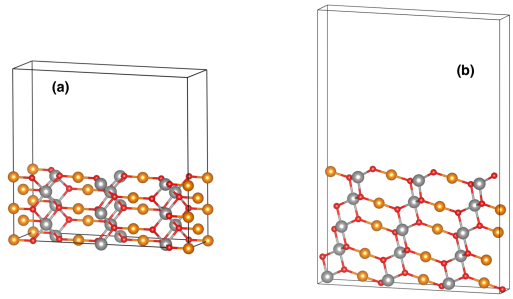

Figure 2.12: Structural models of the $CuAlO_2$ surfaces: (100) orthorhombic surface with 10Å of vacuum (a) and the (011) orthorhombic surface with 14 Å of vacuum (b). Colour code: see Figure 2.11

Optimizations and Electronic Properties As a first step, we have characterized the pristine materials by optimizing the bulk structures. We ran these calculations at the PBE+U level of theory with U-J values of 6.0 and 3.2 eV on Cu(I) [147] and Cr(III) [36], respectively. Both values were taken from literature, the one for Cu has been tuned on the properties of Cu_2O and the one for Cr has been derived via the *ab initio* DFT+U method developed by the Carter group. See the work published on the subject for further details [148]. Table 2.6 lists the structural parameters and bond lengths obtained from the optimizations in comparison with some experimental results taken from literature. Apart from a slight elongation of cell vectors and bond lengths, which is expected from PBE+U, the computed lattice parametes are in good agreement with experimental values. In most cases the error is below 1%, it goes up to 3% for the c-axis of $CuGaO_2$ and $CuCrO_2$, which is still accurate enough for our purposes. If we go from Al to Ga to Cr, we notice an elongation of the M-O bonds, and an expansion of the unit cell. This can be explained by the different size of the ions. According to Shannon's radii, Al^{3+} in this coordination has a radius of 0.535 Å, smaller than the ones of Ga and Cr: 0.620 and 0.615 Å, respectively [149]. The higher cell volume can be

explained with an expansion of the octahedral cavities in the oxygen sublattice to accommodate the larger ions; the Cu-O bond lengths remain in fact essentially the same.

As we remarked already a few times, the band gap is a fundamental property for photoelectrochemical applications. The optical gaps of the Cu-based delafossite family increase going down the III group. A gap of 3.5 eV was reported for $CuAlO_2$ [138, 150], of 3.6 eV for $CuGaO_2$ [151] and of 3.9 eV for $CuInO_2$ [152]. This trend is in contrast with the one observed for group III semiconductors [153]. However, the fundamental gap of $CuMO_2$ is at the Γ point and it is optically forbidden. The value of such gap does respect the trend observed in other group III semiconductors. The nature of the optical band gap in these materials is still much debated in literature [139, 146, 153]. It is beyond our purpose to take part in such debate, but we refer the interested reader to a recent theoretical study on the matter [84].

Table 2.6: 3R $CuMO_2$ (M = Al, Ga, Cr) bulk parameters: lattice vectors (a, c) and bond lengths (d_{Cu-O} and d_{M-O}) obtained from the PBE+U optimizations. Experimental values are reported in parenthesis for comparison

	a(Å)	c(Å)	d_{Cu-O}(Å)	d_{M-O}(Å)
$CuAlO_2$	2.88(2.86)	17.06(16.95)	1.87(1.86)	1.92(1.92)
$CuGaO_2$	2.98(2.97)	17.64(17.17)	1.88(1.85)	2.02(1.99)
$CuCrO_2$	2.97(2.97)	17.63(17.10)	1.88	2.02

Table 2.7: Eigenvalue gaps computed at the PBE+U and HSE06 levels of theory on the structures optimized at the PBE+U level compared with similar calculations in literature reported in parentheses. Magnetic moments on Cu and M from the HSE06 single points

	E_{egn}^{PBE+U}	E_{egn}^{HSE}	$\mu_{Cu}(\mu_B)$	$\mu_M(\mu_B)$
$CuAlO_2$	2.24	3.35(3.4)	0	0
$CuGaO_2$	1.09	2.10(2.2)	0	0
$CuCrO_2$	1.88	2.83(3.1)	0	2.96

Table 2.7 lists our calculated gaps at both PBE+U and HSE06 levels of theory

compared with literature. As expected, PBE+U underestimates the eigenvalue gap. The inclusion of a 25% exact exchange with the HSE functional increases this gap thanks to the more consistent removal of the self interaction error. Our results are in good agreement with the available reference data. At this point, we should point out that to accurately determine band gaps DFT calculations are not an efficient method. To get a more reliable value we should use a higher level of theory, for example a GW in the quasiparticle formalism. Still, these calculations are very expensive and a precise evaluation of the eigenvalue gaps is out of the focus of this thesis. It is also worth noticing that, among all three delafossites, $CuCrO_2$ only has a non-zero magnetic moment due to the d^3 configuration of the outer shell of Cr(III). We considered an anti-ferromagnetic ordering as in other Cr(III) oxides [36, 154].

We investigated the substitution of an Mg^{2+} cation on the optimized 3R structures described above. In order to model a not too high concentration of Mg, we doubled the delafossite unit cell along the a and b directions. This way, we obatin an $8.3\%_{atom}$ concentration of the dopant. While keeping fixed the lattice parameters (since in real systems dopant concentrations are so low that they do not affect them), we relaxed the ionic positions and the electron density of the system. By doing this substitution we are carrying out a p-doping, we the aim at enhancing the p-type conductivity by increasing the concentration of holes, reinforcing the Cu(I)/Cu(II) mixed valence. To put it in other terms, we start from a $CuM(III)O_2$ and insert a hole in the system substituting M^{3+} with Mg^{2+}. This produces empty states and shifts down the Fermi level of the semiconductor[1].

Figure 2.13 depicts the atom- and angular momentum-projected densities of states (pDOS) of pristine (left panel) and doped (right panel) systems.

Copper d states give the major contribution to the valence band edge. The p states of oxygen are instead the main components of the conduction band in $CuAlO_2$ and $CuGaO_2$, while in $CuCrO_2$ the d bands of Cr become dominant in this region. The way the p states of Oxygen and d states of Chromium overlap suggests a certain degree of hybridization between them. Also in $CuGaO_2$ a certain

[1]We are well aware of the fact that the "Fermi level" in semiconductors is not well defined. The VASP code takes the last occupied level in semiconductors as the Fermi level. For practical reasons, we use the same convention throughout this thesis

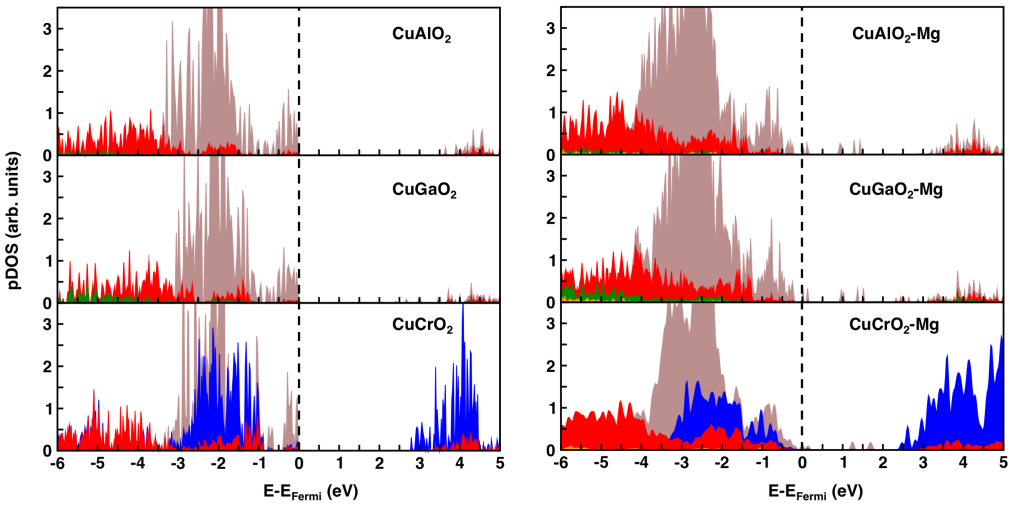

Figure 2.13: Atom- angular momentum-projected densities of states (pDOS) of pristine (left panels) and Mg-doped (right panels) of $CuAlO_2$ (top), $CuGaO_2$ (middle) and $CuCrO_2$ (bottom). Colour code: Cu d (brown), O p (red), M p (green), Cr d (blue), and Mg s (orange).

degree of hybridization between O p and Ga p is present. This indicates a greater covalent character in the M-O bonds in these two systems with respect to $CuAlO_2$. When introducing the dopant in these systems, some states appear in the band gap. These belong to Cu d bands, which confirms that the greatest part of the charge introduced in the system is accepted by Cu ions. The Cu(I)/Cu(II) mixed valence is so reinforced. However, the presence of such states could have two drawbacks: i) light absorption phenomena might occur, interfering with the molecular antenna (i.e. the dye) ii) they can generate undesired charge recombination processes. Table 2.8 lists the charges around the atoms according to Bader's partition. [155] The charge analysis perfectly agrees with the results in the pDOS.

As expected, we can see from the charges a somewhat different picture from the competely ionic one, that we are used to think of (i.e. $Cu^{+}M^{3+}O_2^{2+}$). Moving from Al to Ga to Cr, the systems are less ionic. Since the hole introduced via Mg doping is delocalized, mostly on Cu atoms, only small variations of the average Bader charges are observed in the doped systems. The last two entries in Table

Table 2.8: Bader's effective atomic charges computed on the HSE06 electronic densities of pristine and Mg-doped $CuMO_2$ (M = Al, Ga, and Cr). The reported net charges (Z_{eff}) correspond to the average values for all the aroms of each element in the delafossite unit cell. Cumulative net charge variations (Δq) are also reported and refer to the difference between the Mg-doped $CuMO_2$ and the pristine delafossite, summed over all the Cu and M sites in the unit cell, respectively (the positive Δq values correspond to the localization of the hole introduced by aliovalent substitution)

		$CuAlO_2$		$CuGaO_2$		$CuCrO_2$	
		Pristine	Mg-doped	Pristine	Mg-doped	Pristine	Mg-doped
Z_{eff}	Cu	0.574	0.610	0.580	0.620	0.590	0.621
	M	2.500	2.500	1.810	1.810	1.750	1.750
	O	-1.537	-1.511	-1.195	-1.209	-1.170	-1.182
	Mg		1.666		1.666		1.666
Δq	Cu	0.542		0.426		0.401	
	M	0.000		0.000		0.000	

2.8 list the total charge variation due to the presence of the dopant atom, summed on all the Cu and M atoms. The charge on Cu increases by about 0.5 in each system, while the M atoms are unaffected. This is consistent with the hole being accepted by the VB of the material (composed of filled Cu d orbitals) and it can be described as some Cu(I) being oxidized to Cu(II).

Another important feature to understand is how favourable is this aliovalent substitution. The synthesis of delafossites is usually carried out under hydrothermal conditions from the hydrated nitrates of the metals [140, 156]. Adding some $Mg(NO_3)_2{\cdot}(H_2O)_6$ in the reaction environment is a way to introduce the dopant in these systems.

Since this process is nearly impossible to simulate, in order to evaluate the different stability of the Mg cation in the three different delafossites, we considered an ideal Mg_M substitution under the delafossite thermodynamic stability conditions in an oxygen-rich environment [157–159]. Table 2.9 lists the substitution energies computed as:

$$\Delta H_D = E_D - E_H - \sum_i n_i \mu_i \tag{2.2}$$

where E_D and E_H are the total energies of the supercell containing the defect and the pristine host, respectively. The sum runs over all the chemical potentials of the elements that are added ($n_i > 0$) and removed ($n_i < 0$) to/from the host.

Table 2.9: Substitution energies (ΔH_D) for Mg-doped delafossites, computed according to equation 2.2 in an O-rich environment; average Cu-O, M-O and Mg-O bond lengths in Å for the Mg-doped $CuMO_2$ delafossites

	ΔH_D (eV)	d_{Cu-O} (Å)	d_{M-O} (Å)	d_{Mg-O} (Å)
Mg:$CuAlO_2$	0.40	1.86	2.01	2.01
Mg:$CuGaO_2$	0.29	1.88	2.06	2.06
Mg:$CuCrO_2$	1.44	1.87	2.06	2.06

We considered only an oxygen rich limit environment to compute the chemical potential and the defect formation energies. Other conditions are irrelevant for applications in p-DSSCs. The trend in defect formation energies that can be observed in Table 2.9 is Ga < Al < Cr. Two main factors influence the defect formation energies and can help us rationalize this trend: i) M-O bond strengths and ii) Structural rearrangement. Mg^{2+} has an ionic radius of 0.72 Å, which introduces a larger perturbation in the lattice when substituting the small Al^{3+} cation than the larger Ga^{3+}. We can observe this effect from the elongation of the average Al-O bond distances of ~ 0.1 Å from 1.92 Å (Table 2.6) to 2.01 (Table 2.9), while the elongation in the case of Ga is only 0.04 Å. While the above argument can explain the slightly higher defect formation energy in $CuAlO_2$ with respect to $CuGaO_2$, it cannot account for the incredibly high energy needed to substitute a Cr with a Mg. Here, it is the different nature of the M-O bonds that comes into play. It is well known that early transition metals have the tendency to form very strong M-O bonds [154]: it is more expensive to break a Cr-O bond than M-O bonds involving later transtion metals in the same period (the so-called oxo-wall effect) [160]. Hence, the computed ΔH_Ds reflect the energy loss in substituting the stronger Cr-O bonds or the weaker Ga-O bonds with Mg-O bonds. Among the

three delafossites studied, $CuGaO_2$ should be more easily doped than the other two.

To investigate if $CuMO_2$ oxides are suitable for p-DSSC applications, one key parameter we can compute is the valence band (VB) edge position. From this value is in fact possible to compute the V_{OC} of a cell, which is given by the difference between the VB_{edge} and the redox potential of the redox couple of choice. Another key parameter that strongly depends on the VB_{edge} position is the driving force for the process of hole injection from the HOMO of the dye to the valence band of the semiconductor. To compute the absolute position of VB_{edge}, we modelled two different stoichiometric orthorhombic surface slabs built from the optimized bulk structures: the (100) and the (011) surface slabs that correspond to the $(10\bar{1}0)$ hexagonal surfaces, respectively (Figure 2.12). The surface energies, computed as:

$$E_{surf} = \frac{E_{slab} - nE_{bulk}}{2S} \tag{2.3}$$

where n is the ratio between the formula units in the slab and in the bulk and S is the surface area, are listed in Table 2.10

Table 2.10: Surface energies in Jm^{-2} of the (011) and (100) surfaces calculated according to equation 2.3 as detailed in text

$E_{surf}(Jm^{-2})$	$CuAlO_2$	$CuGaO_2$	$CuCrO_2$
(011)	1.00	0.75	1.09
(100)	1.48	1.10	1.26

Experimental observations indicate that the crystals grow exposing mostly the (011) surface [139]. Consistently, we compute a lower surface energy for it with respect to the (100). For these reasons, we chose this surface to compute the absolute position of the valence band edge. We obtained such value by correcting the band gap center (BGC) with the energy of the vacuum (E_{vac}) and subtracting a half of the eigenvalue gap, according to:

$$VB_{edge} = BGC - E_{vac} - \frac{1}{2}E_{egn} \tag{2.4}$$

If the Fermi level is taken as the last occupied level, this value corresponds

to the negative of the workfunction. Even though PBE+U does not reproduce correctly the band gap, the band gap centre should be accurate enough to be used in such calculations [161]. From the position of the valence band edge, we can calculate the V_{oc} of an hypotetical cell built with this semiconductor and an electrolyte of choice. Figure 2.14 shows such $V_{oc}s$ for all the three delafossites under study and for NiO with respect to three different redox couples; namely, I_3^-/I^-, $[Co(bpy)_3]^{2+/3+}$ and $[Cu(bpye)_2]^{+/2+}$. The first one is the standard choice in such devices, while the other two have been proposed more recently and shown a reduced potential loss [162–164].

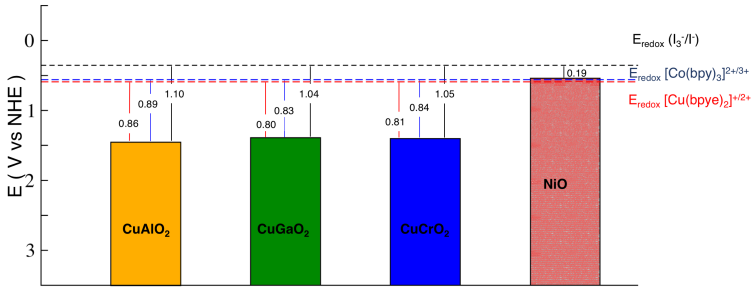

Figure 2.14: Absolute positions of the VB edges of delafossites and NiO. Dashed lines represent the redox potentials of the three electrolytes: I_3^-/I^-, $[Co(bpy)_3]^{2+/3+}$ and $[Cu(bpye)_2]^{+/2+}$. Solid lines represent the V_{OC} values in V vs NHE.

Before discussing the values, a caveat is needed. In the real device, there might be a shift of the VB_{edge} due to the band bending induced by the interface with the dye or solvent molecules that we are neglecting here. At this point, we do not wish to draw any quantitative conclusion but just to extract a trend between the performances of different materials in order to select a good candidate for p-DSSC operation. Once a good material has been selected, one may proceed to the accurate evaluation of all the parameters that are relevant for the performance of

the device.

The differences among the delafossite systems is very small: 1.44 V (vs. NHE) for $CuAlO_2$, 1.38 V for $CuGaO_2$, and 1.39 V for $CuCrO_2$. This is not unexpected, given that the valence band is mainly composed by the d orbitals of Cu. With the standard I_3^-/I^-, NiO gives a smaller V_{oc} than the delafossite systems. With the "newer" redox couples, NiO could not even be used! In conclusion, our data suggest that copper delafossites may outperform NiO in p-DSSC applications, at least in terms of cell voltage. Among the delafossites systems, no major difference is noted. If we had to select one, $CuGaO_2$ would be our choice, thanks to its higher band gap and lower Mg doping energy

Computational Details For the DFT+U calculations on $CuMO_2$ (M = Al, Ga, Cr) delafossites we used the theoretically derived values of 6.0 and 3.2 eV for Cu(I) [147] and Cr(III) [36], respectively. The first being tuned to provide the best structural and electronic properties of Cu_2O, and the second being computed via the *ab initio* method developed in the Carter group [36]. The kinetic energy cutoff used in all calculations was 800 eV and the reciprocal space was sampled via a 8x8x2, Γ-centered k-point mesh. Such parameters were converged on the total electronic energy with a threshold of 3 *meV/f.u.*. Structural optimizations for lattice vectors and ionic positions were carried out until the maximum forces on each atom were lower than 10 meV $Å^{-1}$

2.1.3 Dye anchoring on $CuGaO_2$

Building up from the semiconducting part of the electrode alone towards a model system that is closer to the real one, we need to account for the anchoring of the dye to the SC surface. For this purpose, we model the binding of two of the most widely employed dye anchoring groups i.e. carboxilic and phosphonic acid on $CuGaO_2$. Before doing so, we must take a step back and look again at the effect that a Mg doping has on these materials and in particular on $CuGaO_2$. Renaud *et al.* have measured an increase in the specific surface area (SSA) of the nanoparticles when a Mg concentration below 1% is present [140]. This results in higher efficiency. Increasing Mg concentration up to 5% results in a further increase in the SSA

but has no effect on the photocurrent and a decrease in V_{OC} [83]. To understand this behaviour we have computed the VB edge positions of $CuGaO_2$ at varying concentrations of Mg doping. This can help us dissect the role of the doping on the variation of V_{OC}, excluding other defects and structural factors that can occur in the measurement. In particular, we have considered two Mg concentrations: 3.3 and 6.7%, by substituting one Ga atom from a 5-layer slab with (2x1) and (1x1) periodicity, respectively. VB edges are depicted in Figure 2.15 in comparison with pristine $CuGaO_2$ and NiO.

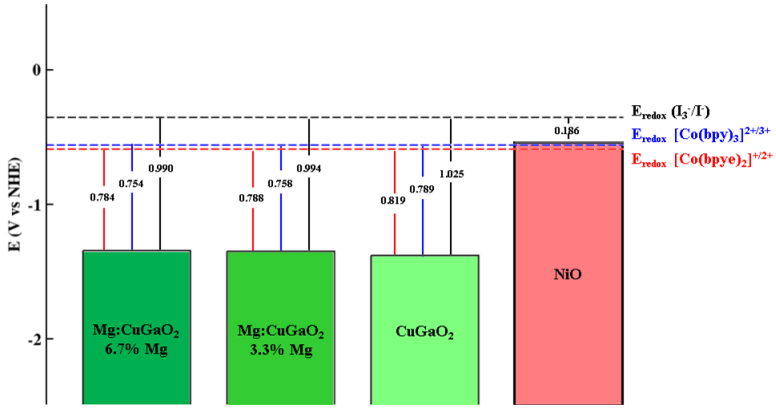

Figure 2.15: Calculated absolute positions of the valence band edges for, from left to right: Mg:$CuGaO_2$ with two different dopant concentrations (i.e. 3.3% and 6.7%), undoped $CuGaO_2$ and NiO. Dashed lines represent the redox potentials of the three electrolytes: I_3^-/I^-, $[Co(bpy)_3]^{2+/3+}$ and $[Cu(bpye)_2]^{+/2+}$. Solid lines represent the V_{OC} values in V vs NHE

We also indicate the V_{OC} with respect to different redox couples, all computed in acetonitrile solution. We refer the interested reader to the following references: [162–164] for the exact compositions of the electrolyte solutions. With respect to the pristine oxide, 3.3% Mg doped $CuGaO_2$ has a VB edge 29 meV higher, rising by 4 more meV when we increase the concentration to 6.7%. The order of magnitude is the same of the experimental values reported by Renaud et al. [140] where they

observe a decrease of V_{OC} of 30 meV with respect to the undoped case and a further decrease of 10 meV occurse then doping is increased up to 5%. Besides this low increase in VB edge with Mg doping, the V_{OC}s of Mg:$CuGaO_2$ are still much higher than those of NiO with respect to all the electrolytes proposed. It is however important to point out that this is just a qualitative picture, since many factors that affect the band allignement are missing (e.g. solvent, band bending at the interfacem effect of ionic species, etc.). Still, the computed trend is consistent with experimental values [87].

It is of paramount importance to understand how the dye anchors to the surface of the semiconductor. A higher dye coverage provides a better photoconversion efficiency and a stronger adsorption provides a more durable electrode. In the case of protic anchoring groups, the analysis of different anchoring modes can help predict the resulting efficiencies, since different anchoring groups can yield different band alignements between the HOMO of the dye and the VB edge of the p-semiconductor. We have investigated all the possible anchoring modes of -COOH and -PO_3H_2 on the $CuGaO_2$ (011) surface. We take into account different coordination sites and their combinations. We have considered monodentate anchoring on Ga or Cu surface atoms (M-Ga and M-Cu), bidentate binding on two Ga atoms, two Cu atoms and one of each (B-Ga-Ga, B-Cu-Cu and B-Ga-Cu). For -PO_3H_2 we had to consider also the two possible tridentate bindings: one Cu and two Ga and one Ga and two Cu (T-Ga-Ga-Cu and T-Cu-Cu-Ga). In the case of monodentate anchorings, when the -OH group forms an hydrogen bond with a surface oxygen, we have added a sub index "H". In the multidentate cases, the H atoms are bound to oxygen atoms on the surface as far as possible from the rest of the anchoring group. Figure 2.16 depicts the anchoring geometries outlined above and Table 2.11 lists selected structural parameters and binding energies E_{ads}.

The adsorbed CH_3COOH molecule does not change much when adsorbed on NiO or the delafossite surface. The Ga-O1 distance is very similar to the Ni-O1 distance, both being similar to the metal-oxygen distances in the respective oxides. A difference is observed in $CuGaO_2$ when the oxygen is adsorbed on Cu or Ga, with the latter being closer at the equilibrium. The Cu-O1 distance is in fact significantly longer than the Cu-O distance in the oxide. The hydrogen bonds between the -OH group and the metals in surface are slightly longer in $CuGaO_2$

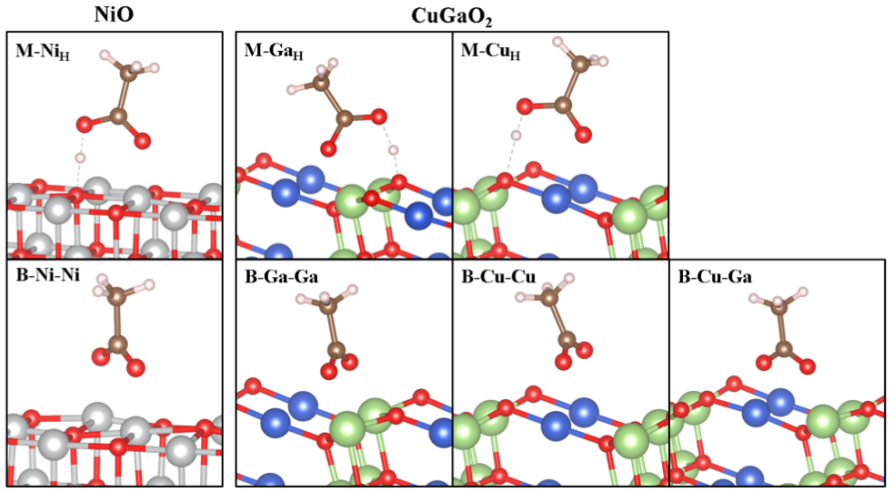

Figure 2.16: Optimized structures of CH_3COOH on $CuGaO_2$ (011) 2x1x3L slav (right) and on NiO (001) (left). Labels according to the anchoring modes [monodentate = M and bidentate = B] and to the surface atoms involved in the adsorption process. Sub index "H" indicates H bonding (dashed grey line) between the OH group and surface oxygen atom upon relaxation in M cases. Colour legend: Ni (gray), Cu (blue), Ga (green), O (red), C (brown)

Table 2.11: Selected structural parameters for relaxed CH_3COOH anchored on $CuGaO_2$ (011) and on NiO (001) together with those of the isolated molecule calculated at the DFT-PBE+U level of theory in vacuum

CH_3COOH - Main structural parameters (Å)									
Anchoring mode	d_{O1-C}	d_{O2-C}	d_{O-H}						$E_{ads}(eV)$
Isolated	1.22	1.36	9.98						
On NiO(001)				d_{O1-Ni}		d_{O2-Ni}		d_{H-Os}	
M-Ni_H	1.26	1.38	1.15	2.05		2.05		1.31	-0.81
B-Ni-Ni_H	1.27	1.29	-	2.01		2.01		-	-0.88
On $CuGaO_2$(011)				d_{O1-Ga}	d_{O1-Cu}	d_{O2-Ga}	d_{O2-Cu}	d_{H-Os}	
M-Ga_H	1.28	1.38	1.29	2.03	-	-	-	1.56	-0.76
M-Cu_H	1.24	1.33	1.03	-	2.38	-	-	1.60	-0.19
B-Ga-Ga	1.28	1.28	-	2.03	-	2.05	-	-	0.52
B-Cu-Cu	1.25	1.27	-	-	1.93	-	1.94	-	1.60
B-Ga-Cu	1.26	1.28	-	2.03	-	-	1.95	-	0.72

with respect to NiO. In bidentate anchoring, we obtain two equal M-O distances for B-Ga-Ga and B-Cu-Cu cases on $CuGaO_2$ and B-Ni-Ni on NiO, since the two oxygen atoms of CH_3COOH become equivalent. In this case, the Cu-O1 distances are much smaller than in the monodentate binding and closer to the Copper - Oxygen bonds in bulk $CuGaO_2$. In mixed bidentate anchoring (i.e. B-Ga-Cu), the M-O bonds to the different metals differ, but they assume the same value as in the respective non-mixed anchoring. Even though $CuGaO_2$ (011) and NiO (001) have very different surface patterns, the M-M bonds in the two solids are very similar (i.e. $d(Ni-Ni)_{NiO}$=2.99 Å and $d(Ga-Ga)_{CuGaO_2} = d(Cu-Cu)_{CuGaO_2}$=2.98Å), which explains the similarities in the binding geometries. The only significant difference is a slight tilting of the C-C bond with respect to the z axis due to the non-planar pattern of the surface of the delafossite. The similarities in adsorption geometries are not reflected on the binding energies, that are very different instead. In NiO, E_{ads} for both mono- and bidentate anchoring modes are negative and very close in energy, with the former being only 0.07 eV more stable than the latter. One important thing to note is that the binding energies indicated in Table 2.11 for CH_3COOH and in Table 2.12 for $CH_3PO_3H_2$ on NiO are very close to those computed considering a full C343 dye and reproduce the same trend [125]. Hence, we can consider the CH_3- capping to be a good approximation for the study of the anchoring groups on the surfaces of the oxides. While the two binding energies in NiO suggest that we would find the oxide covered by the dye in a roughly equal ratio of the two binding modes, in $CuGaO_2$ we observe a strong preference of one of the two anchoring modes. In particular, M binding is the only favourable anchoring. We also observe a strong preference for Ga with respect to Cu, with the values of M-Ga_H being close to those for M-Ni (and B-Ni-Ni). This is consistent with the trend of transition metal-oxo complex dissociation energies (BDE) [165] of Ni-O and Ga-O (-366 and -374 KJ mol$^-$1), with a smaller value for Cu-O BDE (-287 KJ mol^{-1}). The energy difference is increased by the fact that surface Cu retain their bulk coordination with two oxygen atoms, while Ni and Ga are undercoordinated.

In an analogous way, we analyse all the possible binding energies of $CH_3PO_3H_2$. This time we must include also tridentate (T) binding modes. Optimized geometries are shown in Figure 2.17 and structural parameters and binding energies are

listed in Table 2.12

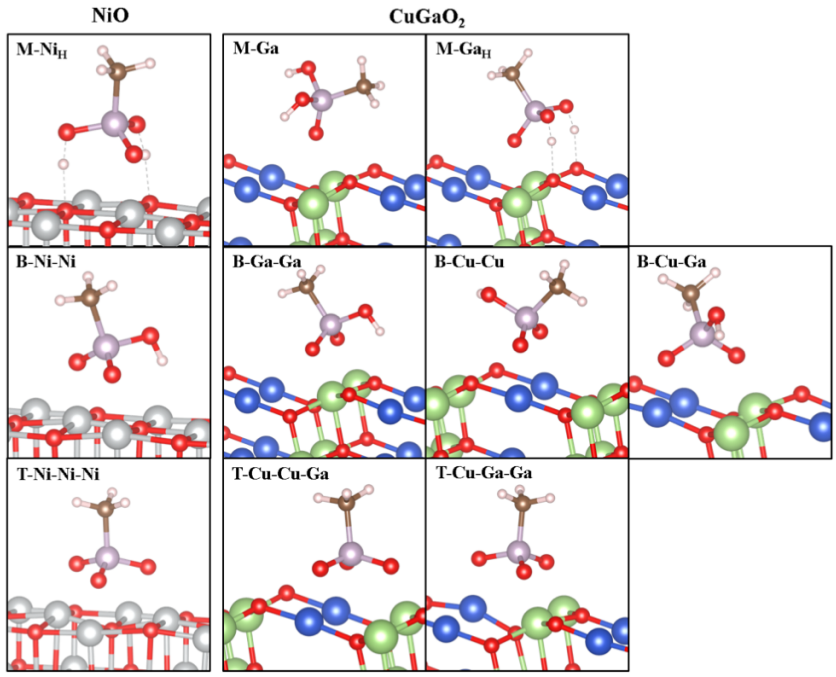

Figure 2.17: Optimized structures of $CH_3PO_3H_2$ on $CuGaO_2$ (011) 2x1x3L slab (rigt) and comparison to NiO (001) (left). Labels according to the anchoring mode [monodentate (M), bidentate (B) and tridentate (T)] and to the surface atoms involved in the adsorption process. Sub index "H" indicates H bonding (dashed gray line betwen the OH group and surface oxygen atom upon relaxation in M cases. Colour code: see Figure 2.16

In this case, only the monodentate adsorption modes on surface Ga atoms are negative. In particular, there are two stable M structures, one with both -OH groups forming hydrogen bonds with the surface Oxygen atoms (M-Ga_H) and one without any hydrogen bonds (M-Ga). The former is stabilized by 0.92 eV by these bonds with respect to the other one. All the different starting points

Table 2.12: Selected structural parameters for relaxed $CH_3PO_3H_2$ anchored on $CuGaO_2$ (011) and on NiO (001) together with those of the isolated molecule calculated at the DFT-PBE+U level of theory in vacuum

	$CH_3PO_3H_2$ - Main structural parameters (Å)										$E_{ads}(eV)$
Anchoring mode	d_{O1-P}	d_{O2-P}	d_{O3-P}	d^*_{O-H}							
Isolated	1.48	1.61	1.62	0.98							
On NiO(001)					d_{O1-Ni}		d_{O2-Ni}		d_{O3-Ni}	d^*_{H-Os}	
M-Ni_H	1.51	1.58	1.59	1.05	2.05		-		-	1.58	-1.08
B-Ni-Ni	1.53	1.53	1.63	0.98	2.00		2.00		-		-1.18
T-Ni-Ni-Ni	1.55	1.55	1.59	-	2.03		2.04		1.98	-	-1.08
On $CuGaO_2$(011)					d_{O1-Ga}	d_{O1-Cu}	d_{O2-Ga}	d_{O2-Cu}	d_{O3-Cu}	d_{H-Os}	
M-Ga	1.50	1.60	1.61	0.97	2.18	-	-	-	-	-	-0.13
M-Ga_H	1.53	1.58	1.58	1.04	2.03	-	-	-	-	1.60	-1.05
B-Ga-Ga	1.53	1.54	1.61	0.99	2.00	-	2.02	-	-	2.13	0.03
B-Cu-Cu	1.48	1.52	1.64	0.98	-	1.99	-	2.14	-	-	1.38
B-Ga-Cu	1.50	1.55	1.64	0.98	1.99	-	-	1.91	-	-	0.55
T-Ga-Ga-Cu	1.54	1.55	1.56	-	1.96	-	1.97	-	1.88	-	2.25
T-Cu-Cu-Ga	1.50	1.55	1.57	-	-	1.91	1.92	-	1.84	-	3.03

of the geometrical optimizations we have tried end up in the same two minima (i.e. M-Ga$_H$ and M-Ga). As in the case of acetate, we observe that NiO has a similar binding energy for all the different anchorings. On the delafossite we observe instead once again a strong preference for the monodentate one. From this we can assume that the molecules will only be found in such geometries on the surface.

In order to analyze the effect of the solvent and of the Mg doping on the selectivity towards monodentate binding, we have calculated the adsorption energy of each anchoring mode (for both anchoring groups) in acetonitrile solvent, on the doped surface (3.3% Mg), and on the doped surface in solvent. The solvent of choice was acetonitrile since it is the most commonly used in DSSCs. These three additional sets of E_{ads} are listed in Table 2.13 together with those on the pristine slab in vacuum listed above.

Table 2.13: Calculated adsorption energies (E_{ads}) for CH_3COOH and $CH_3PO_3H_2$ on CuGaO2 (001) at the DFT(PBE)+U level of theory in vacuum and acetonitrile (implicit solvent), without and with Mg doping (3.3%).

		$E_{ads}(eV)$			
Anchoring group	Anchoring mode	$CuGaO_2$ vacuum	Mg:$CuGaO_2$ vacuum	$CuGaO_2$ acetonitrile	Mg:$CuGaO_2$
CH_3COOH					
	M-Ga$_H$	**-0.765**	**-1.150**	**-0.580**	**-0.776**
	M-Cu$_H$	**-0.191**	**-0.663**	0.233	**-0.360**
	B-Ga-Ga	0.516	0.114	0.434	0.139
	B-Cu-Cu	1.597	1.741	1.926	0.357
	B-Cu-Ga	0.715	0.460	0.928	0.334
$CH_3PO_3H_2$					
	M-Ga	**-0.128**	**-0.646**	-0.160	**-0.121**
	M-Ga$_H$	**-1.050**	**-1.638**	**-0.525**	**-1.121**
	B-Ga-Ga	0.026	0.077	0.041	0.019
	B-Cu-Cu	1.378	0.854	1.935	1.219
	B-Cu-Ga	0.548	0.307	0.547	0.333
	T-Ga-Ga-Cu	2.253	2.492	1.764	1.512
	T-Cu-Cu-Ga	3.030	2.546	2.656	1.756

Both acetic and phosphonic acid are much more strongly bound to the Mg-doped surface, with a decrease in energy of about half an eV. In very few cases a small increase is observed ($\sim 0.05eV$) upon Mg-doping (e.g. CH_3COOH-B-Cu-Cu and $Ch_3PO_3H_2$-B-Ga-Ga/T-Ga-Ga-Cu). The p-doping of these surfaces makes them more Lewis-acidic thanks to the introduction of a hole that enhances their affinity for electron-donating species, which explains the stronger binding [166]. The uniform decrease in E_{ads} in all surface sites and not only on Cu can be explained with the fact that the hole introduced by Mg doping is not localized on any specific Cu, but is spread over all Cu atoms, as we have shown above to happen also in $CuGaO_2$ bulk [148].

The opposite effect is induced by the solvent, with all the E_{ads} increasing, but not to the same extent. Only in the tridentate cases there is a stabilization of half an eV, which is not enough to stabilize the very unfavourable tridentate anchoring. The acetonitrile solvent, having a mild dielectric constant, weakens the ionic contribution to the bonding between the O of the anchoring groups and the Ga atoms on the surface. In the tridentate modes, we observe instead a stabilization of the dipole moments due to the OH species that are formed on surface upon deprotonation of the acid. In conclusion, the overall picture does not change when we include both Mg doping and acetonitrile solvent, with the adsorption energy values being almost analogous to those computed on the pristine slab in vacuum. There is a strong preference of the M binding for both anchoring groups. This result is of greatest importance for the cell performance, since it has been shown that M binding modes maximize the driving force of the hole injection (i.e. between the HOMO of the dye and the VB of the semiconductor) where no H has been released by the acid and adsorbed on the surface, lowering the dipole [125]. Another important conclusion is that Mg doping does not only improve the p-type conductivity and morphology of the nanoparticles [140], but also improve the dye coverage by increasing the affinity of the delafossite for the anchoring group.

Computational Details As in the calculations on the isolated delafossites, we used a value of 6 eV on the d electrons of Cu [147,167]. SCF Energy convergence threshold was set to 10^{-5} eV, and the forces were converged up to 0.05 eV $Å^{-1}$.

Kinetic energy cutoff for plane waves was set to 750 eV and the Brillouin zone was sampled with a Monkhorst-Pack [168] 6x6x2 k-points grid.

2.1.4 $CuFeO_2$ as a CO_2 reduction reaction catalyst

In the introduction to this chapter, we have already spent time on the importance of the CO_2 reduction reaction (CO2RR) as a route to carbon dioxide recycling into useful chemicals that can be reused in a CO_2-neutral way. We have also extensively discussed the structure and electronic properties of some members of the family of copper delafossites. In this section, we propose $CuFeO_2$ as an efficient catalyst for CO2RR.

Bulk and surface properties The lower band gap of $CuFeO_2$ with respect to the other delafossites explored above makes it uninteresting for p-DSSC applications. Light absorption phenomena would interfere with the molecular antenna, making the cell inefficient. However, such property might be useful for photocatalysis: the excited electrons can be transferred to an adsorbed substrate (CO_2 in our case) and perform a reduction.

Very little has been reported in literature about the doping of this delafossite oxide. Here we report an investigation of the formation of (both, Copper and Iron) vacancies and the effect they have on adsorption, activation and catalysis of CO2RR.

Figure 2.18 depicts the pDOS at the HSE level on top of PBE+U geometries (see Computational section for details) of pristine $CuFeO_2$ (top panel) and of $CuFeO_{2-\delta}$.

Besides a small contribution of the hybridized Fe d and O p states, the valence band is mostly composed of Cu d states. This is in agreement with both photoelectrochemical measurements and theoretical works [113, 114, 169–171].

As we have discussed in Section 2.1.2, the p-type behaviour in these oxides is generally explained as being due to partial oxidation of Cu(I) to Cu(II). No works have been published analyzing the different effects of the different kinds of doping. Since our aim is a reduction reaction, we require an excess of electrons to be transferred from the surface of the catalyst to the target molecule. For this

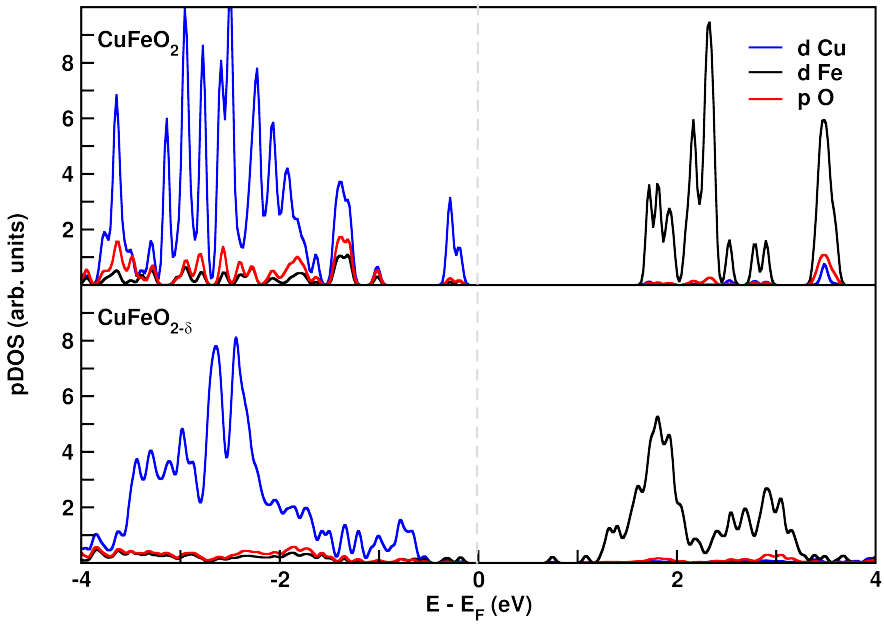

Figure 2.18: Atom- angular momentum-projected density of states (pDOS) at the HSE06 level for 48 atoms ($1 \times \sqrt{3} \times 1$) orthorhombic supercell for $CuFeO_2$ (top panel), $CuFeO_{2-\delta}$ (bottom panel). Cu d-orbitals (blue) give the major contribution to valence band while the major contribution for conduction band is given by Fe d-orbitals (black). The grey dashed line indicates the Fermi energy (E_F). Every graph is scaled by its Fermi energy.

reason, we mainly focused on n-type doping, introducing an oxygen vacancy in the system. With respect to the pristine material, the oxygen vacancy induces a shift of the Fermi level towards the conduction band. The excess of electrons left behind by the O atom causes the reduction of the two neighbouring Fe atoms. From our calculations, we found an effective magnetic moment of 3.9 μ_B against the 4.2 μ_B in the pristine oxide. This indicates formation of a Fe(II) species in the bulk [172]. The computed vacancy formation energies are 3.95 eV for O and 3.31 eV for Cu.

Once again, we are interested in the absolute position of the band edges to asses the activity of our material in photochemical processes. The (011) orthorhombic surface has already been shown to be the most stable one for these oxides, so we build a slab of this surface analogous to the ones used in Section 2.1.2. We used such slab to compute the band gap center, the workfunction and the absolute position of the bands. The slab is shown in Figure 2.19

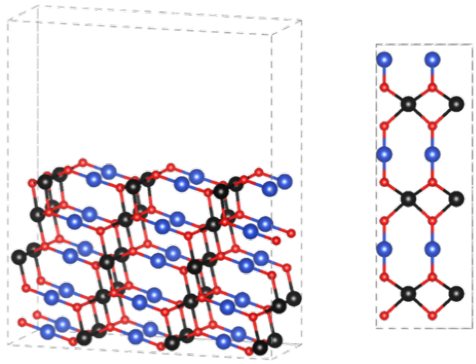

Figure 2.19: Optimized 5-layer slab of pristine (011) orthorhombic surface. Color code: Cu (blue), Fe (black), O (red). On the left lateral view, on the right top view

The computed values of the VBM and CBM are 0.47 V and -1.03 V vs. SHE, respectively. Figure 2.20 depicts the positions of the bands with respect to the redox potential of the reduction of CO_2 to different products after two (CO, formic acid), four (formaldehyde), six (methanol) and eight (methane) proton coupled electron transfer (PCET) steps.

Our computed VB and CB edges (in agreement with those measured through

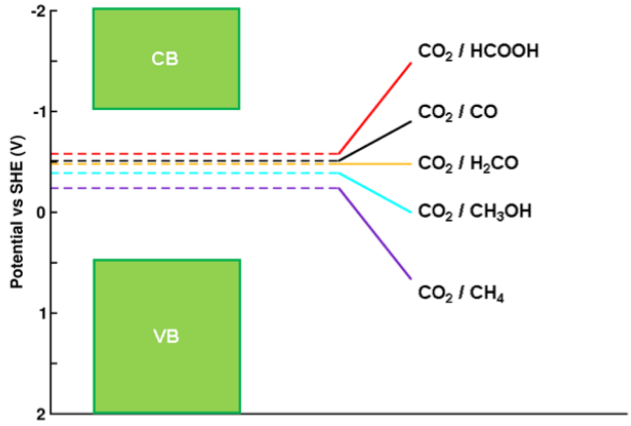

Figure 2.20: Estimates of $CuFeO_2$ band positions, under flat-band conditions, in vacuum. Rectangular green shapes depict the absolute position of the valence (top at 0.47 V) and conduction bands (bottom at 1.03 V) in a scale referred to SHE. Dashed lines represent the reduction potential of CO_2 to some relevant products.

flat band potentials [114, 119]) straddle the redox potential of CO_2 to all the possible products. This indicates that $CuFeO_2$ is in principle photoactive for the CO2RR. The presence of a surface oxygen vacancy affects the position of these bands shifting them down to a lower potential, this might affect the selectivity of the material towards different products. In principle this can also be used to our advantage, engineering the defect concentration in order to tune the selectivity to the desired products.

Surface oxygen vacancies First, we tried to adsorb a CO_2 molecule on the pristine $CuFeO_2$ (011) orthorhombic surface. Of all the possible configurations tested for CO_2 on several adsorption sites (see Supplementary Material for a complete list) none gave a stable adsorbate. In each case, the molecule detached from the surface without any binding interaction. Since previous studies have reported catalytic catalysis on oxides (e.g. Cu_2O and TiO_2) [122, 173], we focused on the interaction of CO_2 with the defective $CuFeO_2$ surface, after considering the concentration of vacancies detected in $CuFeO_2$ [117]. These oxygen vacancies, generate n-type carriers that are driven to the semiconductor-electrolyte interface, and can perform the CO2RR catalysis at the surface [93]. On the surface of the

delafossite, we have two nonequivalent oxygen atoms that can be removed to form the vacancy. One is upward oriented and one is downward oriented (see 1u and 1d in Figure 2.21).

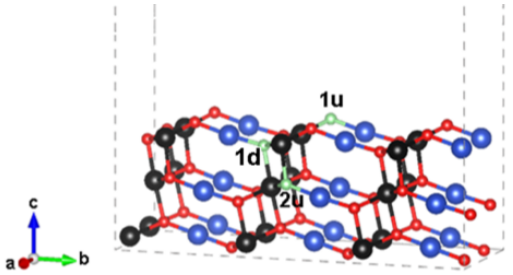

Figure 2.21: Optimized (011) 3-layers surface slab. Oxygens removed to create a single vacancy are highlighted in green. Numbers indicate the layer in which the vacancy is created and the letters "u" and "d" indicate the upward or downward orientation of the oxygen atoms removed, respectively. Colour code: O (red), Cu (blue), Fe (black), O removed to form vacancy (green).

To generate 1u, we remove a tri-coordinated oxygen atom bonded to two unsaturated Fe atoms and a Cu atom. 1d is very similar to 1u, but it has an extra coordination with a Fe atom of the second layer. We have also simulated a 2u vacancy; that is an upwards oriented vacancy in the subsurface layer (Figure 2.21). To investigate the effect of such a doping on the electronic structure and charge distribution, we have computed the Bader charge variations on the superficial atoms. Table 2.14 lists these charge variations and the formation energies of the different vacancies outlined above.

The 2u vacancy is the easiest to form, since the Fe involved have complete coordination prior to the formation the vacancy. It becomes more expensive to remove an oxygen atom from the exposed layer, since the iron atoms are already undercoordinated. In particular, we found that the 1u vacancy is 0.45 eV more favourable than the 1d. For both defects there is just a small surface relaxation and they present a similar pattern of electronic rearrangement upon formation of the vacancy. On the structural side, we can observe that the bond lengths are not modified; the only significant rearrangement is a downward shift of Cu_1 of about 0.63 Å. Due to such displacement, a cavity seems to be opening around the vacancy, making the CO_2 approaching easier. The excess electrons left by the

Table 2.14: Oxygen vacancy formation energies at the PBE+U and HSE06 level of theory and average charge variations on the Fe and Cu atoms directly bondend to the removed oxygen at the PBE+U level. Different vacancy positions are indicated in Figure 2.21 For 2u the first value is for the superficial atom while the highest two are for the subsurface atoms.

	$\Delta E_{def}(eV)$		$\Delta q_{Fe}(e^-)$	$\Delta q_{Cu}(e^-)$
	PBE+U	HSE06		
1u	3.22	3.62	0.42±0.01(×2)	0.14(×1)
1d	3.67	3.98	0.39±0.02(×2)	0.17(×1)
			0.10(×1)	
2u	2.22	2.35	0.35(×1)	0.17(×1)
			0.42±0.02(×2)	

removed oxygen are in each case localized on the neighbouring Fe atoms, that are reduced from Fe (III) to Fe (II). These are both surface atoms in the case of the 1u and 1d vacancies. This result is supported both by the variation on the Bader charges on Table 2.14 and by the variation of magnetic moments from $\mu > 4\mu_B$ typical for Fe (III) to $\mu \sim 3.8\mu_B$, typical of Fe (II) [172]. The charge variation on the Cu atoms is instead very small. The situation on the 2u vacancy is slightly different, since this time there are three neighbouring Fe atoms available to accept the charge (two subsurface and one in the exposed surface). Hence, the degree of localization is reduced, being the charge spread over more atoms, and also contributes to lowering the formation energy of 2u. It is also worth noticing that the two subsurface Fe atoms accept more charge than the surface one, reducing the charge increase on the topmost layer. Looking again at the pDOS in Figure 2.18, we can see that the first unoccupied states are Fe d states that become populated upon doping, consistently with the charge variations just described. The reason why 1u is more stable than 1d can be found in the lower number of M-O bonds to the removed oxygen. To form 1d we need to break 4 M-O bonds, only 3 M-O for 1u. The stability of defective $CuFeO_2$ and the ease of formation of defects is a result of both structural and electronic rearrangements.

In order to develop new strategies to optimize the catalytic performances of $CuFeO_2$, it is essential to explore the role of oxygen vacancies in the activation of

CO_2.

CO_2 adsorption and activation On the two most stable vacancy configurations studied in the previous section (2u and 1u), we tried to adsorb a CO_2 molecule. Calculated adsorption energies at the PBE+U level of theory are 0.87 and -0.33 eV for 2u and 2d, respectively. It is clear that CO_2 requires a superficial vacancy and the consequent electron reorganization in order to adsorb. This charge reorganization is in fact the easiest way to promote an electron flow from the surface of the catalyst to the substrate. In order to be sure that the computed charge accumulation is not dependent on the size of our model, we have simulated vacancy formation also on a bigger slab model, obtaining basically the same results. From now on, our results will refer to the (4x2x3L) slab, which has a defect concentration much closer to the ones usually present in experiments.

We are able to identify two stable configurations of adsorbed carbon dioxide on the (011) surface of the delafossite. We name them B-V_O(I) and B-V_O (II), the first being a radical anion and the second a carbonate-like intermediate. These adsorbates are shown in Figure 2.22 (left panel), with a scheme of the charge accepted by each atom of the adsorbed molecule and donated by the atoms of the surface close to the vacancy upon adsorption.

We account also for the zero-point energy (ZPE) contributions to the adsorption energies and obtain a value of Δ(E+ZPE) = -0.01 and -0.28 eV for B-V_O(I) and B-V_O(II), respectively. The carbonate-like structure is much more stable than the other one. The reason for this can again be found in the structural and electronic rearrangement upon formation of the intermediate. In B-V_O(I), the carbon atom of the molecule is linked to one of the reduced surface iron atoms (d_{C-Fe1}= 2.06Å), one of the oxygen atoms points towards the vacancy and the other one points away from the surface. In this case, activation will occur via electron release from the iron and the copper atom around the vacancy to the carbon atom of CO_2. Basically, the electrophilic part of the adsorbate (*i.e.* the carbon atom) interacts with the electron-rich part of the system, forming the radical anion. The cumulative charge variation on each of the species involved in the processes of vacancy formation and adsorption are listed in Table 2.15

In the case of B-V_O (II), the charge transfer is lower than in the other case,

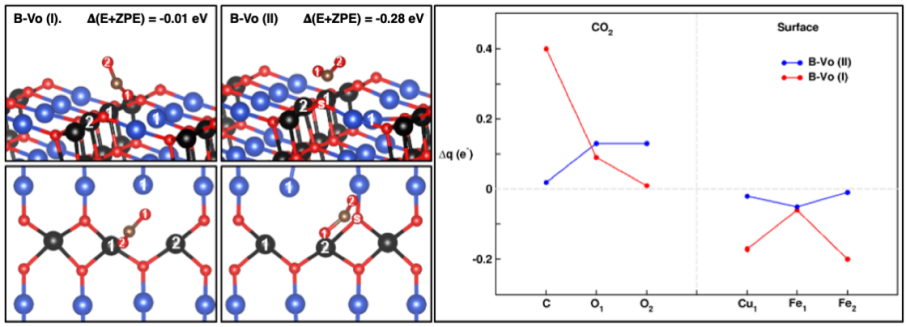

Figure 2.22: Left: Lateral and top views of the two stable geometries B-V_O(I) and B-V_O(II) of CO_2 adsorbed on 1u-type surface oxygen vacancy in a (4x2x3L) slab. Right: Charge variation on the labelled atoms of CO_2 (on the left) and of the surface (on the right). All values have been evaluated in vacuum.

Table 2.15: Details of charge transfer during adsorption process for B-V_O(I) and B-$V_=$(II). The total variation of Bader charges for the surface and the adsorbate are collected in two blocks. Charge variations for the reduced slab (first row) are calculated as difference from the pristine surface to the one with the O vacancy. B-V_O(I)/(II) data (second and third row) are instead obtained as difference between the reduced slab prior to adsorption and the one with the adsorbate. The first three columns of each block report the cumulative Δq for each atom type:$\Delta q_{atype} = \sum_i^{Natype} \Delta q_i$. The fourth column of both blocks is obtained summing the previous three columns. Please note that in the total charge variation of the carbonate species an oxygen from the surface is included in the sum (last entry of the table).

	Surface				Adsorbate			
	Δq_{Cu}	Δq_{Fe}	Δq_O	Δq_{tot}	Δq_O	Δq_C	$\Delta q_{CO_2^{2-}}$	$\Delta q_{CO_3^{2-}}$
$CuFeO_2$	0.12	0.85	-	0.97	-	-	-	-
B-V_O(I)	-0.15	-0.27	-0.07	-0.49	0.10	0.40	0.50	-
B-V_O(II)	-0.06	-0.08	-0.07	- 0.21	0.26	0.02	-	0.25

and the C atom is directly bound to a surface oxygen, forming a carbonate-like species. It easy to understand the different chemical nature and stability of the two intermediates, by looking at the structural modifications that the molecule undergoes. Such structural modification (actually only the main ones) are listed in Table 2.16. We can compare these values with those of similar carbonates (CO_3^{2-}) and carboxylate ($CO_2^{\cdot -}$) intermediates identified on MgO clusters. [174] As in the case of MgO, the carbonate-like structure result to be a more stable intermediate, since the the negative electron effinity of carbon dioxide makes the formation of the radical anion unstable. [175]

Table 2.16: Structural parameters of CO_2 isolated and adsorbed on $CuFeO_2$ slab according to the geometries presented in Figure 2.22 . Values for a carboxyl radical anion and a carbonate adsorbed on MgO from are reported as comparison. Atom labels as in Figure 2.22

	Bond Length(Å)			$\Phi(^{circ})$
	C-O_1	C-O_2	C-O_S	O_1-C-O_2
Isolated CO_2	1.18	1.18	-	180
B-V_O(I)	1.27	1.20	2.60	141
($CO_2^{\cdot -}$-MgO	1.24	1.24	2.29	139
B-V_O(II)	1.30	1.21	1.47	132
(Co_3^{2-})-MgO	1.26	1.26	1.36	131

Our results agree with the proposed mechanism on other materials. As an example, Huygh et al. have proposed carbonate-like structures on reduce anatase $TiO_{2-\delta}$. Moreover, carbonates have been detected by near ambient pressure X-ray photoelectron spectroscopy (NAP-XPS) on the surface of iron-containing (La,Sr)$FeO_{3-\delta}$, so it is not unlikely that they will form on $CuFeO_2$. In the Supplementary material we also report a charge density difference plot of the carbonate-like intermediate, showing increased density on the oxygens involved in this intermediate formation. The lower value of this intermediate can be ascribed to the greater stability of the carbonate with respect to an iron-coordinated radical anion.

Computational Details The usual scheme of running PBE+U calculations for the geometrical optimizations and HSE single points on the minima was used. U-J values were set to 6 eV for Cu d orbitals [147] and to 4 for Fe d orbitals [36]. The kinetic energy cutoff for plane waves was here set to 800 eV and the Brillouin zone was sampled with a Γ centered 8x8x2 k-point mesh. The electronic structure calculations were computed on a 1x$\sqrt{3}$x1 orthorhombic cell built from the hexagonal one.

2.2 Conclusions

We have investigated the interface between three novel push-pull dyes and NiO, characterizing their optical, thermal and electrochemical properties. We have performed a DFT and TD-DFT theoretical analysis, dissecting the properties of the isoleted dyes from those of the dye-semiconductor interface, showing the importance of accounting for the interface in these calculations. The conclusions that can be drawn from molecular properties (vertical excitations, ICT parameters) and interfacial features (hole-injection driving force and charge recombination likelihood) can be summarized in the following points:

i) The optical properties of the dyes show that **C3** has the most effective charge separation (charge withdrawing group), as expected.

ii) The **C1** dye has the largest hole injection driving force. The other two having a similar driving force about 0.20 eV lower than the one for **C1**. The electrochemical characterization of isolated dyes in solution provides a different picture that the interface, with the HOMO energies of the dyes in a very narrow ($\sim$ 0.05 eV) energy window.

iii) The distance between the LUMO of the dyes and the surface of NiO is $\sim$ 10Å, no qualitative differences are observed among the dyes. We can conclude that they all present the same (low) probability for charge recombination between the excited electron and the hole injected in the valence band of the semiconductor.

The three new dyes have been also tested in operating conditions. The cells showed a maximum PCE of $\sim$ 0.05 % for the **C1** dye, the trend being **C1**>**C3**$\sim$**C2**. The obtained conversion efficiencies are in the same order of magnitude of reference push-pull dyes such as the **P1**. It is also worth mentioning that the devices have

shown a remarkable aging resitence, with the PCE measured after 50 days being actually higher than the ones measured right away.

In this chapter we present an analysis of different transition metal oxides for solar energy conversion applications. First, we analyse three members of the family of the delafossites (*i.e.* $CuAlO_2$, $CuGaO_2$ and $CuCrO_2$) as a promising alternative to NiO in p-type DSSCs. We find that the structural and electronic properties in the bulk are similar for Ga and Cr, but slightly different for Al. The eigenvalue gaps for these three oxides are optically forbidden and the computed trend Ga<Cr<Al is consistent with the reference data. We analyze the effect of a Mg doping, finding an enhancement in p-type character. We observe the oxidation of Cu(I) to Cu(II), the latter being responsible for the p-type conductivity. We observe also the presence of copper empty states inside the gap that can explain the loss of efficiency measured at increasing Mg concentrations. These states could cause absorption phenomena, interfering with the dye. The study of the surface properties of the delafossites allowed us to determine the valence band edge positions against NHE. The V_{OC} values determined in this way are much higher that the ones computed for NiO with the same redox couples. The higher V_{OC} and the other promising properties of these oxides mentioned above (light absorption, conductivity etc.) imply that $CuMO_2$ systems can be a better choice than NiO for p-DSSCs.

Among the delafossite systems under study, $CuGaO_2$ is the most promising one thanks to its lower surface energy and defect formation energy. Hence, we selected this out of the three we have studied to investigate the interface with anchoring groups of the dyes and the oxide surface. We have investigated further the role of Mg doping, checking the variation in the absolute band positions at varying concentrations (*i.e.* $\sim 3\%$ and $\sim 6\%$). For these dopant concentrations, the V_{OC} is mostly unchanged, in agreement with experiments. We address the adsorption properties of two of the most commonly used anchoring groups to attach dyes on the surface of the oxides: carboxylic and phosphonic acid. We characterize the interaction between such groups and the surface and evaluate the adsorption energies and investigate the role of the dopant and the solvent on them. Interestingly, there is a strong selectivity towards monodentate binding for both the anchoring groups, contrarily to what happens on NiO. A particular affinity is observed for the Ga sites. This preference for monodentate anchoring should have a positive

effect on the cell efficiency, since it has been shown that when protic groups release H to the surface the driving forces for hole injection are lowered. Hence, our calculations show that -COOH and -PO_3H_2 should perform better on $CuGaO_2$ than on NiO. We also show that Mg doping increases the affinity of the delafossite surface for both anchoring groups. Such effect is counterbalanced by that of the acetonitrile solvent.

The idea of reducing CO_2 concentration and at the same time convert it into new fuels using environment-friendly strategies represents a current grand challenge in chemistry, engineering and other scientific research fields. The pioneering materials for CO2RR (based on metallic copper) suffer from high instability, so the identification of new highly performant catalysts is needed. Within this framework, recent works have proposed the $CuFeO_2$ delafossite as promising photo-electrocatalyst thanks to its peculiar properties: high mobility charge carrier, low band gap and photo-electrochemical stability. These qualities need to be supported by a catalytic activity. Recently, $CuFeO_2$ has been tested as CO2RR photocatalyst and recent computational works have relegated its role to the photo-activation, with no active roles in catalysis. Here we have demonstrated that adsorption and activation of CO_2 can be achieved by tuning the $CuFeO_2$ surface properties: the reduction by formation of surface oxygen vacancies provides the electronic structure features (i.e. charge localization) that is needed for CO_2 activation. We have shown that this kind of defect determines an electronic charge augmentation on Fe involving two different valences, *i.e.* Fe(III) and Fe(II). In other words, the reduction process that involves surface Fe atoms is the intermediate step required to draw charges to CO_2, thus overcoming the issues due to its chemical inertia and leading to its adsorption on the $CuFeO_2$ surface slab. Two different species can be formed after CO_2 adsorption: a carboxylate radical anion and a carbonate-like intermediate. In the first case both Cu and Fe play an important role into the charge transfer to the adsorbate while for the latter there is a smaller electronic transfer highly delocalized since no atom in CO_2 strongly changes its charge distribution. The formation of carbonate-like units is more likely as already suggested for other materials (e.g., MgO, TiO_2), even though the formation of the highly reactive radical anion is still a downhill process. In con-

clusion, we have proven that $CuFeO_2$ can be an active photocatalyst for CO2RR, but only when oxygen vacancies are present. For the first time, here we have demonstrated that it is not only the Cu to play an important role, but we have identified the Fe reduction as the key process for an effective CO_2 adsorption on $CuFeO_{2-\delta}$. Our results also provide a global picture of surface and CO_2 activation, as first key step for a complex chemical process that lead from CO_2 to chemicals (e.g., HCOOH, CO, CH_3OH). Our model is of course far from the complexity of a photo-electrochemical cells at operating conditions: other players are crucial for a proper CO2RR catalysis, the solvent, the cations at the surface, the pH, just to name a few. Here, we have set the scientific basis to understand the $CuFeO_2$ properties, anticipating the potential positive effects of oxygen vacancies for activating and guiding the subsequent CO2RR process. Thus, as design indications, we can suggest to focus on $CuFeO_2$ enhancing the formation of surface oxygen defects by surface reduction, aliovalent doping or by electrochemical strategies. Further studies are undergoing in our laboratory to address the several possible CO_2 reduction mechanisms and pathways, also considering the effects of the other active species along the CO2RR at the electrode surface.

Chapter 3

Effective Methods for Hybrid Materials

Heterogeneous functional materials are challenging systems even for state of the art computational techniques. We usually rely on DFT to investigate their properties in order to be able to afford model systems that are big enough to be meaningful. However, the peculiar electronic structure properties of such materials often push DFT to its limits. Some corrections must be applied in order to make DFT approaches suitable for complex interfaces. In many cases we rely on well established schemes to amend for DFT deficiencies, but sometimes it is mandatory to develop new approaches. In this Chapter, we report two case studies of methodological development. In Section 3.1 we report the development and implementation of DFET and its application on a model system. In Section 3.2 we report a reparametrization of the DFT-D2 dispersion scheme to make it suitable for metal-molecule interfaces.

3.1 Density Functional Embedding Theory

As we have discussed in Chapter 1, the theoretical investigation of hybrid functional materials presents many challenges. Sometimes the need for high level CW methods that are able to catch excited states properties and give better accuracies clashes with the need to model extended systems with a great number of atoms.

In these situations embedding methods can help solve the problem by partitioning the system in subsets that can be treated with different levels of theory. The way the interaction between the subsets is accounted for varies from method to method. In Chapter 1 we have already given a brief review of some of the most important ones. In this section, we report the formalism of Density Functional Embedding Theory (DFET) and its implementation in the VASP program carried out by Kuang *et al.* [176], along with some applications and issues that we encountered in applying the method. The core of DFET is a density-based partition of the system in two sub-densities, one of the environment and one of the cluster. A unique interaction (embedding) potential accounts for the interaction between the two subsets. Such potential is optimized through an OEP procedure carried out self-consistently updating the DFT densities of the cluster and environment under the effect of the potential. In a final step a calculation on the cluster (in presence of the optimized potential) is carried out with the desired level of theory. Finally, the total energy is obtained with the simple ONIOM-like formula:

$$E_{tot} = E_{tot}^{DFT} + (E_{emb,cluster}^{CW} - E_{emb,cluster}^{DFT}) \tag{3.1}$$

In the following sections we go into the details of the DFET formalism.

3.1.1 Embedding Formalism

The current implementation of the embedding code on VASP allows for the optimization of an embedding potential, given a reference density and a partition in two subsets of this density.

The formalism proposed by Huang et al. [177] starts with the usual partition of the system into two subsets: a cluster and an environment. The sum of the electron densities of the two subsets being equal to the total density.

$$n_{tot} = n_{clu} + n_{env} \tag{3.2}$$

Hence the expression for the total energy is

$$E_{tot}[n_{tot}] = E_{clu}[n_{clu}] + E_{env}[n_{env}] + E_{int}[n_{clu}, n_{env}] \tag{3.3}$$

Embedding potentials for the cluster, due to the presence of the environment, and viceversa can be defined as:

$$V_{emb}^{clu} = \frac{\partial E_{int}[n_{clu}, n_{env}]}{\partial n_{clu}} \quad ; \quad V_{emb}^{env} = \frac{\partial E_{int}[n_{clu}, n_{env}]}{\partial n_{env}} \tag{3.4}$$

Therefore it is dependent on the system partitioning. However, given a choice of subsets and fixed the number of electrons in the cluster and in the environment, we can set $V_{emb}^{clu} = V_{emb}^{env}$. The proof of uniqueness of the embedding potentials follows that of the first Hohenberg and Kohn theorem.

Proof of uniqueness of the embedding potential

Let us suppose to have two different embedding potentials V_1 and V_2 which give rise to the two density partitioning n_{A1}, n_{B1} and n_{A2}, n_{B2}. For both we can write

$$n_{tot} = n_{A1} + n_{B1} \quad n_{tot} = n_{A2} + n_{B2} \tag{3.5}$$

Fixed the number of electrons and assuming that A and B are nondegenerate, we can write:

$$\begin{aligned} E_A[n_{A1}] + \int V_1 n_{A1} dr^3 < E_A[n_{A2}] + \int V_1 n_{A2} dr^3 \\ E_B[n_{B1}] + \int V_1 n_{B1} dr^3 < E_B[n_{B2}] + \int V_1 n_{B2} dr^3 \end{aligned} \tag{3.6}$$

which can be rearranged as:

$$\begin{aligned} E_A[n_{A1}] < E_A[n_{A2}] + \int V_1 (n_{A2} - n_{A1}) dr^3 \\ E_B[n_{B1}] < E_B[n_{B2}] + \int V_1 (n_{B2} - n_{B1}) dr^3 \end{aligned} \tag{3.7}$$

By using 3.5 we can see that the integral terms in 3.7 are equal and opposite in sign. Hence, summing the disequalities we obtain:

$$E_A[n_{A1}] + E_B[n_{B1}] < E_A[n_{A2}] + E_B[n_{B2}] \tag{3.8}$$

Exchanging the arbitrary 1 and 2 indices we can obtain the contradictory result:

$$E_A[n_{A2}] + E_B[n_{B2}] < E_A[n_{A1}] + E_B[n_{B1}] \tag{3.9}$$

Which proves that the embedding potential (if exists) is unique

Derivation of the embedding potential

To obtain the embedding potential the first thing we need is a reference density n_{ref}. This is obtained from a KS-DFT calculation on the entire system. Then we look for an embedding potential that satisfies the constraint $n_{ref} = n_A + n_B$ This is done with a modified optimized effective potential (OEP) method [178], using a modified Wu-Yang potential:

$$W[V_{emb}, n_K[V_{emb}]] = \sum_{K=A,B} E_K[n_K] + \int V_{emb} \left(\sum_K n_K - n_{ref} \right) dr^3 \tag{3.10}$$

V_{emb} is introduced as a Lagrange multiplier to enforce the constraint on the maximization. Please note that the electron densities are in turn functionals of the embedding potential. With this in mind, we can calculate the total gradient of W w.r.t. V_{emb} as: [1]

$$\begin{aligned} \frac{\delta W[V_{emb}, n_K[V_{emb}]]}{\delta V_{emb}} = & \left. \frac{\delta W[V_{emb}, n_K]}{\delta V_{emb}} \right|_{n_K = const.} \\ & + \int \frac{\delta W[V_{emb}, n_K[V_{emb}]]}{\delta n_K(\boldsymbol{r'})} \frac{\delta n_K(r')}{\delta V_{emb}(r)} dr'^3 \end{aligned} \tag{3.11}$$

where the second term on the right is a chain rule for functional derivatives. By inserting 3.10 into the first right end term of 3.11 we obtain:

$$\sum_K \frac{\delta E_K[n_K]}{\delta V_{emb}} + \int \frac{\delta V_{emb}(\boldsymbol{r})}{\delta V_{emb}(\boldsymbol{r'})} \left(\sum_{K=A,B} n_K - n_{ref} \right) d\boldsymbol{r}^{\boldsymbol{3}} \tag{3.12}$$

[1] just as the total gradient of a function $f(x, y(x))$ is given by $\frac{\delta f}{\delta x} = \frac{\partial f}{\partial x} + \frac{\partial f}{\partial y} \frac{\partial y}{\partial x}$

here the first term vanishes because there is no explicit dependence of E_K on V_{emb}, while the second one becomes: $n_A + n_B - n_{ref}$ [2]. Let us now deal with the second right end term of 3.11, again we start by plugging in the expression for W given by 3.10:

$$\int \frac{\delta}{\delta n_K(\boldsymbol{r'})} \left[\sum_{K=A,B} E_K[n_K] + \int V_{emb} \left(\sum_{K=A,B} n_K - n_{ref} \right) d\boldsymbol{r}^3 \right] \frac{\delta n_K(\boldsymbol{r'})}{\delta V_{emb}(\boldsymbol{r})} d\boldsymbol{r'}^3 \tag{3.13}$$

Now we can chose the $n_K s$ to be the ground state densities of W, namely the term in brackets in 3.13. If this is the case, the derivative of this term w.r.t. to n_K is a constant. [3] Now we can rewrite 3.11 using the expressions in 3.12 and 3.13 and writing a constant μ_K in place of the derivative of the term in brackets in 3.13.

$$\frac{\delta W[V_{emb}, n_K[V_{emb}]]}{\delta V_{emb}} = \sum_{K=A,B} \int \mu_K \frac{\delta n_K(\boldsymbol{r'})}{\delta V_{emb}(\boldsymbol{r})} d\boldsymbol{r'}^3 + n_A + n_B - n_{ref} \tag{3.14}$$

We can take the derivative w.r.t. $V_{emb}(\boldsymbol{r})$ out of the integration which is in $d\boldsymbol{r'}^3$

$$\frac{\delta W[V_{emb}, n_K[V_{emb}]]}{\delta V_{emb}} = \sum_{K=A,B} \mu_K \frac{\delta}{\delta V_{emb}(\boldsymbol{r})} \int n_K(\boldsymbol{r'}) d\boldsymbol{r'}^3 + n_A + n_B - n_{ref} \tag{3.15}$$

The electron densities integrate to an electron number and the first term on the right vanishes because it is a derivative of a constant. Hence we are left with

$$\frac{\delta W}{\delta V_{emb}} = n_A + n_B - n_{ref} \tag{3.16}$$

which in its stationary point statisfies the condition $n_A + n_B = n_{ref}$. Via the evaluation of the second gradient of W it can be shown that the functional is globally concave. Hence the search for the embedding potential is a maximization problem.

This formalism has been implemented in a modified version of ABINIT by

[2] This is easily showed recalling this property of functional derivatives: $\frac{\delta F[x]}{\delta F[x']} = \delta(x - x')$ this is somehow a generalization for functional differentiation of the property dx/dx = 1

[3] In analogy with the fact that $\frac{\delta E[\rho(\boldsymbol{r})]}{\delta \rho(\boldsymbol{r})} = const.$ if $\rho(\boldsymbol{r})$ is the ground state density and $E[\rho(\boldsymbol{r})]$ the ground state energy

Huang *et al.* [177] without any modification. In the following section we present a more challenging implementation in VASP within the PAW formalism.

VASP implementation

The projector augmented wave (PAW) method used in codes as VASP to treat the interaction between core and valence states presents a challenge to the implementation of the DFET [176]. In Blöchl treatment, the exact all-electron (AE) wavefunction of the n-th band is expanded as:

$$|\Psi_n\rangle = |\tilde{\Psi}\rangle + \sum_i (|\phi_i\rangle - |\tilde{\phi}_i\rangle) \langle \tilde{p_i}|\tilde{\Psi}_n\rangle \tag{3.17}$$

Where $|\tilde{\Psi}\rangle$ are soft, nodeless pseudowavefunctions, $|\tilde{\phi}_i\rangle$ and $|\phi_i\rangle$ are on-site basis set functions and $\tilde{p_i}$ are the projector functions, which are orthonormal to the PS basis. Outside the augmentation sphere $|\tilde{\phi}_i\rangle = |\phi_i\rangle$ and $|\tilde{\Psi}\rangle = |\Psi\rangle$. Usually the *frozen core approximation* is used; meaning that the AE wavefunctions in the core are fixed during the SCF. This represents the main difference between the PAW approach and norm-conserving PPs: here the AE wavefunctions are explicitly represented and expanded as in 3.17. PAW is a frozen-core, all electron level of theory. From 3.17 follows a decomposition of the total density as:

$$n = \tilde{n} + n^1 - \tilde{n}^1 \tag{3.18}$$

In the following rearrangement of the total Hamiltonian[4]

$$H = -\frac{1}{2}\nabla^2 + \tilde{v}_{eff} + \sum_{i,j} |\tilde{p_i}\rangle \, (\hat{D_{ij}} + D^1_{ij} - \tilde{D}^1_{ij}) \, \langle \tilde{p_j}| \tag{3.19}$$

with

[4]See reference for derivation

$$\begin{aligned}\hat{D}_{ij} &= \sum_L \int d\boldsymbol{r}\tilde{v}_{eff}(\boldsymbol{r})\hat{Q}_{ij}^L(\boldsymbol{r}) \\ D_{ij}^1 &= \langle\phi_i| -\frac{1}{2}\nabla^2 + v_{eff}^1 |\phi_j\rangle \\ \tilde{D}_{ij}^1 &= \langle\phi_i| -\frac{1}{2}\nabla^2 + \tilde{v}_{eff}^1 |\phi_j\rangle + \sum_L \int_\Omega d\boldsymbol{r}\tilde{v}_{eff}^1(\boldsymbol{r})\hat{Q}_{ij}^L(\boldsymbol{r})\end{aligned} \tag{3.20}$$

where $\hat{Q}_{ij}^L(\boldsymbol{r})$ are the angular decomposed components of the compensation charge $\hat{n}$. We can see that the effective potential (containing the Hartree and exchange-correlation terms) appears in three different forms that resemble the partition of the density. The embedding potential enters all these three terms. This is straightforward for the first term that is evaluated on the same uniform grid as V_{emb}. For the other two terms instead, we will need to project the embedding potential on the finer radial grid on which the other two terms are evaluated. The projection used is the following:

$$V_{emb}(\boldsymbol{r}) = \sum_{LM} V_{emb}^{LM}(\boldsymbol{r})S_{LM}(\hat{\boldsymbol{r}}) \tag{3.21}$$

There are two different algorithms to perform this projection (see reference [176] for details). The total KS energy in the PAW formalism can be written as:

$$E = \sum_n f_n \langle\tilde{\Psi}_n| H |\tilde{\Psi}_n\rangle + \tilde{E}_{dc} + E_{dc}^1 - \tilde{E}_{dc}^1 + U(\boldsymbol{R}_I) \tag{3.22}$$

where the terms with the subscipt dc are double counting corrections. Let us now evaluate the derivative of the energy with respect to the embedding potential:

$$\frac{\delta E}{\delta V_{emb}} = \left.\frac{\delta E}{\delta V_{emb}}\right|_{n(r)} = \sum_n f_n \langle\tilde{\Psi}_n| \frac{\delta H}{\delta V_{emb}} |\tilde{\Psi}_n\rangle \tag{3.23}$$

double counting terms and nuclear potential vanish since they are independent of V_{emb}. Deriving the PAW Hamiltonian w.r.t. the embedding potential yields:

$$\frac{\delta H}{\delta V_{emb}} = \delta(\boldsymbol{r} - \boldsymbol{r'}) + \sum_{ij} |\tilde{p}_i\rangle \langle\tilde{p}_j| \left(\frac{\delta \hat{D}_{ij}}{\delta V_{emb}} + \frac{\delta D^1_{ij}}{\delta V_{emb}} - \frac{\tilde{D}^1_{ij}}{\delta V_{emb}} \right) \tag{3.24}$$

Differentiation of $\hat{D}_{ij}$ is straightforward:

$$\begin{aligned} \frac{\delta \hat{D}_{ij}}{\delta V_{emb}} &= \frac{\delta}{\delta V_{emb}} \sum_L \int (v_H + v_{XC} + V_{emb}) \hat{Q}^L_{ij} d\boldsymbol{r} \\ &= \sum_L \hat{Q}^L_{ij} \end{aligned} \tag{3.25}$$

where we have used the explicit expression for $\tilde{v}_{eff}$. Now we can rewrite 3.24 as:

$$\frac{\delta H}{\delta V_{emb}} = \delta(\boldsymbol{r} - \boldsymbol{r'}) + \sum_{ij} |\tilde{p}_i\rangle \langle\tilde{p}_j| \left(\hat{Q}^L_{ij} + \frac{\delta D^1_{ij}}{\delta V_{emb}} - \frac{\tilde{D}^1_{ij}}{\delta V_{emb}} \right) \tag{3.26}$$

and plug it in 3.23 to get:

$$\frac{\delta E}{\delta V_{emb}} = \tilde{n} + \overbrace{\sum_{ij,L} \rho_{ij} \hat{Q}^L_{ij}}^{\hat{n}} + \sum_{ij} \rho_{ij} \left(\frac{\delta D^1_{ij}}{\delta V_{emb}} - \frac{\tilde{D}^1_{ij}}{\delta V_{emb}} \right) \tag{3.27}$$

here we have used the relation

$$\rho_{ij} = \sum_n f_n \langle\tilde{\Psi}_n|\tilde{p}_i\rangle \langle\tilde{p}_j|\tilde{\Psi}_n\rangle$$

The evaluation of the last term on the right is quite complex, the evaluation of the integral in radial coordinates gives back:

$$\frac{\delta(D^1_{ij} - \tilde{D}^1_{ij})}{\delta V_{emb}} = \sum_{LM} C^{LM}_{lml'm'} \int dr (Q_{lml'm'}(r) - Q^L_{lml'm'}) \frac{\delta V^{LM}_{emb}}{\delta V_{emb}} \tag{3.28}$$

A torough explanation of all the terms in this equation is beyond our purpose.

We wish to put our focus on the term $\frac{\delta V_{emb}^{LM}}{\delta V_{emb}}$. This should give us a delta function but in practice this is not the case. This arises from the fact that the radial grid is much finer than the uniform one and the projection algorithm needs to interpolate. Hence, a variation of the potential at one point on the uniform grid induces a variation at more than one point on the radial grid. This means that the derivative of the energy of a subset in presence of the embedding potential w.r.t. the embedding potential is no longer equal to the electron density of that subset. In other words, the expression of the Wu-Yang functional in 3.10 must be changed because the equation 3.16 no longer holds. The change in energy is no longer given by the value of the density, so the problem is solved substituting the electron densities in 3.10 with the explicit energy derivatives

$$W[V_{emb}, n_K[V_{emb}]] = \sum_{K=A,B} E_K[n_K] - \int V_{emb}(\boldsymbol{r}) \frac{\delta E_{ref}}{\delta V(\boldsymbol{r})} d\boldsymbol{r} \tag{3.29}$$

And the gradient becomes

$$\frac{\delta W}{\delta V_{emb}} = \frac{\delta E_A}{\delta V(\boldsymbol{r})} + \frac{\delta E_B}{\delta V(\boldsymbol{r})} - \frac{\delta E_{ref}}{\delta V(\boldsymbol{r})} \tag{3.30}$$

The constraint is now on the energy derivative and not anymore on the densities, which is in principle the same.

3.1.2 DFET Application

We have applied the embedding scheme described in the previous chapter to a coumarine based dye (C343) adsorbed on a p-type NiO (100) surface. The surface of the semiconductor has been modelled with a 5-Layer slab of a 2x2x1 supercell and an antiferromagnetic ordering on Ni atoms. Only the two uppermost layers were left free to relax in the geometry optimization and a neutral Nickel atom was removed from the center of the three bottommost layers, which has the effect of introducing two holes in the system to account for the p-type character of the semiconductor. This is consistent with a previous study on the same system [125].

First, we ran a DFT+U calculation (with a U-J=3.8 on Ni) on the whole system to obtain the reference ground state electron density n_{ref}. Then we proceeded

with partitioning the system in a cluster (*i.e.* the C343 molecule) and an environment (the NiO slab). The embedding potential was obtained maximizing the W potential by self-consistently updating the embedding potential and the energy derivatives (see 3.16). A penalty function of $\lambda = 10^{-4}$ was used to damp the oscillations on the potential. The embedding potential is depicted in Figure 3.1. As expected, the greatest part of the potential is localized in the boundary region between the cluster and the environment. Some small oscillations are present in the vacuum regions. These are just numerical noise and could easily be damped by increasing λ. This would however cancel out also part of the physical oscillations. Furthermore, oscillations far from the atoms have no effect on the densities of the systems and so they are not an error source.

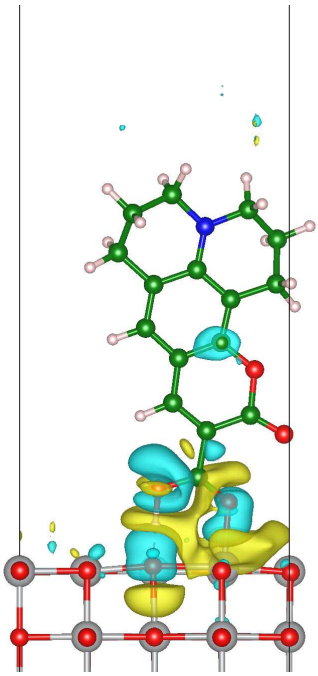

Figure 3.1: Embedding potential for C343 (cluster) on NiO (100) (environment). Only the two uppermost layers are displayed. Colour code: C (green); N (blue); O (red); Ni (grey); H (light pink). Blue areas represent a negative potential value while yellow areas a positive one. Isosurface level: 1×10^{-5} arb. units

Figure 3.2 depicts the atom- angular momentum- projected Densities of States

for the reference calculation and the subsequent partition in cluster and environment. Please note that each of the plots depicted in figure are shifted in energy with respect to the Fermi level obtained from the respective calculation. Hence, no information about the energy level alignment can be obtained by comparing the plots. By comparing the plots we can practically see how the DOS of the DFT-in-DFT calculation are very similar to the one from DFT on the entire system. The differences might be due to hybridization between molecular and NiO states in the bonding region that are not allowed anymore in the separate calculations.

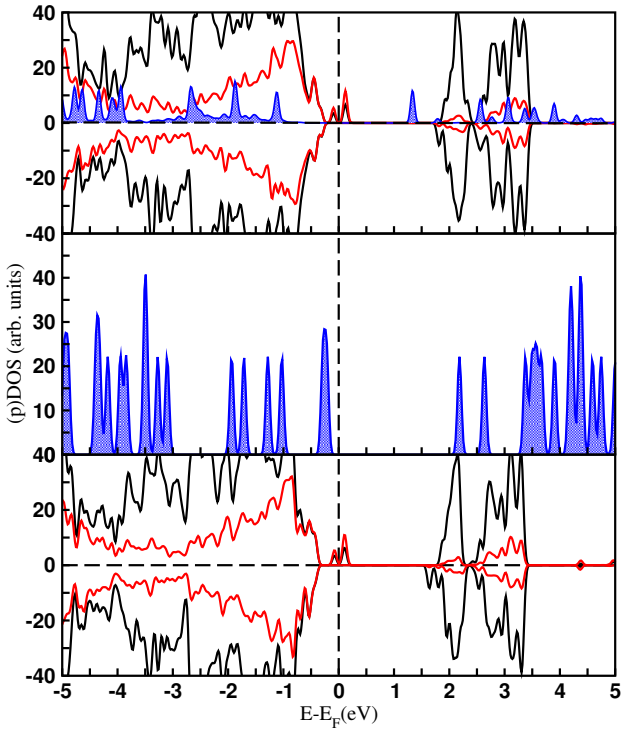

Figure 3.2: atom- angular-momentum- projected density of states of the reference calculation (top), cluster (middle) and environment (bottom). Color code: Ni (black) O (red) C343 (blue). Opposite sign values represent the alpha and beta spin channels. In the total DOS of the cluster alone the two spin components have been summed since they are totally symmetric. Each DOS is shifted with respect to its own Fermi level.

As expected, the NiO band gap is way too low with respect to the experimental

one due to the poor correction for self interaction error in PBE+U. Similarly, the HOMO-LUMO gap of the molecule is almost 1 eV lower than the experimentally measured optical gap. What we can do now is take the embedding potential optimized in this first DFT-in-DFT step and perform an embedded calculation on the cluster alone with a higher level of theory.

We tested this with a Hybrid DFT in DFT calculation, using the HSE06 functional on the embedded cluster. In Figure 3.3 we report the embedded HSE calculation on the molecule (top panel) in comparison with a calculation on the isolated molecule (bottom panel) with the same functional. In the second case there is no embedding potential, but the geometry is still the adsorption geometry. We can observe how the hybrid functional opens the gap up to 3.35 eV. Experimental adsorption spectra on NiO sensitized with C343 report peaks around 420 nm, corresponding to ca. 2.9 eV energy difference [179]. This peaks are due to the molecule since they do not appear on pristine NiO.

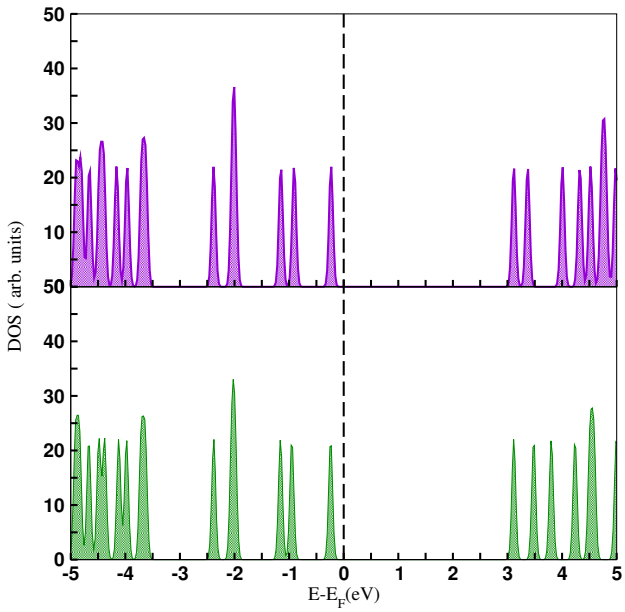

Figure 3.3: Density of states of C343 obtained with the hybrid HSE functional on the embedded cluster (top) and on the isolated molecule at the adsorption geometry (bottom). The spin channels are summed

No major difference in the HOMO-LUMO gap is observed with and without

including the embedding potential. Also comparison of the charge distribution on the atoms and on the shape of the LUMO show no difference in the two cases. For comparison we calculated also the whole system at the HSE level. Still, the HOMO-LUMO gap of the molecule has the same value. The states around the Fermi level of NiO appear to be more strongly localized.

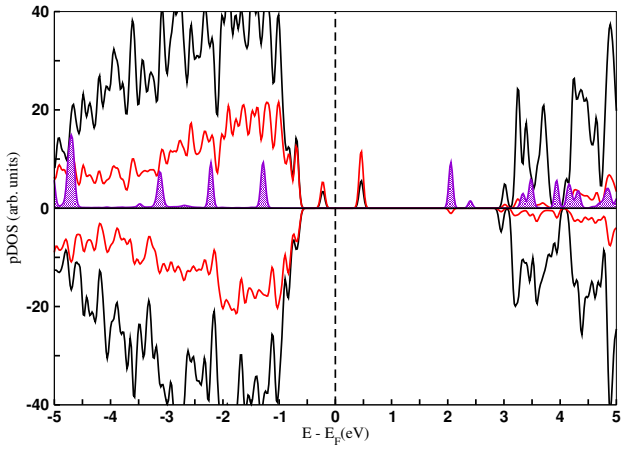

Figure 3.4: Atom- angular-momentum- Projected Density of States of the whole systems at the HSE level.

We might be missing some important contribution. In the next section, we try to improve our results including the contribution of the solvent.

Implicit Solvent

We included the effect of a solvent in the embedding potential optimization. This was done by implicitly accounting for the solvent in the reference calculation with the polarizable continuum model (PCM) implemented in VASP [180]. The solvent implied was acetonitrile, a typical solvent in p-DSSCs testing and fabrication. In the V_{emb}^{sol} optimization the densities of cluster and environment calculated in vacuum where matched to the solvated reference:

$$n_{ref}^{ACN} = n_A + n_B \tag{3.31}$$

or, consistently with the VASP implementation

$$\frac{\partial E_{ref}^{ACN}}{\partial V} = \frac{\partial E_A}{\partial V} + \frac{\partial E_A}{\partial V} \tag{3.32}$$

The so obtained potential is shown in Figure 3.5

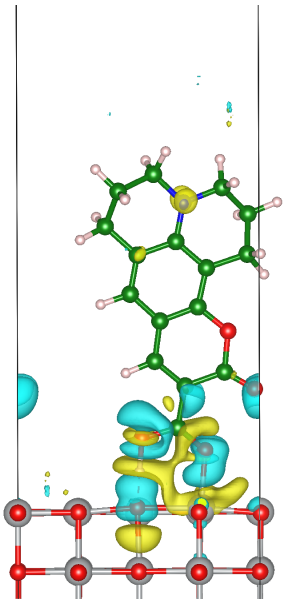

Figure 3.5: Embedding potential in acetonitrile obtained by matching the vacuum calculations in the two subsets to a solvated reference, as described in text. Color code: see figure 3.1. Isosurface level 1×10^{-5}

As in the previous section, V_{emb} was optimized at a PBE+U level of theory and then read in to perform HSE calculations on the cluster. Comparing the DOS on the embedded cluster with the isolated molecule in the solvent we can now see a shift in the HOMO-LUMO gap. The embedding potential should now account for solvation in presence of the surface, while in the isolated case the solvent is all around the molecule as if it were in solution.

Figure 3.6 shows the blue shift obtained upon adsorption of the solvated molecule due to the different solvation (the geometry is the same in the two cases). It looks like acetonitrile has a stabilization effect on the LUMO, which gets stronger when the molecule is completely solvated. This is qualitatively consistent with the

measurements by Morandeira et al. [80] that were carried out in the same solvent. Figure 3.7 depicts their original measurement, in the inset the dotted and the solid line correspond to the isolated and adsorbed molecule, respectively.

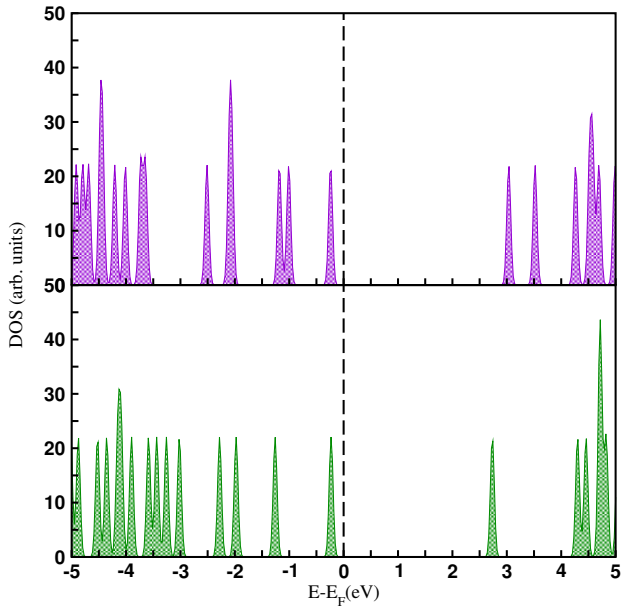

Figure 3.6: Density of state of C343 obtained with the HSE hybrid functional on the molecule in presence of V_{emb}^{sol} (top) and of the isolated molecule in an implicit model for acetonitrile (bottom).

Table 3.1: HOMO-LUMO gap values from adsorption experiments (converted from λ_{max}) and from our calculations. The last column on the right shows the extent of the blue-shift upon adsorption of C343 on NiO in acetonitrile solvent.

	$\Delta E_{solution}$(eV)	ΔE_{onNiO} (eV)	$\Delta\Delta E$ (eV)
Exp [80]	2.77	2.93	0.16
Theo	2.96	3.28	0.31

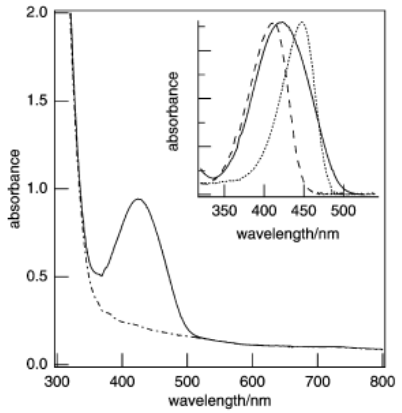

Figure 2. Steady-state absorption spectra of C343|NiO (solid line) and NiO (dash−dot line). Inset: Steady-state absorption spectra of C343|NiO (solid line, NiO absorption has been subtracted), C343H (dotted line, the solvent is MeCN), and $C343^-$ (dashed line, the solvent is EtOH saturated with Na_2CO_3).

Figure 3.7: Original absorption measurements by Morandeira et al. [80]

3.1.3 Unsolved Issues in DFET implementation

If we have a closer look to the embedded monodentate C343/NiO system in acetornitrile, we actually find an unphysical shift in the HOMO-LUMO gap between the DFT calculation and the DFT in DFT system. Figure 3.8 depicts the density of states of the two systems.

We ran several test to try to understand the reason for this discrepancy. We have tried lowering the penalty λ, and changing the F_{corr} to obtain more accurate derivatives, but we could not remove the shift. We have also tried to improve the convergence on the electron densities of the cluster and environment during the OEP procedure, going as low as 10^{-12} but this did not change the behaviour of the system. By having a closer look at the values of the W functional during the OEP functionals, this looks like a systematic convergence problem; probably due to some issue in the implementation of the code or in the energy derivative formalism. Future studies will focus on fixing these problems, trying to improve the stability of the VASP implementation making it suitable to molecule-oxide interfaces in solution.

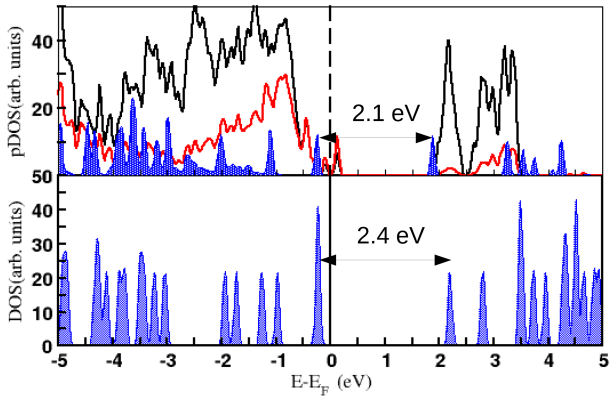

Figure 3.8: Reference calculation for monodentate C343 (top) cluster PBEinPBE obtained from the V_{emb} convergence (bottom).

3.2 Dispersion corrected-DFT for hybrid systems

We have already spent a few words in Chapter 1 on the flaws of density functional theory, and in particular on the lack of dispersion interactions in it. When it comes to hybrid systems, such as molecules on metal surfaces, this inadequacy needs to be overcome in order to get reliable results. In these kinds of systems in fact van der Waals forces play a pivotal role, as shown for example by the work of Zaremba and Kohn many years ago [181]. One way to be able to catch these interactions would be to switch from DFT to higher levels of theory employing coupled clusters and many body perturbation theory (MBPT) techniques [182]. However, their high computational cost would force us to use model systems that are too small to be of any significance in predicting the behaviour of extended systems. On the other hand, a dispersion-correction included in DFT would allow us to keep its cost-effectiveness and to catch the missing interactions. Several methods have been proposed to do that and have been applied to van der Waals complexes [183] and soft materials [184]. The most popular among these methods are certainly the DFT-D family developed by Grimme and co-workers (e.g. DFT-D2, DFT-D3) [20, 21]. The reason for the success of these methods is their computational efficiency and their availability in most DFT codes.

We retuned the DFT-D2 parameter for silver by studying the adsorption of four

small aromatic molecules on its low energy surface *i.e.* Ag(111). The optimized molecules and the cluster model are depicted in Figure 3.9

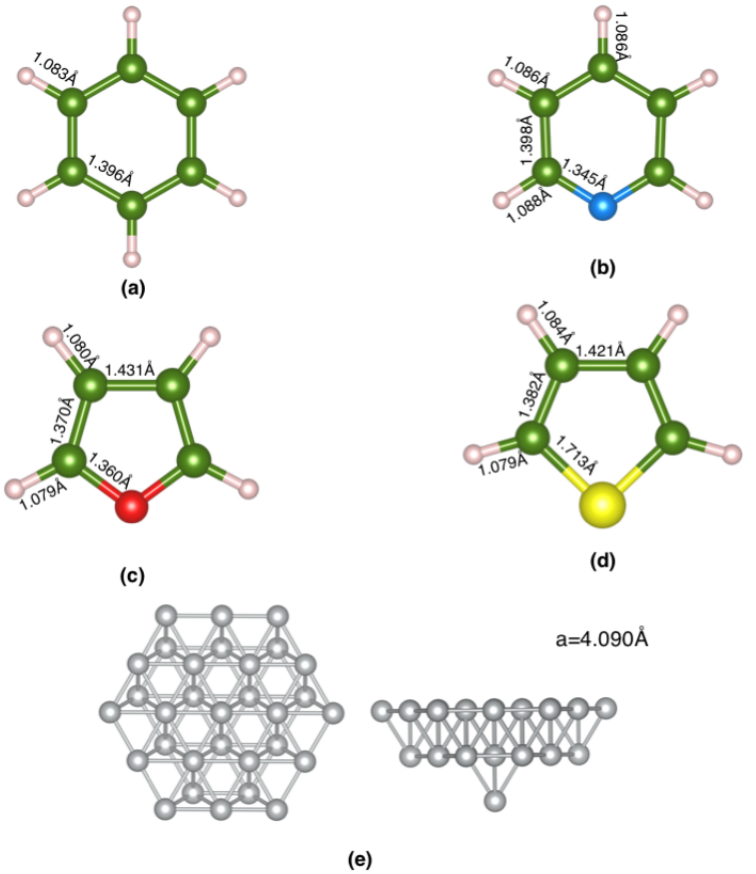

Figure 3.9: Strucure and bond lengths of (a) benzene, (b) pyridine, (c) furan and (d) thiophene; (e) top (left) and lateral (right) view of the Ag_{32} cluster built from the Ag fcc bulck strucurre (a_0 = 4.090 Å) and representative of the Ag(111) surface.

In Chapter 1 we have briefly outlined the possible reasons for the inaccuracy of DFT-D techniques in describing metal-molecule interfaces. Mainly, it was ascribed to the use of approximate C_6 parameters for the TM atoms. The latter were in fact taken as an average value between the preceding group VIII and the following group III element, since the approach used to compute the parameters does not

really make sense for TMs [25]. In Chapter 1, we have also pointed out the importance of shutting down the dispersive contribution "at the right moment" via the damping function. The latter, in the standard DFT-D2 formulation has the simple form:

$$f_{dmp} = \frac{1}{1 + e^{d(R_{ij}/R_{vdW} - 1)}} \tag{3.33}$$

depending on the van der Waals radii of the atoms R_{vdW} (besides its obvious dependence on the interatomic distances R_{ij})

We tested the different C_6 and R_{vdW} parameters for the various molecules adsorbed on the cluster, using MP2 data as a benchmark. We computed adsorption energies and minimum energy distances and evaluated the Mean Absolute Percentage Errors (MAPE) with respect to the MP2 data. Lowering the C_6 parameter, albeit lowering the adsorption energies, does not affect the position of the minima (*i.e.* equilibrium distances are not altered and are in each case lower that the MP2 ones). By increasing R_{vdW} we were able to obtain both the effects of lowering the adsorption strengths and increasing the equilibrium distances. While C_6 only affects the adsorption strengths, the other parameter affects the damping function that shuts down the dispersion contribution at short ranges. By increasing R_{vdW} we are turning off the dispersion contribution when the atoms are further apart with respect to the standard parametrization, accounting in a way for the screening effect of the metal on the incoming dipole. The best choice of parameters has been to use the standard C_6 and a R_{vdW} increased by 65%. Figure 3.10 depicts the adsorption scans and the MAPE comparing the different DFT-D corrections against MP2.

Here we have reported a viable strategy to tune the DFT-D2 parameters for metals in order to achieve a qualitatively reliable description of metal-molecule interaction. We used MP2 cluster calculations and refined the silver parameters testing the planar physisorption of benzene and other three different heterocyclic aromatic molecules on a Ag_{32} model of the Ag(111) surface. We aimed at finding a balanced description of interaction energies and equilibrium distances: our fitting procedure resulted in an increased R_{vdW} value by 65% with respect to the original DFT-D2 value. The larger vdW radius effectively reduces the strength of the dis-

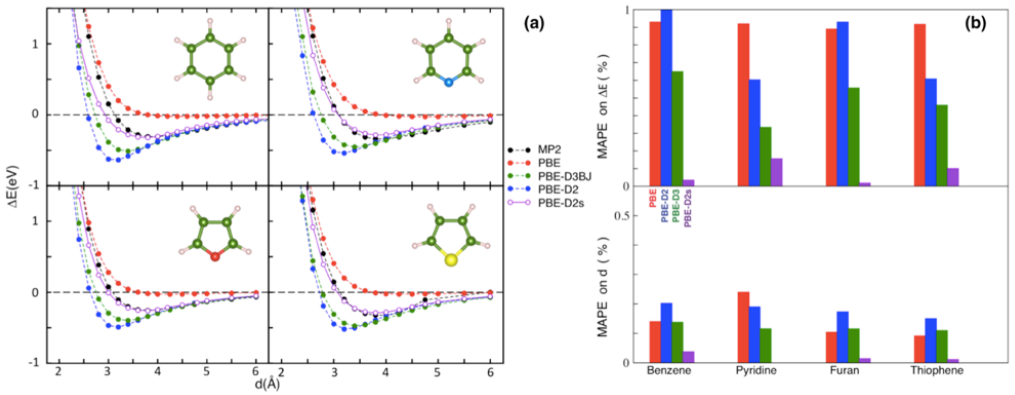

Figure 3.10: (a) Potential energy surface scan for the parallel adorption of the aromatic molecules on the Ag_{32} cluster top surface; (b) Mean Absolute Percentage Error (MAPE) with respect to MP2 considering the binding energy (top panel) and the minimum-energy distance (bottom panel).

persion interaction, thus correcting the well-known DFT-D2 overbinding tendency for physisorption of molecules on silver surfaces at no additional computational costs. In conclusion, we believe that the proposed strategy can be easily applied to other metallic systems and it can circumvent the computational costs of more refined non-local density functionals for qualitative studies of complex heterogeneous systems like the 2D hetero-interface between graphene, h-BN, phosphorene and transition metals that are applied as functional substrates. In Section 4.1 we report a study on extended graphene systems on Ag(111), conferming the transferability of our scheme. Furthermore, we believe that our reparametrization strategy can be easily transferred to other metals if one wanted to compute their interaction with molecular systems.

Computational Details We used the Gaussian09 program [63] to compute the MP2 and DFT calculation on a cluster model of the Ag(111) surface with adsorbed benzene, furan, thiophene and pyridine. To model the silver surface we use the Ag_{32} cluster model proposed by Caputo *et. al.* [185] that uses the experimental lattice constant for Ag (4.09 Å). This model has been extensively used in literature in computing MP2 adsorption of aromatic molecules on metals

[186, 187] and has been used as a reference for testing dispersion corrected DFT calculations [188, 189]. Here we use our MP2 calculations as a benchmark for the reparametrization of DFT-D2. Since MP2 has been extensively tested on metal clusters, giving good agreements with experiments and higher levels of theory [185, 187, 190, 191], we can consider it reliable for the adsorption of our molecules on the silver surface. We used a Stuttgart relativistic small core (RCS) 1997 basis set with effective core potential (ECP) for Ag, while the other atoms were treated through an all electron 6-311++G(d,p) basis set. Calculations were carried out with the PBE functional. Adsorption energies were corrected for the basis set superposition error with the counterpoise correction [192].

Chapter 4

2D Materials

Since monolayer graphene was synthesized for the first time with the scotch-tape method, the interest on this and all kinds of two-dimensional (2D) materials has boomed [193]. At first, were the unique properties of graphene to attract all the attention: its peculiar band structure, with the Dirac cones at the K points, the singular conductivity and mechanical strength, were something that had never been seen before in one material. Thanks to these exceptional properties, it was readily used for a number of different applications in electronics [194], optics [195], energy storage [196], transparent electrodes [197], DNA sequencing [198], drug delivery [199], catalysis [200] and many more [201]. From that point on, scientists started to be interested in any kind of 2D materials, with different structures and properties. As an example we can mention transition metal dichalcogenides (TMDs), hexagonal boron nitride, phosphorene etc.. All these materials are exfoliated from a 3D bulk with a layered structure, with van der Waals forces keeping the layers stacked on top of each other. They do not have a unique electronic structure, but cover the entire conductivity range from metallic to insulator, with the monolayers exhibiting very different properties from the bulk material from which they were exfoliated. Besides the unusual properties of such materials, what made them even more interesting is the fact that they can be functionalized through chemical modifications or interfaced between each other. This opens the door to even new and more interesting properties, that can be accurately tuned to achieve the structural and electronic features needed for the applications of

interest. Understanding the complex interactions at the interfaces of these van der Waals heterostructures is the main challenge in this field. The only way to design and build efficient devices is to intimately comprehend how the interactions between the materials at a microscopic scale affects their properties. In Section 4.2 of this chapter, we focus on a MoS_2/WS_2 heterostructure, investigating the effect of the interaction between the layers and on that of defects formation (Sulphur vacancies) on the electronic features of the 2D structure.

As chemists, amongst the world of possible applications of 2D materials, we are especially interested in their catalytic properties. In particular, graphene nanostructures (GNS) and TMDs have been widely studied, both experimentally and theoretically, as heterogeneous catalysts for different reactions. Some important reactions, with relevance in the sphere of clean energy production, are the oxygen and hydrogen reduction and evolution reactions. Such processes are in fact used in fuel cells to produce energy recombining molecular oxygen and hydrogen with water as the only by-product [202], or in (photo)electrochemical cell for the water splitting reaction, that can be used to reverse the process and store energy as chemical fuel. In Section 4.1, we analyze in detail the effect of doping and of a metallic support on graphene and how these affect the adsorption of oxygen, as a first step of the oxygen reduction reaction (ORR).

4.1 Doped-Graphene Ag(111)

We have already commented on the use of GNS as catalysts for Oxygen Reduction Reaction (ORR). The catalysis of this process is of utmost importance in fuel cells operation. At the time of writing, the most employed catalyst for ORR is metallic Platinum. This metal is in fact quite efficient as catalyst but has many limitations as its high cost and ease of poisoning due to the impurities present in the fuel (mainly CO) that make the electrodes less durable [203]. For these reasons there have been many attempts to use GNS as electrode materials, in order to improve efficiency, cost-effectiveness and durability. As a first step, GNS were used merely as a support for Pt nanoparticles, in order to reduce the content of the metal, which is still the one responsible for the catalysis. Then, actual metal-free

electrodes have been applied, featuring boron-doped or nitrogen-doped GNS, with improved efficiency and durability [204, 205]. These materials, being insensitive to CO, undergo a much slower degradation in operating conditions. To cite some examples, Qu *et al.* found that nitrogen-doped carbon nanotubes are more efficient by a factor 3 than Pt-based electrodes [206], many other experiments on N-doped GNS agree with this result [207, 208]; Yang *et al.* have instead investigated the boron doping, showing an enhanced O_2 adsorption and an improved catalytic performance at increasing B concentrations [209]. Recent theoretical calculations support these results, reporting a higher affinity of B-doped graphene for oxygen and the reaction steps of ORR to be more exothermic with respect to pristine graphene [210]. B-doped graphene has been reported both by experiments and measurements to be the best metal-free catalyst known to date, outperforming also N-doped graphene [211–213]. Even though the goal is the development of real metal-free catalysts, very often the use of GNS in fuel cells applications involves the presence of a metal contact [214]. Usually this is in the form of a metallic layer that supports the graphene sheet. This support may have several roles: it works as an electric connector and as a solid support for the flexible 2D layer, but it can also take part in the electronic rearrangements that occur during the catalytic process [215]. For these reasons, a detailed investigation of the interaction between graphene and this metal contact is needed. As we stressed over and over throughout this thesis, the properties of the interfaces are the crucial features to understand the reactivity of complex hybrid materials. At the time of writing, not many theoretical studies have addressed the metal-graphene interactions. Some have characterized the interface between B-doped graphene and Cu(111), showing a strong cooperation between the metallic support and graphene [210, 216]. It has also been shown that Cu has a stronger stabilizing effect on O_2 adsorption and enhances ORR reactivity on N-doped GNS, when compared to other metals as Ni and Co [217].

Here we look into the interaction between silver and graphene, investigating also the N and B doping of the latter and how these change the adsorption on the metallic substrate. We have selected silver as the metallic support because it has the following qualities: i) it is fairly cheap ii) it is an electron rich metal iii) the mismatch between its lowest energy surface (*i.e.* (111)) and graphene is not

too big ($\sim 2\%$) iv) its workfunction (4.74 eV) is lower than that of Cu(111) (4.94 eV) [218], meaning that the first is more ready to supply to the graphene layer the electrons needed for the reduction. Recent studies have reported the catalytic activity of large conjugated systems on silver surfaces [219, 220].

One of the reasons for the lack of theoretical literature on such a promising interface can be found in the inadequacy of the current computational tools. As discussed extensively in Chapter 1, the workhorse of computational materials science is DFT, especially when dealing with extended systems. Such layered hybrid structures are held together by weak dispersive forces that are completely neglected by standard Kohn-Sham theory. The available corrections are not really tailored to describe the interaction between metals and molecules. Here we report the results obtained using an approach developed for this purpose, based on a reparametrization of DFT-D2. The details about the method can be found in Chapter 3 and in the work published on the subject [62].

In a first part of the work discussed here we analyse the interaction between N- and B- doped graphene and silver surface; then we investigate the adsorption of an oxygen molecule on each of the graphene and graphene/silver systems [221].

4.1.1 Pristine Graphene Ag(111) interface

As a first step, we investigated the interaction between a pristine graphene sheet (G) and the Ag(111) surface. Here we compare three different dispersive corrections applied to the PBE DFT functional, namely DFT-D2 and DFT-D3 [20, 21] and our reparametrization of Grimme's D2 for silver (*i.e.* Ds) [62]. The supercell we built for G on Ag (AgG from now on) superimposing a 2x2 supercell of G to a 4-layer rotated $\sqrt{3} \times \sqrt{3}$ Ag(111) supercell. The (111) termination is confirmed from both theory and experiment to be the most stable silver surface [222]. The G layer is expanded by 1.52% in order to overcome the mismatch between the two lattices. We chose to adapt the graphene layer to the Ag slab instead of compressing Ag since these systems are usually obtained via chemical vapour deposition techniques [223]. Our model of the interface is depicted in Figure 4.1.

Many works employ the same surface slab model to reproduce this interface and to test different dispersion corrections [223–225]. This helps us compare our

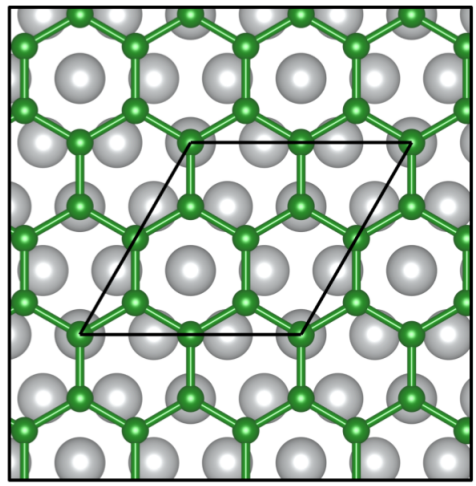

Figure 4.1: Hexagonal cell of the G-Ag(111) interface. A 2x2 graphene supercell is superimposed to four layers of a $\sqrt{3} \times \sqrt{3}$ Ag(111) cell. The experimental lattice parameter is used for silver, resulting in a cell parameter for the slab of a=$\sqrt{3}\sqrt{2}/2a_{Ag}$=5.009Å. The graphene lattice constant is expanded by 1.52% to match the silver surface slab. Colour code: C(green), Ag (grey).

work with recent literature. However, we do not aim at finding the most accurate and physically sound method to include van der Waals interactions in DFT, but only at using an affordable working method to investigate the Ag-G interface and the effects of doping on its electronic and structural features.

Experiments on graphene and graphene metal-interfaces are very often carried out in ultra high vacuum conditions. Nonetheless, in real applications as the one we target graphene is required to work in oxidizing environments as air. In this scenario, the electron-rich metal can work as a reducing agent, preventing the complete oxidation on the surface making the material more durable. Furthermore, the electron-releasing effect will most certainly affect the electronic structure of the system, working as some kind of extrinsic n-type dopant. Some modifications might be expected also from the mechanochemical effect of the strain applied to the graphene surface to match the different lattices.

With the slab model described above, we tested different dispersion correction schemes running a rigid scan of the distance between graphene and silver, depicted

in Figure 4.2. The system is held together solely by dispersive forces, as can be observed from the fact that PBE (red in figure), where these forces are missing, gives a completely unbound system. Grimme's D2 and D3 corrections are very convenient methods, since they compute the correction in a completely atomic parametrized pairwise potential, without adding any computational cost to the calculation.

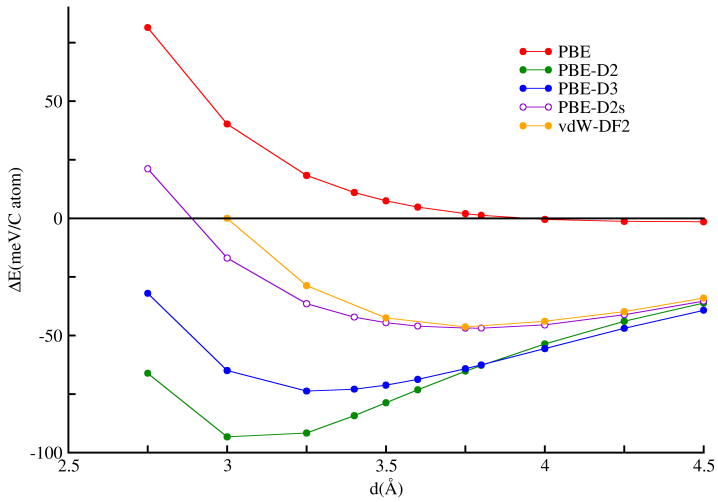

Figure 4.2: Energy scan at different G-Ag(111) distance, with different dispersion corrections. vdW-DF2 (orange curve), being the most accurate and expensive method, is used as a benchmark for our D2s dispersion scheme (purple curve).

One known flaw of these corrections is their being overbinding when treating transition metal-molecule interfaces [24,226]. Our recently proposed re-parametrization of DFT-D2 (see Chapter 3) improves significantly the performances of D2 for such systems by increasing the van der Waals radius of Ag by 65% in the dispersion damping function. Basically, we are turning off the dispersive contribution when the atoms are further apart with respect to standard DFT-D2. This scheme, developed for small aromatic molecules on Ag(111) is here tested for the AgG interface at hand (purple in figure) and found a good agreement with a more advanced den-

sity functional (*i.e.* vdW-DF2) that accounts for dispersion directly in the DFT calculation. We list in Table the adsorption energies and equilibrium distances (*i.e.* the minima from the curves in Figure 4.2).

Table 4.1: Adsorption energies and equilibrium distances for the Ag-G scan with the different dispersion corrections shown in Figure 4.2

	vdW-DF2 [225]	PBE-D2	PBE-D3	PBE-D2s
ΔE (meV/C atom)	-46.3	-93.3	-73.7	-46.8
d (Å)	3.75	3.00	3.25	3.80

Our DFT-Ds scheme gives an error on the adsorption energy with respect to vdW-DF2 that is two orders of magnitude smaller than Grimme's corrections. The difference is not so big on the adsorption distances, but still D2s gives the best approximation of the vdW-DF2

4.1.2 N- and B-doped graphene interaction with Ag(111)

We now report the interaction of doped graphene and silver, with same dispersion scheme as above and with a similar supercell model where we replaced one carbon atom with a nitrogen and a boron atom. In this way we introduce a n- or p-type dopant concentration of 12.5%. We ran a rigid scan as the one described in the previous section, this time using only the PBE-D2s method. Both the structural models and the scans are depicted in Figure 4.3, where we report again the curve relative to pristine graphene, for comparison.

G and GN present a very similar behaviour, with GB exhibiting a much stronger interaction with the surface. This is not unexpected, as GB is electron-deficient and should have a greater affinity for the electron-rich surface with respect to the other two systems. In this case, in fact, the interaction is not only dispersive in nature but it has some covalent character. This is shown very clearly from the separation of the two contributions: there is a minimum even in absence of dispersive contribution (PBE, red curve) which was absent in the other two cases. Obviously, this minimum is made deeper by adding the dispersive contribution (orange curve).

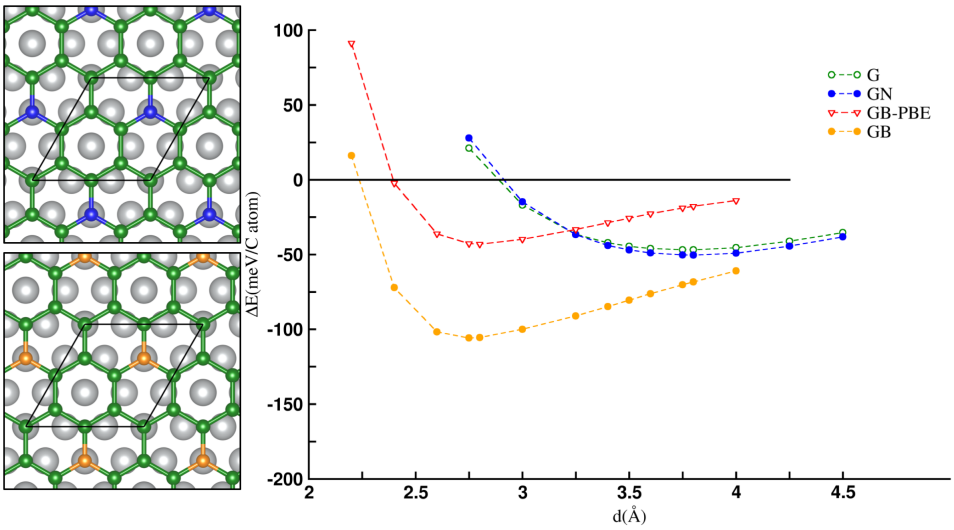

Figure 4.3: Hexagonal cell of nitrogen-doped graphene (top left) and boron-doped graphene (bottom left) on Ag(111); colour code: C (green), Ag (grey), N (blue), B (orange). Rigid distance scan between the graphene systems and the silver surface. G and GN behave similarly while GB is more strongly bound to the Ag surface; Colour code: pristine graphene (black) nitrogen doped graphene (blue) boron doped graphene (orange), PBE scan for boron doped graphene (red)

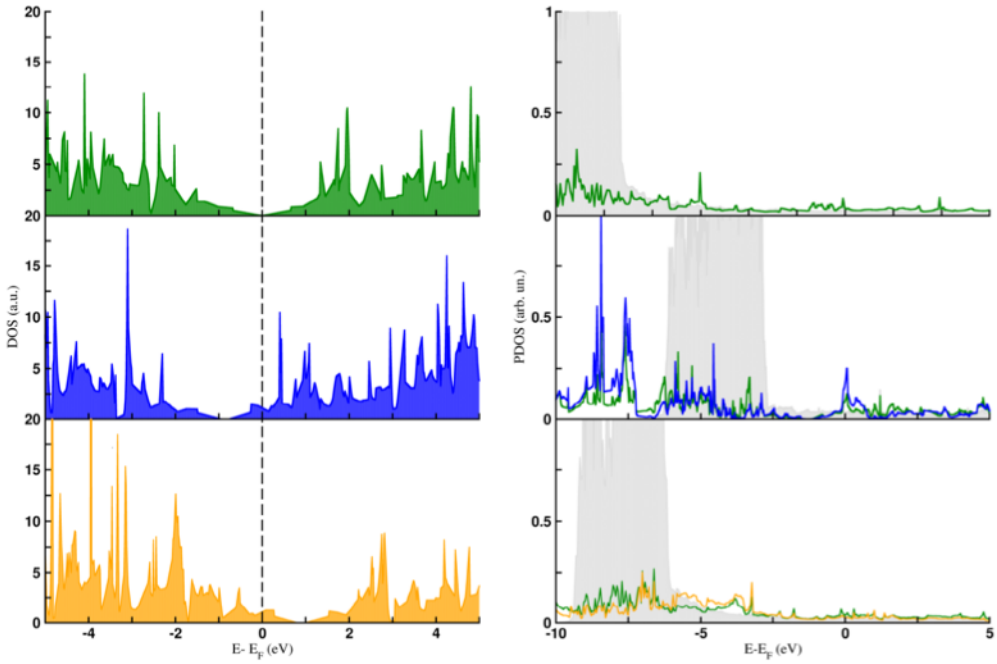

Figure 4.4: Density of States of G (top left), GN (middle left), and GB (bottom left), and atom angular momentum-projected density of states of Ag-G (top right), Ag-GN (middle right), and Ag-GB (bottom right). The α and β spin channels are symmetric and the sum of the two is reported in figure. Colour code: silver (grey), carbon (green) nitrogen (blue) boron (orange). In the left panels, the total DOS is reported, hence the states of carbon and those of the heteroatom are summed.

The different effect of the n- and p-type doping on graphene can be very clearly observed from Figure 4.4. The left panel of the figure, depicts the pDOS of the graphene layers without the silver support. The pristine graphene (green, top left panel) features the characteristic zero gap at the Dirac point with the cone arond it; with a finer k-point mesh this would be more evident [227]. The distortion induced by the dopant creates a very small gap (∼0.2 eV) in GN (blue, middle left panel) and GB (orange, bottom left panel). Here we can see very clearly how the Fermi level cuts through the conduction and valence band for n- and p- doping, respectively. From the right panel of Figure 4.4 we can observe the disruptive effect of the silver support on the electronic structure of the (doped) graphene sheets. The contribution of the d orbitals of Ag becomes dominant, any conical shape is lost, and the system becomes metallic.

We can also assess the role of silver and its different interaction with different doping on graphene by looking at the charge transfers occurring at the interface. When going from AgG to AgGN and to AgGB we found a charge transfer, from the GN sheet to the Ag surface ($\sim 0.13\ e^-$) and from the Ag to the GB surface ($\sim 0.56\ e^-$). The different direction in such charge transfer is perfectly consistent with the different kind of doping. The more electron-deficient GB accepting electrons from the surface. Charge density difference plots are depicted in Figure 4.5 and show a charge variation that is consistent with the aforementioned variations. The effect of the charge variation is mostly delocalized on the whole surface, though some minor local effects are observed in proximity of the dopants.

From the data collected so far, we can conclude that the silver support does not play a merely structural role, but effectively modifies the electronic structure properties of the hybrid systems. In the next section we will see the effect that it has on the adsorption of a O_2 molecule on these surfaces.

4.1.3 Oxygen adsorption

The catalysis of ORR in fuel cells, or its reverse (oxygen evolution) for water splitting in electrocemical cells, are among the most important potential applications of graphene systems. Clearly, a key step for any catalytic process is the binding of the substrate to the catalyst, which can have major consequences on the overall

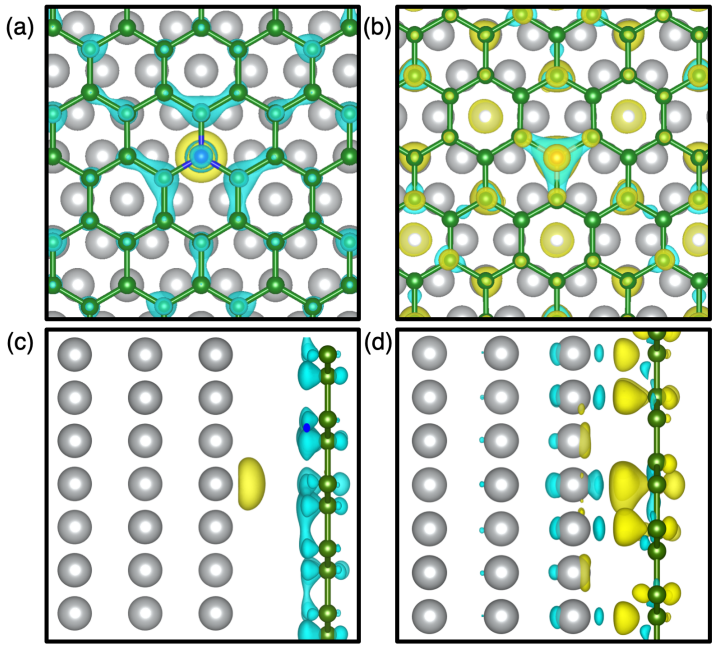

Figure 4.5: Charge Density Difference isosurface plots for AgGN and AgGB computed as $\rho_{CDD} = \rho_{AgGX} - \rho_{Ag} - \rho_{GX}$ (X = N and B). Top (a) and side (c) view of AgGN, top (b) and side (d) view of AgGB. Color legend as in Figure 4.3, yellow and cyan surfaces represent positive and negative ρ_{CDD} values, respectively (isodensity values of 0.0005 and 0.001 a.u. for AgGN and AgGB, respectively

efficiency of catalysis. Here we report the investigation of the adsorption of an oxygen molecule on the six systems described in the previous sections. First, we optimize the stucture of an isolated O_2 molecule in vacuum and on a 4x4 supercell of G, GN and GB. The minima for these optimizations are depicted in Figure 4.6.

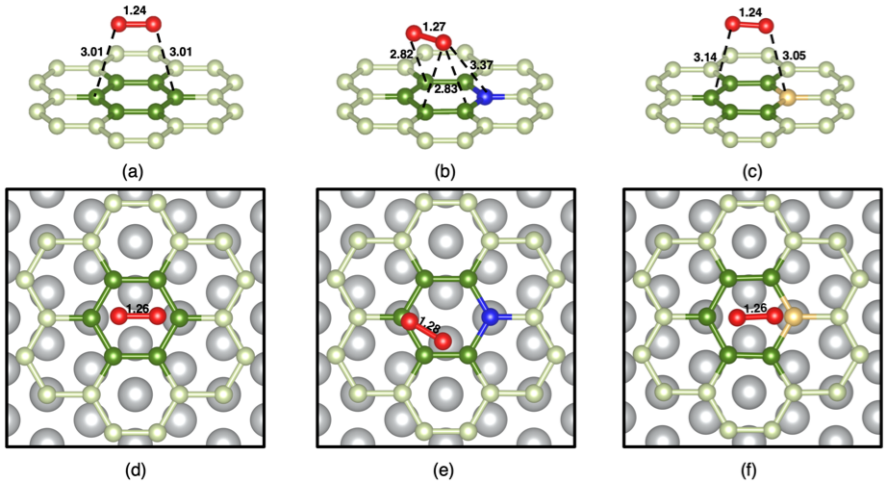

Figure 4.6: Optimized geometries of the oxygen adsorbed on G (a) GN (b) and GB (c). Of the 4x4 cell used, the pictures only shows the ring on which O2 is adsorbed and the immediately adjacent ones. Bond distances are reported in Å. The same geometries were used to calculate the adsorption energy on Ag(111). Colour code: oxygen (red) carbon (green) nitrogen (blue) boron (orange); a darker shade of green is used for carbon atoms in the central ring.

The effect of the heteroatom on the adsorption is immediately evident from the analysis of the geometries. In pristine graphene the molecule lies parallel to the surface, at the centre of a hexagon, suggesting only a physisorption, with no covalent contribution. When N is present, the molecule rotates an tilts towards the surface, one of the oxygen atoms pointing at the nearest neighbour C atom to N. A depletion of charge on this carbon atom (see Figure 4.5), due to the higher electronegativity of N, attracts the lone pairs of that oxygen atom. We can observe a slight elongation of the oxygen molecule as well, as it moves closer to the surfaces. All the above suggests a stronger binding of the substrate to n-doped graphene with respect to the parent material, as is confirmed by the binding energies shown

in Table 4.2, computed as

$$\Delta E = E_{Surf}^{O_2} - E^{O_2} - E_{Surf}$$

Table 4.2: Binding energies of an O_2 molecule calculated as described in text on G, GB, GN, and on Ag-G, Ag-GN, and Ag-GB. A negative sign indicates a favourable adsorption process. O_2 bond length in the adsorbates shown in Figure 4.6 and charge variations going from G(X) to Ag-G(X), calculated as $\Delta q_i = q_i(AgG(X)) - q_i(G)$,where X represents the heteroatom and q_i the Bader charge on the i-th atom. The total charge is expressed as $\Delta q_{tot} = \sum_i \Delta q_i$ that represents the variation of electronic charge (from top to bottom) induced by the silver support on the whole (doped) graphene sheet, on the oxygen molecule, on the heteroatom and on all the carbon atoms

	G	GN	GB	Ag-G	Ag-GN	Ag-GB
ΔE (eV)	-0.14	-0.16	-0.11	0.28	0.09	-0.47
d_{O-O} (Å)	1.24	1.27	1.24	1.26	1.28	1.26
$\Delta q_{tot}(e^-)$	-	-	-	0.22	0.08	0.61
$\Delta q_{O_2}(e^-)$	-	-	-	0.17	0.11	0.14
$\Delta q_X(e^-)$	-	-	-	-	-1.13	1.93
$\Delta q_C(e^-)$	-	-	-	0.05	-0.02	0.45

The adsorption geometry on GB is very similar to the one on G. The molecule here tilts slightly towards Boron (where the electron deficiency lies) but remains relatively far from the surface, the binding energy being smaller than in the other two cases.

We relaxed again the oxygen molecule on the surfaces with the presence of the Ag(111) support. Even though no major effect can be observed on the geometries, the effect on the binding energies is striking (Table 4.2.) In AgG and AgGN the adsorption is made unstable by the presence of the support, the energies becoming positive. This can be explained with the electron-rich environment having a destabilizing effect on the oxygen molecule. This can be observed also in the total charge variation on the G-O_2 system when we include the Ag surface: charge is transferred from silver to the G-O_2 system. Being GN already fairly electron-rich, the destabilizing charge transfer to the molecule comes directly from the doped-

graphene sheet, though to a lesser extent. Conversely, the effect of the support on GB stabilizes oxygen adsorption. The charge transfer is still occurring, but most of the charge is accepted by the doped-graphene surface, on which it has a stabilizing effect that lowers the energy of the whole adsorbate.

We have shown one more time that the silver support is far from being inert: it provides not only mechanical support and an electrical contact but actively affects the electronic properties of the hybrid structure, having a major effect on the interaction with the substrate for catalysis.

In conclusion, we have presented a detailed investigation of graphene and of the effect of p- and n-doping and of the interaction of this systems with Ag(111), focusing on the adsorption of graphene on the metal and on the modifications of the electronic structure induced by it. This system is quite challenging for current state-of-the-art DFT methods due to the dominance of dispersive forces. Here we have validated our reparametrization of Grimme's DFT-D2 develped for small organic molecules on Ag(111) (see Chapter 3). We have seen that it is transferable to extended systems, outperforming the standard D3 and D2 and showing an accuracy comparable with a more advanced and expensive van der Waals density functional (vdW-DF2).

We have considered both n- and p-type doping on graphene, by substituting a C atom with a N and B atom, respectively. We have studied how these substitutions do not only alter the electronic structure of graphene, but largely affect the interaction with silver and ultimately the adsorption of oxygen. By comparing the pristine, doped, and silver supported systems we have been able to decouple the effects of the substrate from those of the dopants and to understand how they combine. This is of outmost importance to understand and design graphene-based systems for the applications we need. One important result is that the role of the silver support is not only structural, but has a massive influence on the electronic structure features of graphene.

As a first step of ORR catalysis on GNS electrodes, we have investigated the adsorption of an oxygen molecule on the systems under study. One again we were able to dissect the role of the dopants from that of silver. The improved oxygen adsorption in GB due to the presence of the Ag(111) support is a very important

result, since GB is already reported as the best carbon-based metal-free catalyst known to date. We can conclude that the silver support, by providing some extra electrons, can further boost the performance of the already effective boron-doped graphene. We are well aware of the fact that we are neglecting many factors present in operating conditions (*e.g.* solvent, temperature, voltage) that can affect ORR catalysis. Still, this preliminary study provides practical insights on the effect of different modifications on the catalysis and provides a good starting point for further investigations aiming at the full characterization of the ORR mechanism. Furthermore, our DFT-D2s results could be refined by more advanced methods that exploit the density functional embedding theory [228] (Chapter 3).

Computational Details For this part of the work we performed periodic calculations in VASP, correcting PBE with our DFT-D2s scheme for dispersion. A kinetic energy cutoff for the plane waves of 750 eV was used. In the rigid distance scans a 11x11x1 Γ-centered k-point mesh was used.

4.2 MoS_2/WS_2 heterostructures for photocatalysis

Among the 2D materials that acquired attention after graphene, TMDs are one of the most extensively studied [229]. TMDs cover a broad range of electrical and conducting behaviours and their properties are easily engineered tuning the layer thickness and nanoparticle morphologies. Different polytypes exist, depending on the coordination around the metal atom and on the stacking on the layers. Octahedral and prismatic environments are both stable, with major consequences on the electronic features of the material due to the different splitting of the d orbitals. In their 2H (trigonal prismatic) phase, they have a semiconducting behaviour and optical gaps in the visible and near-infrared range. Thanks to these properties, they have been largely deployed as field-effect transitors [230–232] and for small-scale electronic devices and logic circuits [233, 234]. Size has a major effect on the electronic structure: a switch from direct to indirect band gap occurs when a monolayer is carved out of the bulk, besides excitonic effects emerge due to the loss of out of plane dielectric screening and the break of inversion symmetry yields a spin orbit coupling (SOC) interaction that has a major effect on the

band structure and optical spectrum. As the size approaches the atomic scale, an enhancement of the light-matter interaction is observed that makes such materials interesting as opto-electronic devices [235–237] ad as electro-catalysts for hydrogen evolution reaction (HER) in photo-electrochemical cells (PECs) [238, 239].

Once again, a big opportunity is presented by the possibility of building van der Waals heterostructures, stacking different TMD monolayers on top of each other. Researchers have extensively investigated the heterostructures composed by MoS_2 and WS_2, whose type-II band alignment promotes a separation of the hole and electron with an ultra-fast charge transfer [240], hot interlayer exciton formation [241] and promising water splitting catalysis properties [242, 243]. Many theoretical works have focused on the study of both TMD monolayers [244–249] and heterostructures [250–252]. Many of the theoretical studies relies on DFT to evaluate the electronic structure properties of these materials. Unfortunately, DFT results are strongly dependent on the choice of functional and parameters involved, very often failing in giving reliable quantitative values, even though being qualitatively correct. Moreover, there is the already extensively discussed flaw of the lack of dispersive forces in this theory (vide supra). Some have tried to use LDA to reproduce the experimental geometries, resulting in a good approximation only due to the overestimation of the covalent interaction that compensates for the lack of dispersion. A correct choice of the parameters is crucial to obtain the right geometries (that largely affect the electronic properties) and sometimes a more expensive XC functional must be used to achieve that.

In this section, we report the characterization of the structural and electronic properties of a MoS_2/WS_2 interface and of the separate monolayers. In order to assess their possible activity as water splitting photocatalysts it is mandatory to account for defects in these systems. These materials are in fact known to be inert on the basal planes, their reactivity is much higher around line (edges) and point (vcancies) defects. Defects affect the electronic and optical properties and introduce active sites of adsorption and catalysis on the basal planes of TMDs that would be otherwise inert [253–257]. Sulphur vacancies are arguably the most important defects in these materials, causing effects like defect-bound excitons [258, 259], single-photon emitters [260] and mid-gap states that yield optical transitions below the neutral-exciton emission line [261, 262]. In order to

engineer the defects to build active catalysts for water splitting, it is really important to understand their role in the catalytic process. To this end, computational investigations can help dissect different effects in the defect formation and obtain atomic-scale information unveiling structure-property relationships.

We report a benchmark study on the electronic structure of the MoS_2 and WS_2 monolayer and their quasi 2D heterostructure. We compare the accuracy of semi-local and hybrid DFT results both in reproducing experimental geometries and in describing the electronic properties. The study is performed for both pristine and more costly defective materials. Our aim is to set a definite scale to assess the efficiency of each level of theory taking as reference the best possible accuracy at the least computational burden.

The 2H phase of MoS_2 and WS_2 belong to the space group P63/mmc, the unit cell containing two layers of the TM and 2 Sulphur atoms per layer covalently bonded to it. The layers interact via van der Waals forces. In each layer of the 3D strucure, the transition metal is in a trigonal prismatic coordination. We build the slab of the monolayer (ML) cutting one of the layers and adding 10 Å of vacuum to separate it from the periodic images. When studying the defect formation, we removed one sulphur atom from a 5x5 supercell, modelling a $2\%_{atom}$ concentration of the defect. This way, the distance between one vacancy and its images is around 15 Å, so that we can consider them as isolated. We built the heterostructure by stacking two monolayer from the different oxides on top of each other and adding 10 Å of vacuum. The defective heterostructure was also built by removing a sulphur atom from the 5x5 supercell. In this case, four non-equivalent vacancies can be formed: two per TMD layer, times two per side (inside or outside the interface). Here the concentration is $1\%_{atom}$ and the separation is again abount 15 Å.

We performed a full relaxation of the pristine bulk of MoS_2 and WS_2, converging the forces up to 0.03 eV/Å and the energies up to 10^{-8}. Calculations were run with the PBE, PBE0 and HSE06 functionals with VASP, using a 800 eV cutoff for plane waves and 8x8x2 Γ centered k points mesh. The dispersion correction was accounted for with Grimme's method DFT-D3 with BJ damping. In the ML and heterostructures we relaxed only the atomic positions, keeping the lattice parameters fixed at their bulk values.

We computed the band structures of the systems described above at the PBE, HSE and PBE0 levels of theory, converging them up to 10^{-5} eV. These band structure were computed along the $\Gamma - K - M - \Gamma$ path in the reciprocal lattice, considering 10 divisions in each segment. Band structures have been evaluated both at the HSE-D3BJ level and at the same level used for the structural optimization. As a general scheme, we analyze the electronic structure properties of the hetero and defective systems via HSE06 ran on top of the PBE-D3BJ geometries, as discussed below.

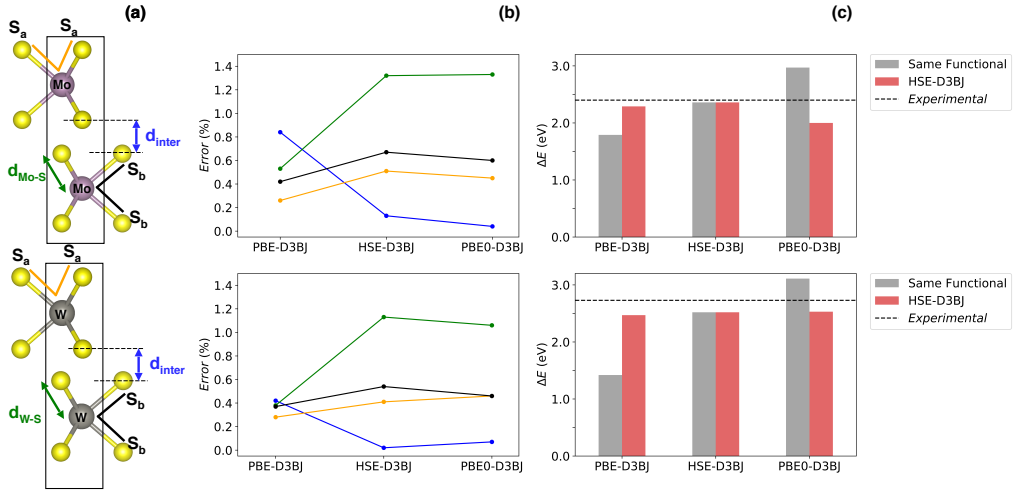

Figure 4.7: Structural parameters for MoS_2 and WS_2 (a). Absolute percentage error of the different functionals on the structural parameters with respect to experiments [263, 264] (b). Eigenvalue gap evaluation with the same level of theory used for the optimization and with HSE06, compared with the experimental reference [265, 266].

We ran geometry optimizations with PBE and the hybrids HSE and PBE0, to compare their ability to reproduce the experimental geometry. Figure 4.7 shows this geometry and the error of the different XC functionals with respect to the experimental one. The left panel of the figure depicts the unit cells of MoS_2 (top) and WS_2 (bottom) highlighting the structural parameters on which we evaluate the

different functionals. We take into account two angles: S_a-TM-S_a and S_b-TM-S_b, the interlayer distance d_{inter} (*i.e.* the vertical distance between suplhur atoms in two different layers) and the TM-S bond length d_{X-S}. The middle panel of Figure 4.7 shows the absolute percentage error on these four parameters of PBE, HSE and PBE0 with respect to the experimental geometries taken from references [263,264]. A very similar trend is observed in MoS_2 and WS_2. PBE-D3BJ better reproduces the TM-D bond distances (green in figure), these distances being underestimated by hybrid potentials (HSE-D3BJ-$d_{Mo(W)-S}$ = 2.38 Å, PBE0-$d_{Mo(W)-S}$=2.38 A (2.39 Å), EXP-$d_{Mo(W)-S}$= 2.4 Å (2.41 Å)). This is probably due to the more ionic contribution given by the Hartree-Fock exchange contribution, giving shorter bond lengths. On the angles, the functionals give the same values within a 1% deviation.

We have also studied how the different starting geometrical minima affect the electronic structure properties of the monolayers. In particular, we have computed the electronic band gaps of the two monolayers cut from the pre-optimized bulk structures with both the HSE level of theory on top of the different geometries and with the same level of theory used in the respective optimization. The deviations with respect to an experimental reference [265,266] are depicted in the histograms in Figure 4.7 (a). The band gap reported is in each case the direct eigenvalue gap at the K point. When using the same level of theory for both relaxation and band structure calculation, HSE06-D3BJ looks like the best choice. Still, if we look at the HSE values on top of the other geometries, we note that the gaps are quite insensitive of the starting geometry. Hence, where one could not afford to run the geometry optimization with the hybrid functional, a single point at the HSE level on top of the PBE structure would give results that are almost as good.

The band structures and pDOS at the HSE on HSE level are depicted in Figure 4.8. We can observe the direct nature of the gaps at the K high symmetry point, as expected from literature. From the pDOS we can see how the edges of the frontier bands are mainly composed by the d states of the transition metals. Hence, d - d transitions will be the ones responsible of photexcitation and exciton formation. Table 4.4 lists the splitting due to the SOC computed both at the HSE and PBE levels of theory, showing again a good agreement with literature [251, 252].

Once we have confirmed that our method is in good agreement, both qualita-

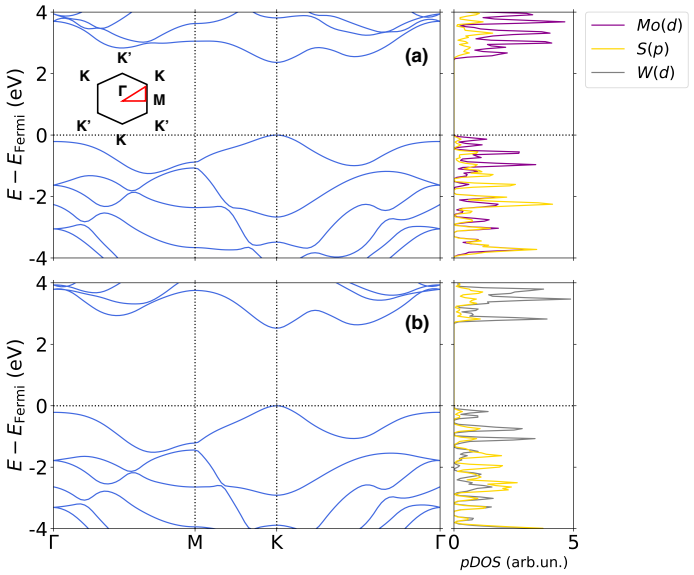

Figure 4.8: Band structures and atom- angular momentum-projected densities of states of MoS_2 (a) and WS_2 computed at the HSE06-D3BJ level of theory on top of the optimization carried out with the same level of theory on a 5x5 supercell of the pristine TMDs. The inset in figure (a) represents the path through the high symmetry k-points on which the band structure is computed.

Table 4.3: Spin-orbit splitting Δ_{SOC} occurring (at the point K) both in the valence and conduction bands of MoS_2 and WS_2 pristine monolayers calculated by means of PBE and HSE XC functionals.

		Δ_{SOC} (meV)	
		VB	**CB**
MoS_2	PBE	147	3
	HSE	204	33
WS_2	PBE	420	37
	HSE	551	39

tively and quantitatively, with literature, we can use it to address the formation of defects and see how they affect the electronic structure properties.

Considering the presence of a Sulphur vacancy in the structure, we observed a change in the nature of the bandgaps for both compounds that become indirect with the VBM located in the point K and the CBM in correspondence of the point Γ of the reciprocal space. The bandgap value is respectively for MoS2 and WS2 1.84 eV and 1.98 eV that are smaller than the values obtained for pristine compound (2.36 eV and 2.52 eV). The smaller value for the defective systems is due to the appearance of mid-gap states that strongly affect the electronic properties of these compounds. Our findings of new bands arising in the mid-gap are in accordance with other references [251, 267, 268]. In both compounds, a defect state appears inside the gap, mostly due to the transition metal atoms near the vacancy that are reduced by the excess charge left by the leaving sulphur (Figure 4.9) The presence of mid gap defects has been also experimentally observed for WS2 slabs, and the arising defect states have found to split due to SOC effect [268].

The energies needed to form such vacancies are (at the PBE level) 2.87 eV for MoS_2 (in agreement with [269]) and 2.99 eV for WS_2. The positive values confirm the expected result that Sulphur vacancies are not native in these materials. From a structural point of view, the presence of a Suplhur vacancy changes the atomic arrangement of both disulphides. Table 2 lists the variations of three selected representative parameters after the HSE optimization of the defective monolayers. These parameters are the distance between two of the nearest vacancy neighbours

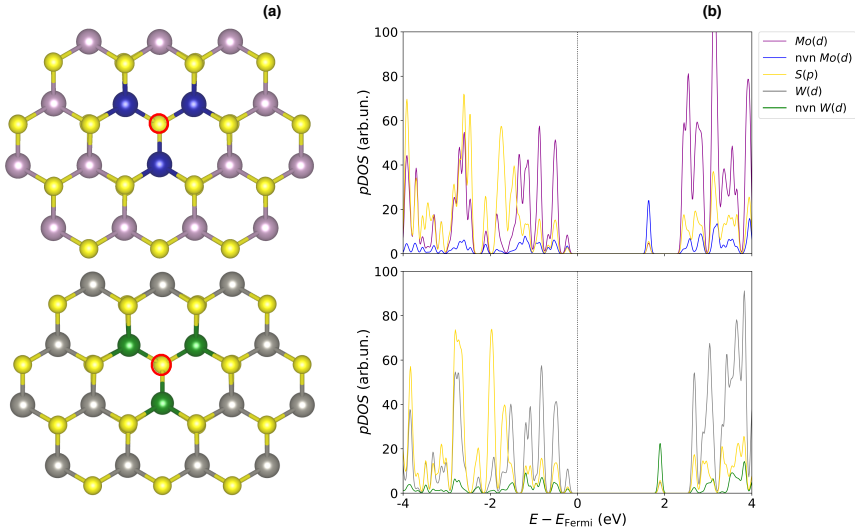

Figure 4.9: Top view of the Sulphur vacancy optimized at the HSE level in monolayer MoS_2 (a) and WS_2 (b) only a few unit cells of the periodic structure are shown in figure and the transition metals in contact with the vacancy are highlighted in blue. Atom-angular momentum-projected densities of states (pDOS) at HSE level for the defective monolayer MoS_2 (a) and WS_2 (b) the contribution of the transition metals nearest neighbours to the vacancy (XNN) has been separated from the rest of the transition metal atoms in each case. Colour code: S (yellow), Mo (purple) W (grey) XNN (blue).

(nvn) TM atoms (depicted in blue and green in Figure 4.9), the distance between one of those atoms and the remaining sulphur atom (below the vacancy) and the angle between the two TM atoms and the sulphur one. Any two among the three nvn atoms can be selected, since angles and distances are equal by symmetry.

Table 4.4: Variation of three geometrical parameters after HSE optimization of defective monolayers. Δd_{TM-S} and Δd_{TM-TM} are the variations of the distance between the TM atoms and the remaining Sulphur atom and the one between two nbn TM atoms, respectively. $\Delta\theta_{TM-S-TM}$ is the angle between two nvn TM atoms and the residual Sulphur atom.

	Δd_{TM-S} (Å)	Δd_{TM-TM} (Å)	$\Delta\theta_{TM-S-TM}$ (°)
		VB	**CB**
MoS_2	-0.03	-0.12	-2.11
WS_2	-0.02	-0.14	-3.29

The values listed in Table refer to the atoms that are closest to the vacancy and experience the most significant variation. However, moving away from the point defect, minor variations can be observed on similar parameters. The sign of the values indicate a contraction of the whole structure around the site that used to be occupied by Sulphur. This geometrical reorganization is accompanied by a charge redistribution. Table 4.5 lists the average values of the Bader charges variations upon vacancy formation. In MoS_2 (first entry) we can observe that the residual charge left by the leaving Sulphur atom, mostly delocalized on the Sulphur sublattice, with a minor local effect on the S below the vacancy site. As a result of the reduction of the Sulphur atoms, TM atoms are partially oxidized. This last effect is less evident on the nvn TM atoms, probably due to the fact that they also accept a part of the charge left by the missing Sulphur. A different picture can be observed in WS_2, where the charge is locally distributed on the nvn W atoms.

After the characterization of the monolayers, we address the properties of a MoS_2/WS_2 heterostructure. Figure 4.10 depicts the bilayer, highlighting the optimized interlayer distance and the projected band structure. From the latter it is possible to dissect which bands are due to which layer and also where hybridiza-

Table 4.5: Average values and valence of the atomic charge variations upon defect formation. The first column lists the average values for the three TM near the vacancies. Column three lists the average on all the other TM atoms, column five and six report the variation on the Sulphur below the vacancy and the average on all the other S atoms, respectively. For each column, the one on its right lists the variance on the values. Positive (negative) values indicate electron loss (gain).

	nvn TM	σ^2	TM	σ^2	nvn S	σ^2	S	σ^2
MoS_2	0.12	0.00	0.26	0.01	-0.17	-	-0.13	0.01
WS_2	-0.18	0.01	0.01	0.01	-0.03	0.01	-0.01	0.01

tion of the states from both materials are present. The band gap is again indirect, the maximum of the valence band being at the Γ point and the minimum of the valence band being on K. Furthermore, the colours in figure highlight the fact that the top of the VB is mainly due to WS_2 and the bottom of the conduction band due to MoS_2. Hence an interlayer charge separation would occur upon photoexcitation. This is in agreement with the type-II band alignment reported for this inteface [240] and could have major consequences for catalysis. That is, after photoexcitation, the electron on MoS_2 can perform the reduction (HER) while the hole on WS_2 performs the oxidation (OER).

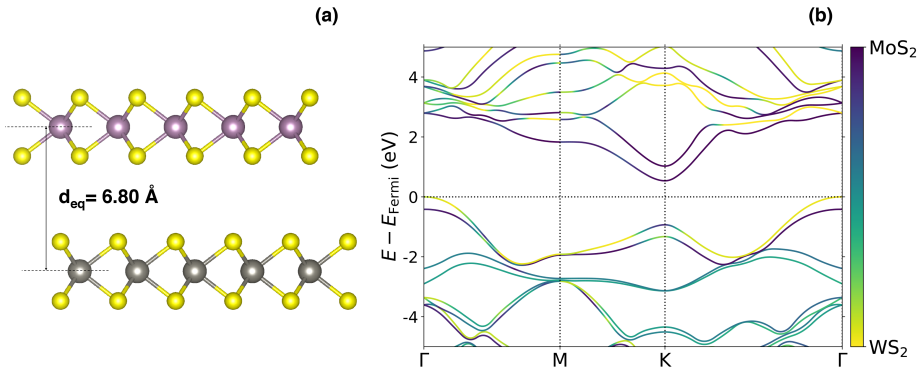

Figure 4.10: Side view of the MoS_2/WS_2 interface (a) and layer-projected band structure (b)

The next step is the characterization of the Sulphur vacancies in the het-

erostructure. Four possible configurations exist of a single defect in the bilayer and are all depicted in Figure 4.11 with the relative pDOS.

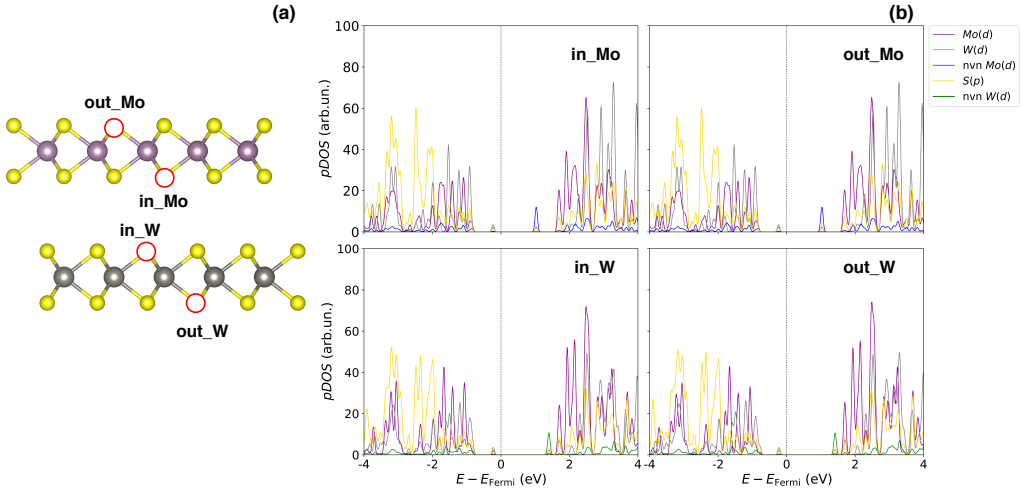

Figure 4.11: Side view of the interface with the four possible sulphur vacancies (a) pDOS of the respective defective monolayers (b) the TM atoms near the vacancy are separated from the rest (nvn) to highlight the charge redistribution upon defect formation

In each case we calculated the formation energy of the vacancy at the PBE-D3BJ level. In the case in which the vacancy is on the outer side of the interface, we obtained respectively for MoS_2 and WS_2 ΔE_{vac} =2.85 eV and ΔE_{vac} = 2.99 eV. These values are quite like the ones obtained for corresponding energies in the monolayers indicating that the interface does not have any effect on the outer defects. Regarding the vacancy in the inner part of the interface, the values we obtain are ΔE_{vac}=2.97 eV for Molybdenum disulphide and ΔE_{vac}= 3.11 eV for Tungsten disulfide. First, it is possible to note that the values obtained for MoS_2 are smaller than the ones of WS_2 both for the inner and the outer vacancy. This trend is probably due to the strength of the bond of the TM-S that is larger for the W due to its smaller charge-ionic radius ratio. Moreover, the energy necessary to form the vacancy within the interface is bigger than the one required to form

the same vacancy at the interface with vacuum. This is probably due to the destabilizing interaction between the excess electrons left behind by the leaving sulphur and the Sulphur lone pairs on the other side of the interface.

As it is possible to observe, in all cases shown in Figure 4.11 defect states appear above the Fermi level with respect to the case of the pristine interface (see Figure 4.12). These states (blue in Figure) are highly localised on the three TM-d orbitals that were bonded to the absent S atom. It seems that there is no difference between the cases of inner and outer vacancy on both compounds. However, differently from the case of vacancy on MoS_2 in which the defect states arise in the mid gap, when the Sulphur atom is subtracted from the WS_2 the defect states arise as a continuation of the conduction band. These states, arising near the CB edge, would not limit the light adsorption efficiency by trapping the electrons. However, they would cause the loss of the inter-layer band alignment since the frontier states both belong to WS_2.

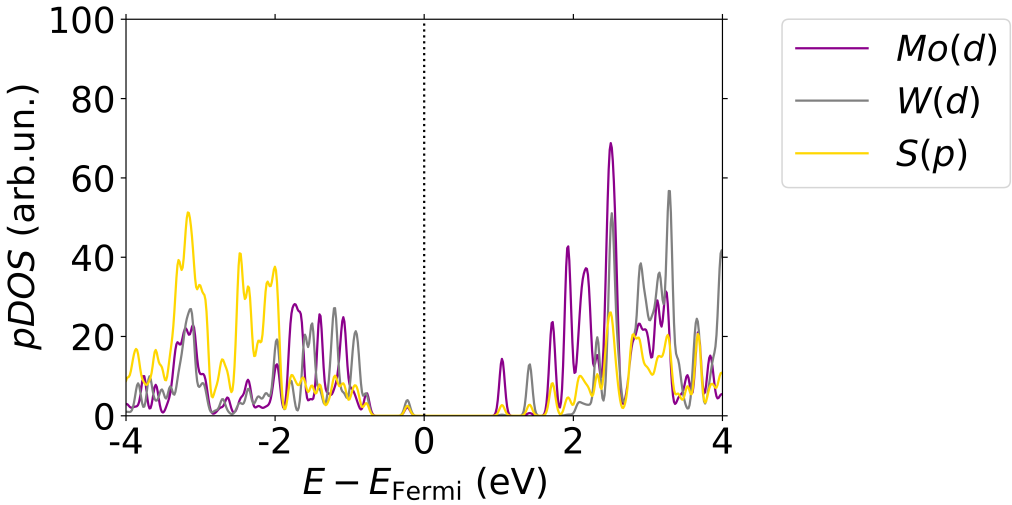

Figure 4.12: atom-angular momentum-projected dos of pristine MoS2: WS2 interface calculated at HSE-D3BJ level on top of PBE-D3BJ ground state geometry optimization

To sum up, we have performed DFT calculations in order to compare three different levels of theory in accurately predicting the ground state geometry. We found that PBE-D3BJ outperforms the hybrid functionals in predicting the TM-S bond length while it behaves as well as HSE and PBE0 in predicting the two angles, chosen as reference geometrical parameters in our study. Electronic properties such as bandgaps are well predicted by the HSE-D3BJ level of theory on top of PBE-D3BJ optimized geometry as well as on top of the more costly hybrid geometrical relaxations. Therefore, balancing both accuracy and computational cost, since the PBE-D3BJ deviations differ from the hybrid ones no more than 1%, we can conclude that the semi-local optimization gives sufficiently accurate geometrical parameters for our purpose. Evaluating the starting geometry at the PBE-D3BJ level and then studying the electronic properties by means of HSE functional can be not only a good trade off between computational cost and accuracy but it can be extended to more realistic defective systems (i.e. containing atom vacancies) for which more costly optimizations could be prohibitive. This is confirmed even in case of defective slabs for which band structures calculated at the HSE-D3BJ level on top of both PBE-D3BJ and HSE-D3BJ optimizations do not show neither qualitative nor quantitative differences. Therefore, it is possible to conclude that, extended systems too demanding to be relaxed by means of hybrid functionals, and for which one is interested in electronic properties, can be treated with different levels of theory for relaxation and calculation of BGs. With this computational approach, we have been able to investigate the formation of a Sulphur vacancy (that is crucial to activate the otherwse inert TMD sheets towards catalysis) in the MLs and how it affects the electronic structure properties. We have reported the formation of intragap states that can interfere with the photoexcitation process. We have addressed the electronic structure properties of the MoS_2/WS_2 heterostructure, confirming the type-II band alignment that allows the electron-hole separation that can be exploited to catalyse both the half-reaction of water splitting on the opposite sides of the interface. Finally, we have investigated the effect of the vacancies on the heterostructure, showing that it is dramatically dependent on the vacancy position. When the latter is on MoS_2, in fact, the electronic structure is similar to that of the ML, while when it is localized on the WS_2 sheet, it causes the loss of the inter-layer charge separation.

Computational Details We performed a full relaxation of the pristine bulk of MoS_2 and WS_2, converging the forces up to 0.03 eV/Å ad the energies up to 10^{-8}. Calculations were run with the PBE, PBE0 and HSE06 functionals with VASP, using a 800 eV cutoff for plane waves and 8x8x2 Γ centered k points mesh. The dispersion correction was accounted for with Grimme's method DFT-D3 with BJ damping. In the ML and heterostructures we relaxed only the atomic positions, keeping the lattice parameters fixed at their bulk values. MLs were relaxed again after removing a Sulphur atom to model the vacancy.

Final Remarks and Perspectives

As the years go by, first principles tools keep gaining ground in the field of materials science. The level of detail at which they allow us to look at the features of materials opens the door to the possibility of a rational design of new functional materials. By deeply understanding their structural and electronic properties and how they affect each other is in fact possible to tune them in order to get the ones we desire for our target application. Throughout this thesis we have repeatedly shown that this is possible for a number of systems and a number of applications. For the greatest part, such applications have been in the field of solar energy conversion, some other on (photo)catalytic processes, still in the field of clean energy production an renewable energy sources. In studying newly synthesized push-pull dyes on the NiO surface as a DSSC photocathode, we have shown the paramount importance of accounting for the interface in order to get qualitatively correct results. In this way, we have been able to predict from first principles calculations the relative efficiencies of the different dyes, highlighting once again how the computational modelling can assist the interpretation of the experiments, explaining the measured trends. We have proposed alternative oxides for p-DSSC as an alternative to NiO, which is the main responsible of the low PCE obtained so far in these devices, being able to extract important parameters directly related to the PCE from the electronic structure features of the materials. We have investigated how atomic substitutions affect these properties, so that, understanding the connection between structural modifications and their effect on the electronic structure, we can use the former to tune the latter to achieve the properties we desire. In the comparison between different oxides, $CuGaO_2$ has emerged as the most promising one. We chose it to investigate further the role of Mg doping and to look at the

interaction between anchoring groups and delafossite oxides, finding a remarkable agreement with experimental results and a strong preference for the monodentate anchoring modes. The latter suggests an improved efficiency due to the more unlikely deactivation of the hole-injection process due to surface protonation. In the same field of solar energy conversion, we studied a possible photocatalyst for CO2RR. With the idea of recovering the CO_2 already present in the atmosphere, converting it back to chemicals that can be used in a carbon-neutral way. We have investigated the properties of another delafossite oxide ($CuFeO_2$), with a band gap too small to be exploited in DSSC devices. Its adsorption in the visible range can instead be exploited for photocatalyisis. We have proven that this material can be active in such a reaction, thanks to the suitable allignement of its band edges with the redox potentials of CO_2 reduction to different products. We have characterized the adsorption and activation of a CO_2 molecule on the surface, proving the need for oxygen vacancies for the reaction to occur, and the active role of Fe atoms in the interaction with the substrate. Sometimes the current tools of computational chemistry are not suitable to give us accurate enough results for our investigations. In these cases we developed new approaches, retuning the existing ones in the attempt to make them able to catch the desired properties in the study of our materials. To improve the modelling of hybrid dye-semiconductor interfaces, we relied on DFET, completing its implementation in the VASP program and testing its performance on some real world system. The partition of the system allows us to treat different subsets with different levels of theory. Within VASP we used it for hybrid DFT in DFT but in perspective one could develop an interface with some quantum chemistry package in order to perform actual excited states calculations. We have also encountered and discussed some issue in the current implementation of the code that will be the focus of future studies devoted to the improvement of the method. When treating molecules and extended systems adsorbed on metallic surfaces, we had to adjust one of the currently available dispersion correction schemes for DFT (DFTD2) to make it suitable to treat this systems. The resulting reparametrization, namely DFT-D2s, not only gave good results for both molecular and extended systems (*e.g.* graphene) adsorbed on the silver surface, but the applied reparametrization strategy could easily be used in the future for other transition metals. In particular, the study of the interaction

between graphene and silver and that of doped graphene and silver that we could carry out with our DFT-D2s method allowed us to understand the interplay between the effect of the dopant and that of the metal support in an interface that is of great importance as a fuel cell electrode. 2D graphene sheets and functionalized/doped systems of this type have in fact been proposed as ORR catalysts. In this thesis we have also reported on the adsorption of an oxygen molecule on these doped/interfaced systems showing a promising boost of the activity of the already efficient boron-doped graphene with the inclusion of a silver support. Remaining in the field of 2D materials, we have studied promising van der Waals heterostructures of TMDs for water splitting catalysis, investigating in detail their electronic structure. Since the presence of line or point defects in these materials is crucial to activate their reactivity, we have investigated how a Sulphur vacancy affects their electronic strucutre properties. Finally, we can see from the alignment of the bands and the separation of the contributions with respect to the layers, that an electron-hole separation will be present in these materials. In this way, they can both be used to perform the catalysis of different half reactions on the opposite sides of the heterostructure.

There is still much unexplored. We are currently working at the complete characterization of the reaction pathways of the catalytic processes (*e.g.* CO2RR, ORR, water splitting). Much can be improved on the theoretical models, using as a starting point the calculations reported in this thesis. We can add layers of complexity building towards the real system, being able to dissect the role of different components. As an example, the inclusion of the solvent contribution (where missing) as that of temperature or applied voltage could give us a picture that better resembles the conditions in which the studied materials are supposed to operate. The continuous improvement of the theoretical techniques (along with the always increasing computational power) makes possible the use of more and more realistic models, stepping towards the possibility of predicting and explaining entrirely *ab initio* the roles of the different moieties and their interplay that gives rise to the behaviour of heterogeneous functional materials.

Bibliography

[1] A. K. Padhi, K. S. Nanjundaswamy, and J. B. Goodenough. Phospho-olivines as positive-electrode materials for rechargeable lithium batteries. *Journal of The Electrochemical Society*, 144(4):1188–1194, 1997.

[2] K. Mizushima, P.C. Jones, P.J. Wiseman, and J.B. Goodenough. Li_xCoO_2 (0<x<-1): A new cathode material for batteries of high energy density. *Materials Research Bulletin*, 15(6):783 – 789, 1980.

[3] S. Pimputkar, J. S. Speck, S. P. DenBaars, and S. Nakamura. Prospects for LED lighting. *Nature hotonics*, 3(4):180, 2009.

[4] S. Lee, J. H. Kwon, S. Kwon, and K. C. Choi. A review of flexible OLEDs toward highly durable unusual displays. *IEEE Transactions on Electron Devices*, 64(5):1922–1931, 2017.

[5] E. Fortunato, P. Barquinha, and R. Martins. Oxide semiconductor thin-film transistors: A review of recent advances. *Advanced Materials*, 24(22):2945–2986, 2012.

[6] J. Safari and Z. Zarnegar. Advanced drug delivery systems: Nanotechnology of health design a review. *Journal of Saudi Chemical Society*, 18(2):85 – 99, 2014.

[7] J. Gong, K. Sumathy, Q. Qiao, and Z. Zhou. Review on dye-sensitized solar cells (DSSCs): Advanced techniques and research trends. *Renewable and Sustainable Energy Reviews*, 68:234 – 246, 2017.

[8] Z. Shi and A. H. Jayatissa. Perovskites-based solar cells: A review of recent progress, materials and processing methods. *Materials*, 11(5), 2018.

[9] J. Gong, C. Li, and M. R. Wasielewski. Advances in solar energy conversion. *Chemical Society Reviews.*, 48:1862–1864, 2019.

[10] A.V. Shah, R. Platz, and H. Keppner. Thin-film silicon solar cells: A review and selected trends. *Solar Energy Materials and Solar Cells*, 38(1):501 – 520, 1995.

[11] M. A. Green. The path to 25% silicon solar cell efficiency: History of silicon cell evolution. *Progress in Photovoltaics: Research and Applications*, 17(3):183–189, 2009.

[12] S. Dubey, N. Y. Jadhav, and B. Zakirova. Socio-economic and environmental impacts of silicon based photovoltaic (PV) technologies. *Energy Procedia*, 33:322 – 334, 2013.

[13] D. Aurbach, Y. Talyosef, B. Markovsky, E. Markevich, E. Zinigrad, L. Asraf, J. S. Gnanaraj, and H. J. Kim. Design of electrolyte solutions for Li and Li-ion batteries: a review. *Electrochimica Acta*, 50(2):247 – 254, 2004.

[14] E. A. Carter. Challenges in modeling materials properties without experimental input. *Science*, 321(5890):800–803, 2008.

[15] P. Hohenberg and W. Kohn. Inhomogeneous electron gas. *Physical Review*, 136(3B):B864, 1964.

[16] W. Kohn and L. J. Sham. Self-consistent equations including exchange and correlation effects. *Physical Review*, 140:A1133–A1138, 1965.

[17] H. S. Yu, S. L. Li, and D. G. Truhlar. Perspective: Kohn-Sham density functional theory descending a staircase. *The Journal of Chemical Physics*, 145(13):130901, 2016.

[18] E. Runge and E. K. U. Gross. Density-functional theory for time-dependent systems. *Physical Review Letters.*, 52:997–1000, 1984.

[19] M.A.L. Marques and E.K.U. Gross. Time-dependent density functional theory. *Annual Review of Physical Chemistry*, 55(1):427–455, 2004.

[20] S. Grimme. Semiempirical GGA-type density functional constructed with a long-range dispersion correction. *Journal of Computational Chemistry*, 27(15):1787–1799, 2006.

[21] S. Grimme, J. Antony, S. Ehrlich, and H. Krieg. A consistent and accurate ab initio parametrization of density functional dispersion correction (DFT-D) for the 94 elements H-Pu. *The Journal of Chemical Physics*, 132(15):154104, 2010.

[22] M. Dion, H. Rydberg, E. Schröder, D. C. Langreth, and B. I. Lundqvist. Van der Waals density functional for general geometries. *Physical Review Letters.*, 92:246401, 2004.

[23] K. Berland and P. Hyldgaard. Exchange functional that tests the robustness of the plasmon description of the van der Waals density functional. *Physical Review B*, 89:035412, 2014.

[24] K. Toyoda, I. Hamada, K. Lee, S. Yanagisawa, and Y. Morikawa. Density functional theoretical study of pentacene/noble metal interfaces with van der Waals corrections: Vacuum level shifts and electronic structures. *The Journal of Chemical Physics*, 132(13):134703, 2010.

[25] J. Klimeš and A. Michaelides. Perspective: Advances and challenges in treating van der waals dispersion forces in density functional theory. *The Journal of Chemical Physics*, 137(12):120901, 2012.

[26] K. Lee, É. D. Murray, L. Kong, B. I. Lundqvist, and D. C. Langreth. Higher-accuracy van der Waals density functional. *Physical Review B*, 82:081101, 2010.

[27] É. D. Murray, K. Lee, and D. C. Langreth. Investigation of exchange energy density functional accuracy for interacting molecules. *Journal of Chemical Theory and Computation*, 5(10):2754–2762, 2009.

[28] I. Hamada. van der Waals density functional made accurate. *Physical Review B*, 89:121103, 2014.

[29] A. Tkatchenko and M. Scheffler. Accurate molecular van der Waals interactions from ground-state electron density and free-atom reference data. *Physical Review Letters.*, 102:073005, 2009.

[30] J. Tao, H. Tang, A. Patra, P. Bhattarai, and J. P. Perdew. Modeling the physisorption of graphene on metals. *Physical Review B*, 97:165403, 2018.

[31] J. Hermann, R. A. DiStasio, and A. Tkatchenko. First-principles models for van der waals interactions in molecules and materials: Concepts, theory, and applications. *Chemical Reviews*, 117(6):4714–4758, 2017.

[32] K. Berland, V. R. Cooper, K. Lee, E. Schröder, T. Thonhauser, P. Hyldgaard, and B. I. Lundqvist. van der Waals forces in density functional theory: a review of the vdW-DF method. *Reports on Progress in Physics*, 78(6):066501, 2015.

[33] G. Román-Pérez and J. M. Soler. Efficient implementation of a van der waals density functional: Application to double-wall carbon nanotubes. *Physical Review Letters.*, 103:096102, 2009.

[34] J. P. Perdew and K. Schmidt. Jacob's ladder of density functional approximations for the exchange-correlation energy. *AIP Conference Proceedings*, 577(1):1–20, 2001.

[35] S. A. Tolba, K. M. Gameel, B. A. Ali, H. A. Almossalami, and N. K. Allam. The DFT+U: Approaches, accuracy, and applications. In Gang Yang, editor, *Density Functional Calculations*, chapter 1. IntechOpen, Rijeka, 2018.

[36] N. J. Mosey, P. Liao, and E. A. Carter. Rotationally invariant ab initio evaluation of coulomb and exchange parameters for DFT+U calculations. *The Journal of Chemical Physics*, 129(1):014103, 2008.

[37] B. G. Dick and A. W. Overhauser. Theory of the dielectric constants of alkali halide crystals. *Physical Review*, 112:90–103, 1958.

[38] J. R. Shoemaker and M. S. Gordon. SIMOMM: An integrated molecular orbital/molecular mechanics optimization scheme for surfaces. *The Journal of Physical Chemistry A*, 103(17):3245–3251, 1999.

[39] M. Karplus, M. Levitt, and A. Warshel. The Nobel prize in chemistry 2013. *Nobel Media AB 2014*, 2013.

[40] Thom Vreven and Keiji Morokuma. Chapter 3 hybrid methods: ONIOM(QM:MM) and QM/MM. volume 2 of *Annual Reports in Computational Chemistry*, pages 35 – 51. Elsevier, 2006.

[41] C. Pisani. Approach to the embedding problem in chemisorption in a self-consistent-field-molecular-orbital formalism. *Physical Review B*, 17:3143–3153, 1978.

[42] J. E. Inglesfield. A method of embedding. *Journal of Physics C: Solid State Physics*, 14(26):3795–3806, 1981.

[43] J. L. Whitten and H. Yang. Theoretical studies of surface reactions on metals. *International Journal of Quantum Chemistry*, 56(S29):41–47, 1995.

[44] N. Govind, Y. A. Wang, A. J. R. da Silva, and E. A. Carter. Accurate ab initio energetics of extended systems via explicit correlation embedded in a density functional environment. *Chemical Physics Letters*, 295(1):129 – 134, 1998.

[45] Pietro Cortona. Self-consistently determined properties of solids without band-structure calculations. *Physical Review B*, 44:8454–8458, 1991.

[46] T. Klüner, N. Govind, Y. A. Wang, and E. A. Carter. Periodic density functional embedding theory for complete active space self-consistent field and configuration interaction calculations: Ground and excited states. *The Journal of Chemical Physics*, 116(1):42–54, 2002.

[47] Patrick Huang and Emily A. Carter. Self-consistent embedding theory for locally correlated configuration interaction wave functions in condensed matter. *The Journal of Chemical Physics*, 125(8):084102, 2006.

[48] C. Huang, M. Pavone, and E. A. Carter. Quantum mechanical embedding theory based on a unique embedding potential. *The Journal of Chemical Physics*, 134(15):154110, 2011.

[49] F. Libisch, C. Huang, and E. A. Carter. Embedded correlated wavefunction schemes: Theory and applications. *Accounts of Chemical Research*, 47(9):2768–2775, 2014.

[50] G. Kresse and J. Hafner. Ab initio molecular dynamics for liquid metals. *Physical Review B*, 47:558–561, 1993.

[51] G. Kresse and J. Hafner. Ab initio molecular-dynamics simulation of the liquid-metal–amorphous-semiconductor transition in germanium. *Physical Review B*, 49:14251–14269, 1994.

[52] G. Kresse and J. Furthmüller. Efficiency of ab-initio total energy calculations for metals and semiconductors using a plane-wave basis set. *Computational Materials Science*, 6(1):15 – 50, 1996.

[53] G. Kresse and J. Furthmüller. Efficient iterative schemes for ab initio total-energy calculations using a plane-wave basis set. *Physical Review B*, 54:11169–11186, 1996.

[54] S. L. Dudarev, G. A. Botton, S. Y. Savrasov, C. J. Humphreys, and A. P. Sutton. Electron-energy-loss spectra and the structural stability of nickel oxide: An LSDA+U study. *Physical Review B*, 57:1505–1509, 1998.

[55] A. Rohrbach, J. Hafner, and G. Kresse. Electronic correlation effects in transition-metal sulfides. *Journal of Physics: Condensed Matter*, 15(6):979–996, 2003.

[56] J. Heyd, G. E. Scuseria, and M. Ernzerhof. Hybrid functionals based on a screened coulomb potential. *The Journal of Chemical Physics*, 118(18):8207–8215, 2003.

[57] J. Heyd, G. E. Scuseria, and M. Ernzerhof. Erratum: "hybrid functionals based on a screened coulomb potential" [J. Chem. Phys. 118, 8207 (2003)]. *The Journal of Chemical Physics*, 124(21):219906, 2006.

[58] C. Adamo and V. Barone. Toward reliable density functional methods without adjustable parameters: The PBE0 model. *The Journal of Chemical Physics*, 110(13):6158–6170, 1999.

[59] J. P. Perdew, K. Burke, and M. Ernzerhof. Generalized gradient approximation made simple. *Physical Review Letters.*, 77:3865–3868, 1996.

[60] J. P. Perdew, K. Burke, and M. Ernzerhof. Generalized gradient approximation made simple [Phys. Rev. Lett. 77, 3865 (1996)]. *Physical Review Letters.*, 78:1396–1396, 1997.

[61] P. E. Blöchl. Projector augmented-wave method. *Physical Review B*, 50:17953–17979, 1994.

[62] E. Schiavo, A. B. Muñoz-García, V. Barone, A. Vittadini, M. Casarin, D. Forrer, and M. Pavone. Tuning dispersion correction in DFT-D2 for metal-molecule interactions: A tailored reparameterization strategy for the adsorption of aromatic systems on Ag(111). *Chemical Physics Letters*, 693:28 – 33, 2018.

[63] M. J. Frisch, G. W. Trucks, H. B. Schlegel, G. E. Scuseria, M. A. Robb, J. R. Cheeseman, G. Scalmani, V. Barone, B. Mennucci, G. A. Petersson, H. Nakatsuji, M. Caricato, X. Li, H. P. Hratchian, A. F. Izmaylov, J. Bloino, G. Zheng, J. L. Sonnenberg, M. Hada, M. Ehara, K. Toyota, R. Fukuda, J. Hasegawa, M. Ishida, T. Nakajima, Y. Honda, O. Kitao, H. Nakai, T. Vreven, J. A. Montgomery Jr., J. E. Peralta, F. Ogliaro, M. Bearpark, J. J. Heyd, E. Brothers, K. N. Kudin, V. N. Staroverov, R. Kobayashi, J. Normand, K. Raghavachari, A. Rendell, J. C. Burant, S. S. Iyengar, J. Tomasi, M. Cossi, N. Rega, J. M. Millam, M. Klene, J. E. Knox, J. B. Cross, V. Bakken, C. Adamo, J. Jaramillo, R. Gomperts, R. E. Stratmann, O. Yazyev, A. J. Austin, R. Cammi, C. Pomelli, J. W. Ochterski, R. L. Martin, K. Morokuma, V. G. Zakrzewski, G. A. Voth, P. Salvador, J. J. Dannenberg, S. Dapprich, A. D. Daniels, Ö. Farkas, J. B. Foresman, J. V. Ortiz, J. Cioslowski, and D. J. Fox. •. *Gaussian 09 (Gaussian, Inc., Wallingford CT, 2009).*, •.

[64] United Nations Framework Convention on Climate Change. Kyoto Protocol. *https://unfccc.int/kyoto_protocol*, 1992.

[65] United Nations Framework Convention on Climate Change. The Doha amendment. *https://unfccc.int/process/the-kyoto-protocol/the-doha-amendment*, 2012.

[66] United Nations Framework Convention on Climate Change. The Paris agreement. *https://unfccc.int/process-and-meetings/the-paris-agreement/the-paris-agreement*, 2015.

[67] A. Hagfeldt, G. Boschloo, L. Sun, L. Kloo, and H. Pettersson. Dye-sensitized solar cells. *Chemical Reviews*, 110(11):6595–6663, 2010.

[68] D. Turney and V. Fthenakis. Environmental impacts from the installation and operation of large-scale solar power plants. *Renewable and Sustainable Energy Reviews*, 15(6):3261 – 3270, 2011.

[69] M. Freitag, J. Teuscher, Y. Saygili, X. Zhang, F. Giordano, P. Liska, J. Hua, S. M. Zakeeruddin, J.-E. Moser, M. Grätzel, and A. Hagfeldt. Dye-sensitized solar cells for efficient power generation under ambient lighting. *Nature Photonics*, 11(6):372–378, 2017.

[70] S. Yoon, S. Tak, J. Kim, Y. Jun, K. Kang, and J. Park. Application of transparent dye-sensitized solar cells to building integrated photovoltaic systems. *Building and Environment*, 46(10):1899 – 1904, 2011.

[71] I. Benesperi, H. Michaels, and M. Freitag. The researcher's guide to solid-state dye-sensitized solar cells. *Journal of Materials Chemistry C*, 6:11903–11942, 2018.

[72] M. A. Green. Third generation photovoltaics: Ultra-high conversion efficiency at low cost. *Progress in Photovoltaics: Research and Applications*, 9(2):123–135, 2001.

[73] S. Kurtz, N. Haegel, R. Sinton, and R. Margolis. A new era for solar. *Nature Photonics*, 11(1):3–5, 2017.

[74] B. O'Regan and M. Grätzel. A low-cost, high-efficiency solar cell based on dye-sensitized colloidal TiO_2 films. *Nature*, 353(6346):737–740, 1991.

[75] J. He, H. Lindström, A. Hagfeldt, and S.-E. Lindquist. Dye-sensitized nanostructured tandem cell-first demonstrated cell with a dye-sensitized photocathode. *Solar Energy Materials and Solar Cells*, 62(3):265 – 273, 2000.

[76] A. Nakasa, H. Usami, S. Sumikura, S. Hasegawa, T. Koyama, and E. Suzuki. A high voltage dye-sensitized solar cell using a nanoporous NiO photocathode. *Chemistry Letters*, 34(4):500–501, 2005.

[77] M. S. Prévot and K. Sivula. Photoelectrochemical tandem cells for solar water splitting. *The Journal of Physical Chemistry C*, 117(35):17879–17893, 2013.

[78] I. R. Perera, T. Daeneke, S. Makuta, Z. Yu, Y. Tachibana, A. Mishra, P. Bäuerle, C. A. Ohlin, U. Bach, and L. Spiccia. Application of the tris(acetylacetonato)iron(iii)/(ii) redox couple in p-type dye-sensitized solar cells. *Angewandte Chemie International Edition*, 54(12):3758–3762, 2015.

[79] I. Sullivan, B. Zoellner, and P. A. Maggard. Copper(I)-based p-type oxides for photoelectrochemical and photovoltaic solar energy conversion. *Chemistry of Materials*, 28(17):5999–6016, 2016.

[80] A. Morandeira, G. Boschloo, A. Hagfeldt, and L. Hammarström. Photoinduced ultrafast dynamics of coumarin 343 sensitized p-type-nanostructured NiO films. *The Journal of Physical Chemistry B*, 109(41):19403–19410, 2005.

[81] F. Odobel and Y. Pellegrin. Recent advances in the sensitization of wide-band-gap nanostructured p-type semiconductors. photovoltaic and photocatalytic applications. *The Journal of Physical Chemistry Letters*, 4(15):2551–2564, 2013.

[82] S. Mori, S. Fukuda, S. Sumikura, Y. Takeda, Y. Tamaki, E. Suzuki, and T. Abe. Charge-transfer processes in dye-sensitized NiO solar cells. *The Journal of Physical Chemistry C*, 112(41):16134–16139, 2008.

[83] A. Renaud, B. Chavillon, L. Le Pleux, Y. Pellegrin, E. Blart, M. Boujtita, T. Pauporté, L. Cario, S. Jobic, and F. Odobel. $CuGaO_2$: a promising alternative for NiO in p-type dye solar cells. *Journal of Materials Chemistry.*, 22:14353–14356, 2012.

[84] M. F. Iozzi, P. Vajeeston, R. Vidya, P. Ravindran, and H. Fjellvåg. Structural and electronic properties of transparent conducting delafossite: a comparison between the $AgBO_2$ and $CuBO_2$ families (B = Al, Ga, In and Sc, Y). *RSC Advances*, 5:1366–1377, 2015.

[85] B. Das, A. Renaud, A. M. Volosin, L. Yu, N. Newman, and D.-K. Seo. Nanoporous delafossite $CuAlO_2$ from inorganic/polymer double gels: A desirable high-surface-area p-type transparent electrode material. *Inorganic Chemistry*, 54(3):1100–1108, 2015.

[86] M. Yu, G. Natu, Z. Ji, and Y. Wu. p-type dye-sensitized solar cells based on delafossite $CuGaO_2$ nanoplates with saturation photovoltages exceeding 460 mV. *The Journal of Physical Chemistry Letters*, 3(9):1074–1078, 2012.

[87] M. Yu, T. I. Draskovic, and Y. Wu. Cu(i)-based delafossite compounds as photocathodes in p-type dye-sensitized solar cells. *Physical Chemistry Chemical Physics.*, 16:5026–5033, 2014.

[88] Y. Pellegrin, L. Le Pleux, E. Blart, A. Renaud, B. Chavillon, N. Szuwarski, M. Boujtita, L. Cario, S. Jobic, D. Jacquemin, and F. Odobel. Ruthenium polypyridine complexes as sensitizers in NiO based p-type dye-sensitized solar cells: Effects of the anchoring groups. *Journal of Photochemistry and Photobiology A: Chemistry*, 219(2):235 – 242, 2011.

[89] Y. M. Klein, N. Marinakis, E. C. Constable, and C. E. Housecroft. A phosphonic acid anchoring analogue of the sensitizer P1 for p-type dye-sensitized solar cells. *Crystals*, 8(10), 2018.

[90] F. De Angelis, S. Fantacci, and R. Gebauer. Simulating dye-sensitized tio2 heterointerfaces in explicit solvent: Absorption spectra, energy levels, and dye desorption. *The Journal of Physical Chemistry Letters*, 2(7):813–817, 2011.

[91] S. Galliano, F. Bella, C. Gerbaldi, M. Falco, G. Viscardi, M. Grätzel, and C. Barolo. Photoanode/electrolyte interface stability in aqueous dye-sensitized solar cells. *Energy Technology*, 5(2):300–311, 2017.

[92] B. Kumar, M. Llorente, J. Froehlich, T. Dang, A. Sathrum, and C. P. Kubiak. Photochemical and photoelectrochemical reduction of CO_2. *Annual Review of Physical Chemistry*, 63(1):541–569, 2012.

[93] J. L. White, M. F. Baruch, J. E. Pander, Y. Hu, I. C. Fortmeyer, J. E. Park, T. Zhang, K. Liao, J. Gu, Y. Yan, T. W. Shaw, E. Abelev, and A. B. Bocarsly. Light-driven heterogeneous reduction of carbon dioxide: Photocatalysts and photoelectrodes. *Chemical Reviews*, 115(23):12888–12935, 2015.

[94] K. Li, X. An, K. H. Park, M. Khraisheh, and J. Tang. A critical review of CO_2 photoconversion: Catalysts and reactors. *Catalysis Today*, 224:3 – 12, 2014.

[95] K. Li, B. Peng, and T. Peng. Recent advances in heterogeneous photocatalytic CO_2 conversion to solar fuels. *ACS Catalysis*, 6(11):7485–7527, 2016.

[96] A. B. Vidal, L. Feria, J. Evans, Y. Takahashi, P. Liu, K. Nakamura, F. Illas, and J. A. Rodriguez. CO_2 activation and methanol synthesis on novel Au/TiC and Cu/TiC catalysts. *The Journal of Physical Chemistry Letters*, 3(16):2275–2280, 2012.

[97] J. A. Rodriguez, J. Evans, L. Feria, A. B. Vidal, P. Liu, K. Nakamura, and F. Illas. CO_2 hydrogenation on Au/TiC, Cu/TiC, and Ni/TiC catalysts: Production of CO, methanol, and methane. *Journal of Catalysis*, 307:162 – 169, 2013.

[98] H. Ooka, M. C. Figueiredo, and M. T. M. Koper. Competition between hydrogen evolution and carbon dioxide reduction on copper electrodes in mildly acidic media. *Langmuir*, 33(37):9307–9313, 2017.

[99] Y. Hori, K. Kikuchi, and S. Suzuki. Production of CO and CH_4 in electrochemical reduction of CO_2 at metal electrodes in aqueous hydrogencarbonate solution. *Chemistry Letters*, 14(11):1695–1698, 1985.

[100] S. Posada-Pérez, P. J. Ramírez, R. A. Gutiérrez, D. J. Stacchiola, F. Viñes, Ping Liu, F. Illas, and J. A. Rodriguez. The conversion of co_2 to methanol on orthorhombic β-mo_2c and cu/β-mo_2c catalysts: mechanism for admetal induced change in the selectivity and activity. *Catal. Sci. Technol.*, 6:6766–6777, 2016.

[101] S. Posada-Pérez, P. J. Ramírez, J. Evans, F. Viñes, P. Liu, F. Illas, and J. A. Rodriguez. Highly active Au/δ-MoC and Cu/δ-MoC catalysts for the conversion of CO_2: The metal/C ratio as a key factor defining activity, selectivity, and stability. *Journal of the American Chemical Society*, 138(26):8269–8278, 2016.

[102] J. Graciani, K. Mudiyanselage, F. Xu, A. E. Baber, J. Evans, S. D. Senanayake, D. J. Stacchiola, P. Liu, J. Hrbek, J. F. Sanz, and J. A. Rodriguez. Highly active copper-ceria and copper-ceria-titania catalysts for methanol synthesis from CO_2. *Science*, 345(6196):546–550, 2014.

[103] M. Behrens, F. Studt, I. Kasatkin, S. Kühl, M. Hävecker, F. Abild-Pedersen, S. Zander, F. Girgsdies, P. Kurr, B. L. Kniep, M. Tovar, R. W. Fischer, J. K. Nørskov, and R. Schlögl. The active site of methanol synthesis over $Cu/ZnO/Al_2O_3$ industrial catalysts. *Science*, 336(6083):893–897, 2012.

[104] C. Janáky, D. Hursán, B. Endrődi, W. Chanmanee, D. Roy, D. Liu, N. R. de Tacconi, B. H. Dennis, and K. Rajeshwar. Electro- and photoreduction of carbon dioxide: The twain shall meet at copper oxide/copper interfaces. *ACS Energy Letters*, 1(2):332–338, 2016.

[105] A. K. Mishra, A. Roldan, and N. H. de Leeuw. CuO surfaces and CO_2 activation: A dispersion-corrected DFT+U study. *The Journal of Physical Chemistry C*, 120(4):2198–2214, 2016.

[106] L. I. Bendavid and E. A. Carter. CO_2 adsorption on $Cu_2O(111)$: A DFT+U and DFT-D study. *The Journal of Physical Chemistry C*, 117(49):26048–26059, 2013.

[107] F. Studt, M. Behrens, E. L. Kunkes, N. Thomas, S. Zander, A. Tarasov, J. Schumann, E. Frei, J. B. Varley, F. Abild-Pedersen, J. K. Nørskov, and

R. Schlögl. The mechanism of CO and CO_2 hydrogenation to methanol over cu-based catalysts. *ChemCatChem*, 7(7):1105–1111, 2015.

[108] G. Ghadimkhani, N. R. de Tacconi, W. Chanmanee, C. Janaky, and K. Rajeshwar. Efficient solar photoelectrosynthesis of methanol from carbon dioxide using hybrid CuO–Cu_2O semiconductor nanorod arrays. *Chem. Commun.*, 49:1297–1299, 2013.

[109] K. Rajeshwar, N. R. de Tacconi, G. Ghadimkhani, W. Chanmanee, and C. Janáky. Tailoring copper oxide semiconductor nanorod arrays for photoelectrochemical reduction of carbon dioxide to methanol. *ChemPhysChem*, 14(10):2251–2259, 2013.

[110] H. Kawazoe, M. Yasukawa, H. Hyodo, M. Kurita, H. Yanagi, and H. Hosono. P-type electrical conduction in transparent thin films of $CuAlO_2$. *Nature*, 389(6654):939–942, 1997.

[111] M. A. Marquardt, N. A. Ashmore, and D. P. Cann. Crystal chemistry and electrical properties of the delafossite structure. *Thin Solid Films*, 496(1):146 – 156, 2006.

[112] T. Okuda, N. Jufuku, S. Hidaka, and N. Terada. Magnetic, transport, and thermoelectric properties of the delafossite oxides $CuCr_{1-x}Mg_xO_2$ ($0 \leq x \leq 0.04$). *Physical Review B*, 72:144403, 2005.

[113] V. R. Galakhov, A. I. Poteryaev, E. Z. Kurmaev, V. I. Anisimov, St. Bartkowski, M. Neumann, Z. W. Lu, B. M. Klein, and Tong-Rong Zhao. Valence-band spectra and electronic structure of $cufeo_2$. *Physical Review B*, 56:4584–4591, 1997.

[114] M. S. Prévot, X. A. Jeanbourquin, W. S. Bourée, F. Abdi, D. Friedrich, R. van de Krol, N. Guijarro, F. Le Formal, and K. Sivula. Evaluating charge carrier transport and surface states in $CuFeO_2$ photocathodes. *Chemistry of Materials*, 29(11):4952–4962, 2017.

[115] C. G. Read, Y. Park, and K.-S. Choi. Electrochemical synthesis of p-type $CuFeO_2$ electrodes for use in a photoelectrochemical cell. *The Journal of Physical Chemistry Letters*, 3(14):1872–1876, 2012.

[116] N. Zhang, R. Long, C. Gao, and Y. Xiong. Recent progress on advanced design for photoelectrochemical reduction of CO_2 to fuels. *Science China Materials*, 61(6):771–805, 2018.

[117] J. Gu, A. Wuttig, J. W. Krizan, Y. Hu, Z. M. Detweiler, R. J. Cava, and A. B. Bocarsly. Mg-doped $CuFeO_2$ photocathodes for photoelectrochemical reduction of carbon dioxide. *The Journal of Physical Chemistry C*, 117(24):12415–12422, 2013.

[118] A. Wuttig, J. W. Krizan, J. Gu, J. J. Frick, R. J. Cava, and A. B. Bocarsly. The effect of Mg-doping and Cu nonstoichiometry on the photoelectrochemical response of $CuFeO_2$. *Journal of Materials Chemistry. A*, 5:165–171, 2017.

[119] U. Kang, S. Kyu Choi, D. J. Ham, S. M. Ji, W. Choi, D. S. Han, A. A.-W., and H. Park. Photosynthesis of formate from CO_2 and water at 1efficiency via copper iron oxide catalysis. *Energy and Environmental Science.*, 8:2638–2643, 2015.

[120] X. Yang, E. A. Fugate, Y. Mueanngern, and L. R. Baker. Photoelectrochemical CO_2 reduction to acetate on iron–copper oxide catalysts. *ACS Catalysis*, 7(1):177–180, 2017.

[121] S. H. Yoon, U. Kang, H. Park, A. Abdel-Wahab, and D. S. Han. Computational density functional theory study on the selective conversion of CO_2 to formate on homogeneously and heterogeneously mixed $CuFeO_2$ and CuO surfaces. *Catalysis Today*, 335:345 – 353, 2019.

[122] L. Li, R. Zhang, J. Vinson, E. L. Shirley, J. P. Greeley, J. R. Guest, and M. K. Y. Chan. Imaging catalytic activation of CO_2 on Cu_2O (110): A first-principles study. *Chemistry of Materials*, 30(6):1912–1923, 2018.

[123] A. Carella, R. Centore, F. Borbone, M. Toscanesi, M. Trifuoggi, F. Bella, C. Gerbaldi, S. Galliano, E. Schiavo, A. Massaro, A. B. Muñoz-García, and M. Pavone. Tuning optical and electronic properties in novel carbazole photosensitizers for p-type dye-sensitized solar cells. *Electrochimica Acta*, 292:805 – 816, 2018.

[124] T. Le Bahers, C. Adamo, and I. Ciofini. A qualitative index of spatial extent in charge-transfer excitations. *Journal of Chemical Theory and Computation*, 7(8):2498–2506, 2011.

[125] A. B. Muñoz-García and M. Pavone. Structure and energy level alignment at the dye–electrode interface in p-type DSSCs: new hints on the role of anchoring modes from ab initio calculations. *Physical Chemistry Chemical Physics.*, 17:12238–12246, 2015.

[126] J. N. Clifford, E. Palomares, M. K. Nazeeruddin, M. Grätzel, J. Nelson, X. Li, N. J. Long, and J. R. Durrant. Molecular control of recombination dynamics in dye-sensitized nanocrystalline TiO_2 films: Free energy vs distance dependence. *Journal of the American Chemical Society*, 126(16):5225–5233, 2004.

[127] J. Z. Zhang, J. Zhang, H. B. Li, Y. Wu, H. L. Xu, M. Zhang, Y. Geng, and Z. M. Su. Modulation on charge recombination and light harvesting toward high-performance benzothiadiazole-based sensitizers in dye-sensitized solar cells: A theoretical investigation. *Journal of Power Sources*, 267:300 – 308, 2014.

[128] J. Feng, Y. Jiao, W. Ma, M. K. Nazeeruddin, M. Grätzel, and S. Meng. First principles design of dye molecules with ullazine donor for dye sensitized solar cells. *The Journal of Physical Chemistry C*, 117(8):3772–3778, 2013.

[129] S. Karamshuk, S. Caramori, N. Manfredi, M. Salamone, R. Ruffo, S. Carli, C. A. Bignozzi, and A. Abbotto. Molecular level factors affecting the efficiency of organic chromophores for p-type dye sensitized solar cells. *Energies*, 9(1), 2016.

[130] M. Bonomo, A. Carella, R. Centore, A. Di Carlo, and D. Dini. First examples of pyran based colorants as sensitizing agents of p-type dye-sensitized solar cells. *Journal of The Electrochemical Society*, 164(13):F1412–F1418, 2017.

[131] P. Naik, A. Planchat, Y. Pellegrin, F. Odobel, and A. V. Adhikari. Exploring the application of new carbazole based dyes as effective p-type photosensitizers in dye-sensitized solar cells. *Solar Energy*, 157:1064 – 1073, 2017.

[132] T. Yanai, D. P. Tew, and N. C. Handy. A new hybrid exchange–correlation functional using the Coulomb-attenuating method (CAM-B3LYP). *Chemical Physics Letters*, 393(1):51 – 57, 2004.

[133] N. Godbout, D. R. Salahub, J. Andzelm, and E. Wimmer. Optimization of gaussian-type basis sets for local spin density functional calculations. part I. boron through neon, optimization technique and validation. *Canadian Journal of Chemistry*, 70(2):560–571, 1992.

[134] N. Alidoust, M. C. Toroker, J. A. Keith, and E. A. Carter. Significant reduction in NiO band gap upon formation of $Li_xNi_{1-x}O$ alloys: Applications to solar energy conversion. *ChemSusChem*, 7(1):195–201, 2014.

[135] N. Alidoust, M. C. Toroker, and E. A. Carter. Revisiting photoemission and inverse photoemission spectra of nickel oxide from first principles: Implications for solar energy conversion. *The Journal of Physical Chemistry B*, 118(28):7963–7971, 2014.

[136] N. J. Mosey and E. A. Carter. Ab initio evaluation of coulomb and exchange parameters for DFT + U calculations. *Physical Review B*, 76:155123, 2007.

[137] H. Kawazoe, M. Yasukawa, H. Hyodo, M. Kurita, H. Yanagi, and H. Hosono. P-type electrical conduction in transparent thin films of $CuAlO_2$. *Nature*, 389(6654):939–942, 1997.

[138] D. O. Scanlon and G. W. Watson. Conductivity limits in $CuAlO_2$ from screened-hybrid density functional theory. *The Journal of Physical Chemistry Letters*, 1(21):3195–3199, 2010.

[139] B. Das, A. Renaud, A. M. Volosin, L. Yu, N. Newman, and D. K. Seo. Nanoporous delafossite $CuAlO_2$ from inorganic/polymer double gels: A desirable high-surface-area p-type transparent electrode material. *Inorganic Chemistry*, 54(3):1100–1108, 2015.

[140] A. Renaud, L. Cario, P. Deniard, E. Gautron, X. Rocquefelte, Y. Pellegrin, E. Blart, F. Odobel, and S. Jobic. Impact of Mg doping on performances of $CuGaO_2$ based p-type dye-sensitized solar cells. *The Journal of Physical Chemistry C*, 118(1):54–59, 2014.

[141] C. Ruttanapun. Optical and electronic properties of delafossite $CuBO_2$ p-type transparent conducting oxide. *Journal of Applied Physics*, 114(11):113108, 2013.

[142] D. O. Scanlon, A. Walsh, B. J. Morgan, G. W. Watson, D. J. Payne, and R. G. Egdell. Effect of Cr substitution on the electronic structure of $\mathrm{cual}_{1-x}\mathrm{cr}_x\mathrm{o}_2$. *Physical Review B*, 79:035101, 2009.

[143] Haifeng Jiang, Xiancai Wang, Xueping Zang, Weifeng Wu, Shunping Sun, Chao Xiong, Weiwei Yin, Chuanyou Gui, and Xuebin Zhu. Electronic properties of bivalent cations (Be, Mg and Ca) substitution for Al in delafossite $CuAlO_2$ semiconductor by first-principles calculations. *Journal of Alloys and Compounds*, 553:245 – 252, 2013.

[144] M. C. Toroker, D. K. Kanan, N. Alidoust, L. Y. Isseroff, P. Liao, and E. A. Carter. First principles scheme to evaluate band edge positions in potential transition metal oxide photocatalysts and photoelectrodes. *Physical Chemistry Chemical Physics.*, 13:16644–16654, 2011.

[145] V. Jayalakshmi, R. Murugan, and B. Palanivel. Electronic and structural properties of $CuMO_2$ (M = Al, Ga, In). *Journal of Alloys and Compounds*, 388(1):19 – 22, 2005.

[146] D. O. Scanlon, A. Walsh, and G. W. Watson. Understanding the p-type conduction properties of the transparent conducting oxide $CuBO_2$: A density functional theory analysis. *Chemistry of Materials*, 21(19):4568–4576, 2009.

[147] L. Y. Isseroff and E. A. Carter. Importance of reference hamiltonians containing exact exchange for accurate one-shot *gw* calculations of Cu_2O. *Physical Review B*, 85:235142, 2012.

[148] E. Schiavo, C. Latouche, V. Barone, O. Crescenzi, A. B. Muñoz-García, and M. Pavone. An ab initio study of Cu-based delafossites as an alternative to nickel oxide in photocathodes: effects of Mg-doping and surface electronic features. *Physical Chemistry Chemical Physics.*, 20:14082–14089, 2018.

[149] R. D. Shannon. Revised effective ionic radii and systematic studies of interatomic distances in halides and chalcogenides. *Acta Crystallographica Section A*, 32(5):751–767, 1976.

[150] H. Yanagi, S. I. Inoue, K. Ueda, H. Kawazoe, H. Hosono, and N. Hamada. Electronic structure and optoelectronic properties of transparent p-type conducting $CuAlO_2$. *Journal of Applied Physics*, 88(7):4159–4163, 2000.

[151] K. Ueda, T. Hase, H. Yanagi, H. Kawazoe, H. Hosono, H. Ohta, M. Orita, and M. Hirano. Epitaxial growth of transparent p-type conducting $CuGaO_2$ thin films on sapphire (001) substrates by pulsed laser deposition. *Journal of Applied Physics*, 89(3):1790–1793, 2001.

[152] H. Yanagi, T. Hase, S. Ibuki, K. Ueda, and H. Hosono. Bipolarity in electrical conduction of transparent oxide semiconductor $CuInO_2$ with delafossite structure. *Applied Physics Letters*, 78(11):1583–1585, 2001.

[153] X. Nie, S.-H. Wei, and S. B. Zhang. Bipolar doping and band-gap anomalies in delafossite transparent conductive oxides. *Physical Review Letters.*, 88:066405, 2002.

[154] M. Pavone, A. M. Ritzmann, and E. A. Carter. Quantum-mechanics-based design principles for solid oxide fuel cell cathode materials. *Energy and Environmental Science.*, 4:4933–4937, 2011.

[155] W. Kutzelnigg. Atoms in molecules. a quantum theory. (Reihe: International Series of Monographs on Chemistry, Vol. 22.) Von R.F.W. Bader.

Clarendon Press, Oxford, 1990. – ISBN 0-19-855168-1. *Angewandte Chemie*, 104(10):1423–1423, 1992.

[156] R. Srinivasan, B. Chavillon, C. Doussier-Brochard, L. Cario, M. Paris, E. Gautron, P. Deniard, F. Odobel, and S. Jobic. Tuning the size and color of the p-type wide band gap delafossite semiconductor $CuGaO_2$ with ethylene glycol assisted hydrothermal synthesis. *Journal of Materials Chemistry.*, 18:5647–5653, 2008.

[157] N. Ishizawa, T. Miyata, I. Minato, F. Marumo, and S. Iwai. A structural investigation of α-Al_2O_3 at 2170 K. *Acta Crystallographica Section B*, 36(2):228–230, 1980.

[158] S. Geller. Crystal structure of $\beta - Ga_2O_3$. *The Journal of Chemical Physics*, 33(3):676–684, 1960.

[159] S. Sasaki, K. Fujino, Y. Tak, and E. Uchi. X-ray determination of electron-density distributions in oxides, MgO, MnO, CoO, and NiO, and atomic scattering factors of their constituent atoms. *Proceedings of the Japan Academy, Series B*, 55(2):43–48, 1979.

[160] J. R. Winkler and H. B. Gray. *Electronic Structures of Oxo-Metal Ions*, pages 17–28. Springer Berlin Heidelberg, Berlin, Heidelberg, 2012.

[161] J. Preat, A. Hagfeldt, and E. A. Perpète. Investigation of the photoinduced electron injection processes for p-type triphenylamine-sensitized solar cells. *Energy and Environmental Science.*, 4:4537–4549, 2011.

[162] J. Cong, D. Kinschel, Q. Daniel, M. Safdari, E. Gabrielsson, H. Chen, P. H. Svensson, L. Sun, and L. Kloo. Bis(1,1-bis(2-pyridyl)ethane)copper(i/ii) as an efficient redox couple for liquid dye-sensitized solar cells. *Journal of Materials Chemistry. A*, 4:14550–14554, 2016.

[163] S. M. Feldt, E. A. Gibson, E. Gabrielsson, L. Sun, G. Boschloo, and A. Hagfeldt. Design of organic dyes and cobalt polypyridine redox mediators for high-efficiency dye-sensitized solar cells. *Journal of the American Chemical Society*, 132(46):16714–16724, 2010.

[164] G. Boschloo and A. Hagfeldt. Characteristics of the iodide/triiodide redox mediator in dye-sensitized solar cells. *Accounts of Chemical Research*, 42(11):1819–1826, 2009.

[165] Y. R. Luo. *Comprehensive Handbook of Chemical Bond Energies*. •, 2007.

[166] H. Metiu, S. Chrétien, Z. Hu, B. Li, and X. Sun. Chemistry of lewis acid–base pairs on oxide surfaces. *The Journal of Physical Chemistry C*, 116(19):10439–10450, 2012.

[167] M. D'Arienzo, L. Gamba, F. Morazzoni, U. Cosentino, C. Greco, M. Lasagni, D. Pitea, G. Moro, C. Cepek, V. Butera, E. Sicilia, N. Russo, A. B. Muñoz-García, and M. Pavone. Experimental and theoretical investigation on the catalytic generation of environmentally persistent free radicals from benzene. *The Journal of Physical Chemistry C*, 121(17):9381–9393, 2017.

[168] H. J. Monkhorst and J. D. Pack. Special points for brillouin-zone integrations. *Physical Review B*, 13:5188–5192, 1976.

[169] C. T. Crespo. Potentiality of $CuFeO_2$-delafossite as a solar energy converter. *Solar Energy*, 163:162 – 166, 2018.

[170] F.A. Benko and F.P. Koffyberg. Opto-electronic properties of p- and n-type delafossite, $CuFeO_2$. *Journal of Physics and Chemistry of Solids*, 48(5):431 – 434, 1987.

[171] San-Dong Guo. X-ray emission spectra and gaps of $CuFeO_2$ with the modified Becke–Johnson potential. *Journal of Magnetism and Magnetic Materials*, 377:226 – 228, 2015.

[172] Y. Meng, X. W. Liu, C. F. Huo, W. P. Guo, D. B. Cao, Q. Peng, A. Dearden, X. Gonze, Y. Yang, J. Wang, H. Jiao, Y. Li, and X. D. Wen. When density functional approximations meet iron oxides. *Journal of Chemical Theory and Computation*, 12(10):5132–5144, 2016.

[173] W. Pipornpong, R. Wanbayor, and V. Ruangpornvisuti. Adsorption CO_2 on the perfect and oxygen vacancy defect surfaces of anatase TiO_2 and its

photocatalytic mechanism of conversion to CO. *Applied Surface Science*, 257(24):10322 – 10328, 2011.

[174] G. Preda, G. Pacchioni, M. Chiesa, and E. Giamello. Formation of CO_2-radical anions from CO_2 adsorption on an electron-rich MgO surface: A combined ab initio and pulse EPR study. *The Journal of Physical Chemistry C*, 112(49):19568–19576, 2008.

[175] R. N. Compton, P. W. Reinhardt, and C. D. Cooper. Collisional ionization of Na, K, and Cs by CO_2, COS, and CS_2: Molecular electron affinities. *The Journal of Chemical Physics*, 63(9):3821–3827, 1975.

[176] K. Yu, F. Libisch, and E. A. Carter. Implementation of density functional embedding theory within the projector-augmented-wave method and applications to semiconductor defect states. *The Journal of Chemical Physics*, 143(10):102806, 2015.

[177] C. Huang, M. Pavone, and E. A. Carter. Quantum mechanical embedding theory based on a unique embedding potential. *The Journal of Chemical Physics*, 134(15):154110, 2011.

[178] Q. Wu and W. Yang. A direct optimization method for calculating density functionals and exchange–correlation potentials from electron densities. *The Journal of Chemical Physics*, 118(6):2498–2509, 2003.

[179] A. Morandeira, G. Boschloo, A. Hagfeldt, and L. Hammarström. Coumarin 343-NiO films as nanostructured photocathodes in dye-sensitized solar cells: Ultrafast electron transfer, effect of the I_3^-/I^- redox couple and mechanism of photocurrent generation. *The Journal of Physical Chemistry C*, 112(25):9530–9537, 2008.

[180] K. Mathew, R. Sundararaman, K. Letchworth-Weaver, T. A. Arias, and R. G. Hennig. Implicit solvation model for density-functional study of nanocrystal surfaces and reaction pathways. *The Journal of Chemical Physics*, 140(8):084106, 2014.

[181] E. Zaremba and W. Kohn. Theory of helium adsorption on simple and noble-metal surfaces. *Physical Review B*, 15:1769–1781, 1977.

[182] A. Szabo and N. S. Ostlund. *Modern Quantum Chemistry: Introduction to Advanced Electronic Structure Theory.* Dover Publications, Inc., Mineola, first edition, 1996.

[183] J. Antony and S. Grimme. Density functional theory including dispersion corrections for intermolecular interactions in a large benchmark set of biologically relevant molecules. *Physical Chemistry Chemical Physics.*, 8:5287–5293, 2006.

[184] V. Barone, M. Casarin, D. Forrer, M. Pavone, M. Sambi, and A. Vittadini. Role and effective treatment of dispersive forces in materials: Polyethylene and graphite crystals as test cases. *Journal of Computational Chemistry*, 30(6):934–939, 2009.

[185] R. Caputo, B. P. Prascher, V. Staemmler, P. S. Bagus, and C. Wöll. Adsorption of benzene on coinage metals: A theoretical analysis using wavefunction-based methods. *The Journal of Physical Chemistry A*, 111(49):12778–12784, 2007.

[186] P. S. Bagus, K. Hermann, and C. Wöll. The interaction of C_6H_6 and C_6H_{12} with noble metal surfaces: Electronic level alignment and the origin of the interface dipole. *The Journal of Chemical Physics*, 123(18):184109, 2005.

[187] G. Witte, S. Lukas, P. S. Bagus, and Ch. Wöll. Vacuum level alignment at organic/metal junctions: "cushion" effect and the interface dipole. *Applied Physics Letters*, 87(26):263502, 2005.

[188] M. P. Andersson. Density functional theory with modified dispersion correction for metals applied to molecular adsorption on Pt(111). *Physical Chemistry Chemical Physics.*, 18:19118–19122, 2016.

[189] L. Zoppi, A. Garcia, and K. K. Baldridge. Theoretical investigation of the binding process of corannulene on a Cu(111) surface. *The Journal of Physical Chemistry A*, 114(33):8864–8872, 2010.

[190] K. H. Frank, P. Yannoulis, R. Dudde, and E. E. Koch. Unoccupied molecular orbitals of aromatic hydrocarbons adsorbed on Ag(111). *The Journal of Chemical Physics*, 89(12):7569–7576, 1988.

[191] K. Tonigold and A. Groß. Adsorption of small aromatic molecules on the (111) surfaces of noble metals: A density functional theory study with semiempirical corrections for dispersion effects. *The Journal of Chemical Physics*, 132(22):224701, 2010.

[192] S. F. Boys and F. Bernardi. The calculation of small molecular interactions by the differences of separate total energies. some procedures with reduced errors. *Molecular Physics*, 19(4):553–566, 1970.

[193] K. S. Novoselov, A. K. Geim, S. V. Morozov, D. Jiang, Y. Zhang, S. V. Dubonos, I. V. Grigorieva, and A. A. Firsov. Electric field effect in atomically thin carbon films. *Science*, 306(5696):666–669, 2004.

[194] Y. M. Lin, C. Dimitrakopoulos, K. A. Jenkins, D. B. Farmer, H. Y. Chiu, A. Grill, and P. Avouris. 100-GHz transistors from wafer-scale epitaxial graphene. *Science*, 327(5966):662–662, 2010.

[195] M. Liu, X. Yin, E. Ulin-Avila, B. Geng, T. Zentgraf, L. Ju, F. Wang, and X. Zhang. A graphene-based broadband optical modulator. *Nature*, 474(7349):64, 2011.

[196] Y. Zhu, S. Murali, M. D. Stoller, K. J. Ganesh, W. Cai, P. J. Ferreira, A. Pirkle, R. M. Wallace, K. A. Cychosz, M. Thommes, D. Su, E. A. Stach, and R. S. Ruoff. Carbon-based supercapacitors produced by activation of graphene. *Science*, 332(6037):1537–1541, 2011.

[197] K. S. Kim, Y. Zhao, H. Jang, S. Y. Lee, J. Min Kim, K. S. Kim, J. H. Ahn, P. Kim, J. Y. Choi, and B. H. Hong. Large-scale pattern growth of graphene films for stretchable transparent electrodes. *Nature*, 457(7230):706, 2009.

[198] M. Xu, D. Fujita, and N. Hanagata. Perspectives and challenges of emerging single-molecule DNA sequencing technologies. *Small*, 5(23):2638–2649, 2009.

[199] J. Liu, L. Cui, and D. Losic. Graphene and graphene oxide as new nanocarriers for drug delivery applications. *Acta Biomaterialia*, 9(12):9243 – 9257, 2013.

[200] S. P. Lonkar and A. A. Abdala. Applications of graphene in catalysis. *Journal of Thermodyamics and Catalysis*, 5(132):1–132, 2014.

[201] M. Xu, T. Liang, M. Shi, and H. Chen. Graphene-like two-dimensional materials. *Chemical Reviews*, 113(5):3766–3798, 2013.

[202] D. Higgins, P. Zamani, A. Yu, and Z. Chen. The application of graphene and its composites in oxygen reduction electrocatalysis: a perspective and review of recent progress. *Energy and Environmental Science.*, 9:357–390, 2016.

[203] J. Duan, S. Chen, M. Jaroniec, and S. Z. Qiao. Heteroatom-doped graphene-based materials for energy-relevant electrocatalytic processes. *ACS Catalysis*, 5(9):5207–5234, 2015.

[204] K. Gong, F. Du, Z. Xia, M. Durstock, and L. Dai. Nitrogen-doped carbon nanotube arrays with high electrocatalytic activity for oxygen reduction. *Science*, 323(5915):760–764, 2009.

[205] T. Xing, Y. Zheng, L. H. Li, B. C. C. Cowie, D. Gunzelmann, S. Z. Qiao, S. Huang, and Y. Chen. Observation of active sites for oxygen reduction reaction on nitrogen-doped multilayer graphene. *ACS Nano*, 8(7):6856–6862, 2014.

[206] L. Qu, Y. Liu, J. B. Baek, and L. Dai. Nitrogen-doped graphene as efficient metal-free electrocatalyst for oxygen reduction in fuel cells. *ACS Nano*, 4(3):1321–1326, 2010.

[207] C. H. Choi, H. K. Lim, M. W. Chung, J. C. Park, H. Shin, H. Kim, and S. I. Woo. Long-range electron transfer over graphene-based catalyst for high-performing oxygen reduction reactions: Importance of size, n-doping, and metallic impurities. *Journal of the American Chemical Society*, 136(25):9070–9077, 2014.

[208] Y. Zhang, X. Zhang, and J. Su. An AVC system based coordinated control method for reactive power at gateway between provincial and regional power grids. *Power System Technology*, 37(10):2771–2777, 2013.

[209] L. Yang, S. Jiang, Y. Zhao, L. Zhu, S. Chen, X. Wang, Q. Wu, J. Ma, Y. Ma, and Z. Hu. Boron-doped carbon nanotubes as metal-free electrocatalysts for the oxygen reduction reaction. *Angewandte Chemie*, 123(31):7270–7273, 2011.

[210] L. Ferrighi, M. Datteo, and C. Di Valentin. Boosting graphene reactivity with oxygen by boron doping: Density functional theory modeling of the reaction path. *The Journal of Physical Chemistry C*, 118(1):223–230, 2014.

[211] G. Fazio, L. Ferrighi, and C. Di Valentin. Boron-doped graphene as active electrocatalyst for oxygen reduction reaction at a fuel-cell cathode. *Journal of Catalysis*, 318:203 – 210, 2014.

[212] Y. Jiao, Y. Zheng, M. Jaroniec, and S. Z. Qiao. Origin of the electrocatalytic oxygen reduction activity of graphene-based catalysts: A roadmap to achieve the best performance. *Journal of the American Chemical Society*, 136(11):4394–4403, 2014.

[213] X. Liu and L. Dai. Erratum: Carbon-based metal-free catalysts. *Nature Reviews Materials*, 1(1):16082, 2016.

[214] P. Lazar, S. Zhang, K. Šafářová, Q. Li, J. P. Froning, J. Granatier, P. Hobza, R. Zbořil, F. Besenbacher, M. Dong, and M. Otyepka. Quantification of the interaction forces between metals and graphene by quantum chemical calculations and dynamic force measurements under ambient conditions. *ACS Nano*, 7(2):1646–1651, 2013.

[215] G. Giovannetti, P. A. Khomyakov, G. Brocks, V. M. Karpan, J. van den Brink, and P. J. Kelly. Doping graphene with metal contacts. *Physical Review Letters.*, 101:026803, 2008.

[216] Lara Ferrighi and Cristiana Di Valentin. Oxygen reactivity on pure and b-doped graphene over crystalline Cu(111). effects of the dopant and of the metal support. *Surface Science*, 634:68 – 75, 2015.

[217] S. H. Noh, D. H. Kwak, M. H. Seo, T. Ohsaka, and B. Han. First principles study of oxygen reduction reaction mechanisms on N-doped graphene with a transition metal support. *Electrochimica Acta*, 140:225 – 231, 2014.

[218] J. Hölzl and F. K. Schulte. Work function of metals. In *Solid surface physics*, pages 1–150. Springer, 1979.

[219] F. Sedona, M. Di Marino, D. Forrer, A. Vittadini, M. Casarin, A. Cossaro, L. Floreano, A. Verdini, and M. Sambi. Tuning the catalytic activity of Ag(110)-supported fe phthalocyanine in the oxygen reduction reaction. *Nature Materials*, 11(11):970–977, 2012.

[220] M. Casarin, M. Di Marino, D. Forrer, M. Sambi, F. Sedona, E. Tondello, A. Vittadini, V. Barone, and M. Pavone. Coverage-dependent architectures of iron phthalocyanine on Ag(110): a comprehensive STM/DFT study. *The Journal of Physical Chemistry C*, 114(5):2144–2153, 2010.

[221] E. Schiavo, A. B. Muñoz-García, P. Maddalena, O. Crescenzi, and M. Pavone. Doped graphene and Ag(111) hybrid material as fuel cell electrode: new insights on interfacial features and oxygen adsorption from dispersion-corrected density functional theory. *Computational Materials Science*, 169:109141, 2019.

[222] C.L. Liu, J.M. Cohen, J.B. Adams, and A.F. Voter. EAM study of surface self-diffusion of single adatoms of fcc metals Ni, Cu, Al, Ag, Au, Pd, and Pt. *Surface Science*, 253(1):334 – 344, 1991.

[223] B. Kiraly, E. V. Iski, A. J. Mannix, B. L. Fisher, M. C. Hersam, and N. P. Guisinger. Solid-source growth and atomic-scale characterization of graphene on Ag(111). *Nature communications*, 4:2804, 2013.

[224] M. Vanin, J. J. Mortensen, A. K. Kelkkanen, J. M. Garcia-Lastra, K. S. Thygesen, and K. W. Jacobsen. Graphene on metals: A van der Waals density functional study. *Physical Review B*, 81:081408, 2010.

[225] I. Hamada and M. Otani. Comparative van der Waals density-functional study of graphene on metal surfaces. *Physical Review B*, 82:153412, 2010.

[226] I. Lončarić and V. Despoja. Benchmarking van der waals functionals with noncontact rpa calculations on graphene-Ag(111). *Physical Review B*, 90:075414, 2014.

[227] E. R. McNellis, J. Meyer, and K. Reuter. Azobenzene at coinage metal surfaces: Role of dispersive van der Waals interactions. *Physical Review B*, 80:205414, 2009.

[228] C. Huang, A. B. Muñoz-García, and M. Pavone. Effective scheme for partitioning covalent bonds in density-functional embedding theory: From molecules to extended covalent systems. *The Journal of Chemical Physics*, 145(24):244103, 2016.

[229] S. Manzeli, D. Ovchinnikov, D. Pasquier, O. V. Yazyev, and A. Kis. 2D transition metal dichalcogenides. *Nature Reviews Materials*, 2:15. 17033, 2017.

[230] M. Chhowalla, H. S. Shin, G. Eda, L. J. Li, K. P. Loh, and H. Zhang. The chemistry of two-dimensional layered transition metal dichalcogenide nanosheets. *Nature Chemistry*, 5(4):263–275, 2013.

[231] K. S. Novoselov, A. K. Geim, S. V. Morozov, D. Jiang, M. I. Katsnelson, I. V. Grigorieva, S. V. Dubonos, and AA Firsov. Two-dimensional gas of massless dirac fermions in graphene. *Nature*, 438(7065):197, 2005.

[232] Y. Zhang, Y. W. Tan, H. L. Stormer, and P. Kim. Experimental observation of the quantum hall effect and Berry's phase in graphene. *Nature*, 438(7065):201, 2005.

[233] B. Radisavljevic, M. B. Whitwick, and A. Kis. Integrated circuits and logic operations based on single-layer MoS_2. *ACS Nano*, 5(12):9934–9938, 2011.

[234] F. Peyskens, C. Chakraborty, M. Muneeb, D. Van Thourhout, and D. Englund. Integration of single photon emitters in 2D layered materials with a silicon nitride photonic chip. *Nature Communications*, 10(1):4435, 2019.

[235] W. Bao, X. Cai, D. Kim, K. Sridhara, and M. S. Fuhrer. High mobility ambipolar MoS_2 field-effect transistors: Substrate and dielectric effects. *Applied Physics Letters*, 102(4):042104, 2013.

[236] K. F. Mak, C. Lee, J. Hone, J. Shan, and T. F. Heinz. Atomically thin mos_2: A new direct-gap semiconductor. *Physical Review Letters.*, 105:136805, 2010.

[237] M. R. Islam, N. Kang, U. Bhanu, H. P. Paudel, M. Erementchouk, L. Tetard, M. N. Leuenberger, and S. I. Khondaker. Tuning the electrical property via defect engineering of single layer MoS_2 by oxygen plasma. *Nanoscale*, 6:10033–10039, 2014.

[238] J. Zhang, T. Wang, P. Liu, S. Liu, R. Dong, X. Zhuang, M. Chen, and X. Feng. Engineering water dissociation sites in MoS_2 nanosheets for accelerated electrocatalytic hydrogen production. *Energy and Environmental Science.*, 9:2789–2793, 2016.

[239] K. K. Ghuman, S. Yadav, and C. V. Singh. Adsorption and dissociation of H_2O on monolayered MoS_2 edges: Energetics and mechanism from ab initio simulations. *The Journal of Physical Chemistry C*, 119(12):6518–6529, 2015.

[240] X. Hong, J. Kim, S. F. Shi, Y. Zhang, C. Jin, Y. Sun, S. Tongay, J. Wu, Y. Zhang, and F. Wang. Ultrafast charge transfer in atomically thin MoS_2/WS_2 heterostructures. *Nature Nanotechnology*, 9(9):682–686, 2014.

[241] H. Chen, X. Wen, J. Zhang, T. Wu, Y. Gong, X. Zhang, J. Yuan, C. Yi, J. Lou, P. M. Ajayan, W. Zhuang, G. Zhang, and J. Zheng. Ultrafast formation of interlayer hot excitons in atomically thin MoS_2/WS_2 heterostructures. *Nature Communications*, 7(1):12512, 2016.

[242] D. Vikraman, S. Hussain, K. Akbar, L. Truong, A. Kathalingam, S. H. Chun, J. Jung, H. J. Park, and H. S. Kim. Improved hydrogen evolution reaction

performance using MoS_2–WS_2 heterostructures by physicochemical process. *ACS Sustainable Chemistry & Engineering*, 6(7):8400–8409, 2018.

[243] F. M. Pesci, M. S. Sokolikova, C. Grotta, P. C. Sherrell, F. Reale, K. Sharda, N. Ni, P. Palczynski, and C. Mattevi. MoS_2/WS_2 heterojunction for photoelectrochemical water oxidation. *ACS Catalysis*, 7(8):4990–4998, 2017.

[244] Ashwin R. Large excitonic effects in monolayers of molybdenum and tungsten dichalcogenides. *Physical Review B*, 86(11):115409, 2012.

[245] C. Gong, H. Zhang, W. Wang, L. Colombo, R. M. Wallace, and K. Cho. Band alignment of two-dimensional transition metal dichalcogenides: Application in tunnel field effect transistors. *Applied Physics Letters*, 103(5):053513, 2013.

[246] D. Y. Qiu, F. H. da Jornada, and S. G. Louie. Optical spectrum of mos_2: Many-body effects and diversity of exciton states. *Physical Review Letters.*, 111:216805, 2013.

[247] L. Liang and V. Meunier. First-principles raman spectra of MoS_2, WS_2 and their heterostructures. *Nanoscale*, 6:5394–5401, 2014.

[248] L. Debbichi, O. Eriksson, and S. Lebègue. Electronic structure of two-dimensional transition metal dichalcogenide bilayers from ab initio theory. *Physical Review B*, 89:205311, 2014.

[249] A. Molina-Sánchez, D. Sangalli, K. Hummer, A. Marini, and L. Wirtz. Effect of spin-orbit interaction on the optical spectra of single-layer, double-layer, and bulk mos_2. *Physical Review B*, 88:045412, 2013.

[250] E. Torun, H. P. C. Miranda, A. Molina-Sánchez, and L. Wirtz. Interlayer and intralayer excitons in MoS_2/WS_2 and $MoSe_2/WSe_2$ heterobilayers. *Physical Review B*, 97:245427, 2018.

[251] K. Kośmider and J. Fernández-Rossier. Electronic properties of the MoS_2-WS_2 heterojunction. *Physical Review B*, 87:075451, 2013.

[252] B. Amin, N. Singh, and U. Schwingenschlögl. Heterostructures of transition metal dichalcogenides. *Physical Review B*, 92:075439, 2015.

[253] C. Ataca and S. Ciraci. Dissociation of H_2O at the vacancies of single-layer MoS_2. *Physical Review B*, 85:195410, 2012.

[254] F. Ling, X. Liu, H. Jing, Y. Chen, W. Zeng, Y. Zhang, W. Kang, J. Liu, L. Fang, and M. Zhou. Optimizing edges and defects of supported MoS_2 catalysts for hydrogen evolution via an external electric field. *Physical Chemistry Chemical Physics.*, 20:26083–26090, 2018.

[255] G. Ye, Y. Gong, J. Lin, B. Li, Y. He, S. T. Pantelides, W. Zhou, R. Vajtai, and P. M. Ajayan. Defects engineered monolayer MoS_2 for improved hydrogen evolution reaction. *Nano Letters*, 16(2):1097–1103, 2016.

[256] H. Li, C. Tsai, A. L. Koh, L. Cai, A. W. Contryman, A. H. Fragapane, J. Zhao, H. S. Han, H. C. Manoharan, F. Abild-Pedersen, J. K. Nørskov, and X. Zheng. Activating and optimizing MoS_2 basal planes for hydrogen evolution through the formation of strained sulphur vacancies. *Nature Materials*, 15(1):48–53, 2016.

[257] D. Voiry, H. Yamaguchi, J. Li, R. Silva, D. C. B. Alves, T. Fujita, M. Chen, T. Asefa, V. B. Shenoy, G. Eda, and M. Chhowalla. Enhanced catalytic activity in strained chemically exfoliated ws2 nanosheets for hydrogen evolution. *Nature Materials*, 12(9):850–855, 2013.

[258] P. K. Chow, R. B. Jacobs-Gedrim, J. Gao, T. M. Lu, B. Yu, H. Terrones, and N. Koratkar. Defect-induced photoluminescence in monolayer semiconducting transition metal dichalcogenides. *ACS Nano*, 9(2):1520–1527, 2015.

[259] S. Zhang, C. G. Wang, M. Y. Li, D. Huang, L. J. Li, W. Ji, and S. Wu. Defect structure of localized excitons in a wse_2 monolayer. *Physical Review Letters.*, 119:046101, 2017.

[260] A. Srivastava, M. Sidler, A. V. Allain, D. S. Lembke, A. Kis, and A. Imamoğlu. Optically active quantum dots in monolayer WSe_2. *Nature Nanotechnology*, 10(6):491–496, 2015.

[261] V. Carozo, Y. Wang, K. Fujisawa, B. R. Carvalho, A. McCreary, S. Feng, Z. Lin, C. Zhou, N. Perea-López, A. L. Elías, B. Kabius, V. H. Crespi, and M. Terrones. Optical identification of sulfur vacancies: Bound excitons at the edges of monolayer tungsten disulfide. *Science Advances*, 3(4), 2017.

[262] S. Salehi and A. Saffarzadeh. Optoelectronic properties of defective MoS_2 and WS_2 monolayers. *Journal of Physics and Chemistry of Solids*, 121:172 – 176, 2018.

[263] R. G. Dickinson and L. Pauling. The crystal structure of molybdenite. *Journal of the American Chemical Society*, 45(6):1466–1471, 1923.

[264] W. J. Schutte, J. L. De Boer, and F. Jellinek. Crystal structures of tungsten disulfide and diselenide. *Journal of Solid State Chemistry*, 70(2):207–209, 1987.

[265] Y. L. Huang, Y. Chen, W. Zhang, S. Y. Quek, C. H. Chen, L. J. Li, W. T. Hsu, W. H. Chang, Y. J. Zheng, W. Chen, and A. T. S. Wee. Bandgap tunability at single-layer molybdenum disulphide grain boundaries. *Nature Communications*, 6(1):6298, 2015.

[266] B. Zhu, X. Chen, and X. Cui. Exciton binding energy of monolayer WS_2. *Scientific Reports*, 5(1):9218, 2015.

[267] G. B. M. Stan and M. C. Toroker. On the nature of trapped states in an MoS_2 two-dimensional semiconductor with sulfur vacancies. *Molecular Physics*, 117(15-16):2058–2068, 2019.

[268] B. Schuler, D. Y. Qiu, S. Refaely-Abramson, C. Kastl, C. T. Chen, S. Barja, R. J. Koch, D. F. Ogletree, S. Aloni, A. M. Schwartzberg, J. B. Neaton, S. G. Louie, and A. Weber-Bargioni. Large spin-orbit splitting of deep in-gap defect states of engineered sulfur vacancies in monolayer ws_2. *Physical Review Letters.*, 123:076801, 2019.

[269] A. V. Krivosheeva, V. L. Shaposhnikov, V. E. Borisenko, J. L. Lazzari, C. Waileong, J. Gusakova, and B. K. Tay. Theoretical study of defect impact on two-dimensional MoS_2. *Journal of Semiconductors*, 36(12):122002, 2015.